UNIVERSITY OF NAPLES FEDERICO II

DEPARTMENT OF PHARMACY

PhD programme in Pharmaceutical Sciences

Effects of radiotherapy on the mechanical microenvironment of breast cancer cell to improve HA-coated NPs delivery

PhD student
Dr. GIUSEPPE LA VERDE

Coordinator
Prof.
ROSARIA MELI

Tutor
Prof. Prof. MARCO LA COMMARA

Co-Tutor
Prof. VALERIA PANZETTA

XXXV CYCLE (2019-2022)

*“*Chi ha un *perché* abbastanza forte
può superare qualsiasi *come*.*”*

Friedrich Nietzsche

Ai miei genitori,
inesauribile fonte d’ispirazione

TABLE OF CONTENT

List of abbreviations

ANOVA	Analysis of Variance
APS	Ammonium Persulfate Solution
APTES	3-aminopropyltriethoxysilane
AT	Area Traveled
BPE	Bovine Pituitary Extract
BSA	Bovine Serum Albumin
BT	Brachytherapy
CD-44	Receptor Cluster Determinant 44
CI	Circularity Index
CK	Cytokeratins
Col	Collagen
CsI	Caesium Iodine
CSK	Cytoskeleton
CT	Computed Tomography
CTV	Clinical Target Volume
DLS	Dynamic Light Scattering
DMEM	Dulbecco's Modified Eagle Medium
DVH	Dose-Volume Histograms
EBRT	External Beam Radiation Therapy
ECM	Extracellular Matrix
EMT	Epithelial-Mesenchymal Transition
EPR	Enhanced Permeability and Retention Effect
ER	Estrogenic Receptor
FA	Focal Adhesion
FAK	Focal Adhesion Kinase
FBS	Fetal Bovine Serum
FDA	Food and Drug Administration
FN	Fibronectin
FOV	Field of View
GA	Gentamicin-Amphotericin
GTV	Gross Tumor Volume
HA	Hyaluronic Acid

HA-PP-NPs	Poly(lactic-co-glycolic acid) and Poloxamers Nanoparticles coated with hyaluronic acid
HARE	Hyaluronic Acid Receptor
hEGF	Human Epidermal Growth Factor
HEPES	(4-(2-hydroxyethyl)-1-piperazineethanesulfonic acid)
HER-2	Human Epidermal growth factor Receptor 2
HR	Hormonal Receptors
ICAM-1	Intracellular Adhesion Molecule-1
IGRT	Image-Guided Radiation Therapy
IORT	Intraoperative Radiotherapy
LINAC	Linear Accelerator
LINC	Linker of Nucleoskeleton and Cytoskeleton complex
LN	Laminin
LQ	Linear Quadratic model
LYVE-1	Lymphatic Vessels
MDR	Multidrug Resistance
MEGM	Mammary Epithelial Cell Growth Medium
MRI	Magnetic Resonance Imaging
MSD	Mean Square Displacement
MU	Monitor Units
NaOH	Sodium Hydroxide
NPs	Nanoparticles
NTCP	Normal Tissue Complication Probability
OAR	Organs at Risk
PAA	Polyacrylamide
PBS	Phosphate Buffered Saline
PCA	Principal Component Analysis
PDI	Polydispersity Index
PGA	Poly(Glycolic Acid)
PLA	Poly(Lactic Acid)
PLGA	Poly(Lactic-Co-Glycolic Acid)
PP-NPs	Nanoparticles in Poly(lactic-co-glycolic acid) and Poloxamers coated with hyaluronic acid

PR	Progesterone Receptor
PTV	Planning Target Volume
RHAMM	Receptor for Hyaluronan Mediated Motility
Rho A	Ras homolog A
ROCK	Rho-associated protein kinase
ROI	Region Of Interest
RS	Raman Spectroscopy
SERS	Surface Enhanced Raman Scattering
SF	Shape Factor
sulpho-SANPAH	(Sulfosuccinimidyl 6-(4′-Azido-2′-Nitrophenylamino)Hexanoate
TAZ	Transcriptional Coactivator With PDZ-Binding Motif
TCP	Tumor Control Probability
TEAD	Transcription Enhancers Activation Domain
TEMED	Tetramethylethylenediamine
TER	Trajectory Extension Ratio
TME	Tumor Microenvironment
TNBC	Triple Negative Breast Cancer
TNM	Tumor, Node, Metastasis system
TPS	Treatment Planning System
TRITON X	t-Octylphenoxypolyethoxyethanol, Polyethylene glycol tert-octylphenyl ether
TRP	Transient Receptor Potential
TSG-6	Gene-6 Stimulated By Tumor Necrosis Factor
XVI	X-Ray Volumetric Imaging
YAP	Yes-Associated Protein

Abstract

Managing the medical treatment of widespread diseases, such as cancer, poses both a scientific and a health challenge. However, in systemic therapies as chemotherapy, failure is usually caused by the intrinsic biological nature of cells among which multidrug resistance (MDR); on the other hand, it promotes the development of alternative approaches such as targeted therapy and nanomedicine. Also radiotherapy, a localized treatment, is constantly improving: the irradiations are tailor-made for each individual case, guaranteeing the maximum dose on the tumor and saving the surrounding ones as much as possible. What follows, therefore, is that the study for treatment plans optimization plays a fundamental role in the success of the therapy.

This PhD project investigated the effects of ionizing radiation, at the doses used in traditional radiotherapy (2 and 10 Gy), on the biophysical properties of breast cancer cells (MDA-MB-231, classified as triple negative, highly metastatic). From mechanobiological point of view, the cytoskeleton and extracellular matrix alterations result in a reduction of metastatic processes. A further implication is that they could represent a strategy to increase targeted therapy, bypassing the cancer cells MDR.

The work is organized in three parts, corresponding to the thesis chapters and which concerned: (i) study of cellular microenvironment with a detailed biophysical characterization of the effects of radiation on spreading, migration and expression of proteins that influence the nuclear structure; (ii) formulation and stability measurements of nanoparticles functionalized with hyaluronic acid, as a therapeutic tool in view of clinical application; (iii) study of internalization of cells irradiated with doses typical for radiotherapy.

The results encourage a combination radio- chemo-therapy in order to exploit ionizing radiation both to reduce the progression of metastases and to promote drug delivery.

Introduction

Breast cancer is the most common malignancy accounting for 28% of all cancers in women in Europe and 30% in Italy [1]. Despite the progress of the prevention and diagnostic campaigns, to date, 6-7% of cases present metastases already at diagnosis [2].

Advances in scientific research have different directions and areas of expertise that converge on the same point: adequate treatment for the disease. For this reason, a multidisciplinary approach is needed.

Any treatment is planned only after cancer characterization.

In particular, breast cancer is a complex disease made up of a large number of subtypes that have distinct biological characteristics [3] and, therefore, lead to different responses to treatments. However, it is increasingly evident that histological aspect alone may not be sufficient to understand the mechanisms underlying these alterations, making the therapeutic choice unsuccessful.

In recent decades, thanks to the advancement of gene expression profiling techniques, and through a systematic analysis of gene expression profiles (in terms of genomic DNA copy number arrays, DNA methylation, exome sequencing, messenger RNA arrays, microRNA sequencing), 50 genes (PAM50) closely related to the biology were identified. These results allowed to define intrinsic molecular subtypes [4]:

- Luminal A: (40-55%) have high levels of estrogenic receptor (ER) expression and absence of human epidermal growth factor receptor 2 (HER-2) expression and low cell proliferation index. Most are well differentiated or moderately differentiated therefore tumors

grow slowly and respond well to hormonal treatments; few respond to standard chemotherapy.

- Luminal B: (15-20%) have HER-2 overexpression, high levels of ER expression, and high levels of expression of genes involved in cell proliferation. They are sometimes called triple positives and respond to hormone therapy, while the response to chemotherapy is variable, with phenotype B responding better than phenotype A. [5].

- HER-2: (7-12%) are invasive carcinomas; with high-grade neoplasms and include ER-negative carcinomas that overexpress HER-2. HER-2 cancers are usually poorly differentiated, have a high proliferation rate and are associated with a high frequency of brain metastases. Respond to trastuzumab therapy and anthracycline chemotherapy; however, they have a poor prognosis [6].

- Basal like: (13-25%) are invasive carcinomas characterized by the absence of ER, HER-2 and progesterone receptor (PR); on the other hand, they have an expression of cytokeratins such as CK5, CK14, CK17, present in the basal/mypetelial layer of the normal mammary gland. Basal carcinomas frequently have a similar structure to the so-called “triple negative breast cancer” (TNBC) due to the loss of expression of hormonal receptors (HR) and the absence of HER-2 hyper-expression. The basal cell phenotype is characterized by a high probability of relapse (lung and brain metastases) and by a significantly low total and disease-free survival.

– Normal-like (5-10%) are a subtype on whose real existence there are still doubts. They express genes characteristic of adipose tissue and have an intermediate prognosis between luminal and basal, not responding to neo-adjuvant chemotherapy. They are usually well differentiated, express ER but not HER-2.

Once the type of tumor has been identified, the staging, i.e., size and location, must be defined. The possible diagnoses are [5]:

– Stage 0: usually described as non-infiltrating or intraductal, as cells do not invade the tissue;

– Stage 1: maximum diameter not exceeding 2 cm; the axillary lymph nodes are free, and the neoplastic cells have not spread to other organs;

– Stage 2: maximum diameter between 2 and 5 cm or the axillary lymph nodes are invaded, or reveals both of these characteristics, but the neoplastic cells have not migrated to other organs;

– Stage 3: maximum diameter of up to 5 cm and is fixed to nearby structures (skin or muscle); the lymph nodes are usually invaded, but the neoplastic cells have apparently not spread beyond the breast or to the axillary lymph nodes;

– Stage 4: regardless of the diameter, the lymph nodes are usually invaded and the cancer cells have spread to other sites in the body. Due to metastases, it is the most difficult case to cure and the outcome is often fatal.

Another parameter is *grading* which indicates how quickly cancer cells can infiltrate: from grade 1 in which the cells are similar to healthy ones, up to grade 3 in which cells grow rapidly and spread over a distance.

Finally, for a more exhaustive characterization, there is the clinical staging and classification system known as Tumor, Node, Metastasis (TNM) system [7]: T refers to the size of the primary tumor, the scale ranges from 1, which identifies the smallest tumors, to 4 for the largest ones; N indicates whether the cancer has spread to the lymph nodes, it can be followed by a number ranging from 0 (no lymph nodes involved) to 3 (many lymph nodes involved); M, which stands for metastasis, can have a value of 0 (if the tumor has remained confined to its primary site) or 1 (when the tumor has spread to other parts of the body).

This brief overview on diagnosis highlights the complexity of the disease, the diagnosis, and the multiplicity of therapeutic approaches. In the latter area too, much progress has been made and several healing methods are available to date.

The main international protocols provide broadly for:

- Surgery to remove diseased tissue (conservative surgery, removing only the part where the tumor is) or mastectomy (removing the entire breast)
- Radiotherapy (carried out after surgery) is used to protect the remaining mammary gland from the risk of local recurrence.
- Chemotherapy is prescribed after a tailored evaluation of the characteristics of each case and offering a wide range of solutions, including targeted therapy, nanomedicine, use of natural compounds, etc.
- Immunotherapy in combination with chemotherapy, which can be useful in the treatment of some advanced cancer, with particular attention for TNBC.

Surgery and radiation therapy are treatments usually used for local, non-metastatic cancers, but are ineffective when the cancer has spread throughout the body. The use of drugs (chemotherapy, hormonal and biological) able to reach every organ of the body through the bloodstream is the most effective choice for the treatment of metastatic tumors. At the same time use of drugs is distributed throughout the duration and phases of the disease. In this scenario, the gold standard is chemotherapy, despite having many enemies to face. The most important are adverse effects on the patient such as inhibition of fast-turnover healthy cells (hair follicles, bone marrow, and gastrointestinal cells) [8], and the multidrug resistance (MDR) typical for the most aggressive tumors. These limitations, together with a deeper understanding of the cellular mechanisms involved in disease processes, have stimulated the development of nanomedicine, a science that, over the past 15 years, has produced promising results in drug delivery, diagnosis, imaging, and therapy practices [9]. Using nanodevices (nanoparticles, NPs) it is possible to functionalize their surface and direct them towards target organs, reducing systemic toxicity and optimizing drug transport (targeted therapy).

Also, in this case the challenges are not few, the molecule that functionalizes the NPs and that was chosen for its affinity for a specific receptor over-expressed in cancer cells, could have competitors between different receptors expressed on all types of cells. An example is hyaluronic acid (HA), used to functionalize the NPs surface and be selectively recognized by the membrane receptor cluster determinant 44 (CD-44), known to be overexpressed on the tumor cells surface. In this case HA has different competitor receptors, which are an obstacle for targeted therapy [10]. This phenomenon could influence drug delivery: the NPs loaded with a drug and functionalized for a specific receptor of the

tumor cell, would have the availability of more receptors, thus diverting its path towards non-target cells. [11]. Another obstacle is the interaction between the molecule used to functionalize and the cellular environment, such as the formation of the protein corona [12]. By partially or totally masking the functionalization, the therapeutic aim consequently fails.

The effort of scientific research is, also in this case, to study strategies to solve this kind of challenges such as using other molecules linked to HA specific for the competitor CD-44 receptors use of folate [13, 14] or saturating with a pre-administration of HA [15, 16].

An innovative point of view, purpose of this PhD project, is to assess how mechanobiological effects, occurring in cells after irradiation, can offer a solution for the improvement of drug delivery and the success of targeted therapy.

PhD project: aim and structure of thesis

Cell cytoskeleton (CSK) and the extracellular matrix (ECM), from a mechanobiological point of view, play an important role in the correct functioning of many tissue processes [17-20]. In fact, if these structures undergo alterations, they produce effects on cellular responses [21]. Cancer cells have a less organized and structured CSK with lower cellular mechanical and cytoadhesive properties than their healthy counterparts. Furthermore, changes in the composition and architecture of the ECM result in a stiffening process of the matrix that activates cell proliferation and a consequent invasion mechanism [22]. The ECM itself can ultimately influence the mechanical properties of the CSK.

Therapeutic treatments are also aimed at modulating these biophysical characteristics to obtain positive outcomes. Recently, several research groups have begun to focus their attention on studying the possible impacts

of radiation on the cell CSK and its associated functions such as motility, a prerequisite for the formation of metastases. However, it remains a sector with broad themes to discover.

Therefore, considering the challenges of drug delivery and the potential of the effects of ionizing radiation on cellular structures, the rationale of this PhD project was therefore to investigate, from a biophysical and mechanobiological point of view, how, after a traditional radiotherapy treatment, the alterations produced may be favourable to increasing the internalization of NPs.

Understanding these mechanisms would offer a solution to the aforementioned competition and masking processes, which hinder the targeted therapy of NPs, as well as an optimization of therapeutic treatment protocols that involve the combination of radio and chemo-therapy.

The approach to this study was multisciplinary (physics applied to biology, biomedical engineering, pharmaceutical technology, medical physics) and provided for use of various facilities, requiring effort and devotion but offering, at the same time, the fascinating opportunity to combine different skills for a common purpose.

The project can be divided into three parts, corresponding to the thesis chapters:

Chapter 1. Characterization of the biophysical effects of photon irradiation at the doses used in radiotherapy (2 and 10 Gy) on healthy (MCF10A) and triple negative (MDA-MB-231) breast cells. To understand the CSK-ECM interaction, cell lines were seeded on polyacrylamide substrates with stiffnesses mimicking healthy (1.3 kPa) and tumor (13 kPa) tissue. After 24 h and 72 h from irradiation,

morphological parameters, such as the spreading, the shape factor (SF) and circularity index (CI), and migration physical parameters, such as velocity, mean square displacement (MSD), trajectory extension ratio (TER) and the area traveled (AT), were analysed. Considering that alterations in mechanosensing are then translated into protein expression, the results obtained were analysed also in terms of expression and localization of Yes-associated protein (YAP)/Transcriptional coactivator with PDZ-binding motif (TAZ) complex and of the lamin A/C protein. Results confirmed that high doses of radiation modify the mechanical characteristics typical for cancer cells, sparing healthy ones.

Chapter 2. Formulation and stability studies of hyaluronic acid (HA) coated nanoparticles (NPs). Based on the targeted therapy principle, the over expression of the CD-44 receptor of MDA-MB-231 and its high affinity for HA was considered. The stability of a formulation is fundamental to guarantee the surface functionalization over time, in view of clinical application. For this reason, Dynamic Light Scattering (DLS) analyses were carried out, and the dimensional changes recorded over time required the use of further investigations. In this work, the Surface Enhanced Raman Scattering (SERS) spectroscopy was implemented to quantify HA alterations over time, thus establishing the time within which surface functionalization is guaranteed.

Chapter 3. Internationalization analysis of HA coated NPs in breast cells after radiotherapy treatment. Including the biophysical effects of radiation on CSK, it was investigated whether these alterations could affect the ability to internalize NPs. The analyses were carried out by analysing the NPs fluorescence intensity, labeled with Rhodamine B, put in contact with cells after 24 h and 72 h from irradiation. The results

obtained confirm that the biophysics alterations recorded previously result in an increased ability of tumor cells to internalize NPs, especially at high doses, regardless of surface functionalization.

References

1. European Cancer Information System. Available from: https://ecis.jrc.ec.europa.eu/explorer.php?$0-0$1-IT$2-All$4-2$3-All$6-0,85$5-2020,2020$7-7$CEstByCancer$X0_8-3$CEstRelativeCanc$X1_8-3$X1_9-AE27$CEstBySexByCancer$X2_8-3$X2_-1-1 (Accessed on Sept 2022).
2. I numeri del cancro in Italia 2020. Available from: https://www.aiom.it/wpcontent/uploads/2020/10/2020_Numeri_Cancro-operatori_web.pdf (Accessed on Sept 2022).
3. Roulot A, et al. 2016. *Ann Biol Clin* (Paris). **74**(6):653-660. doi:10.1684/abc.2016.1192.
4. Perou CM, et al. 2000. *Nature*. **406**(6797):747-752. doi:10.1038/35021093.
5. Schnitt SJ. 2010. *Mod Pathol*. **23**(suppl2):60-64. doi:10.1038/modpathol.2010.33.
6. Hu Z, et al. 2006. *BMC Genomics*. **7**:96. doi:10.1186/1471-2164-7-96.
7. Sawaki M, et al. 2019. *Jpn J Clin Oncol*. **49**(3):228-231. doi:10.1093/jjco/hyy182.
8. Chabner BA, et al. 2005. *Nat Rev Cancer*. **5**(1):65-72. doi:10.1038/nrc1529.
9. Shi J, et al. 2017. *Nat Rev Cancer*. **17**(1):20-37. doi:10.1038/nrc.2016.108.
10. Yang B, et al. 1994. *EMBO J*. **13**(2):286-96. doi:10.1002/j.1460-2075.1994.tb06261.x.
11. Rios de la Rosa JM, et al. 2018. *Adv. Biosys*. **2**:1800049. doi:10.1002/adbi.201800049.
12. Berrecoso G, et al. 2020. *Drug Deliv Transl Res*. **10**(3):730-750. doi:10.1007/s13346-020-00745-0.
13. Liu Y, et al. 2011. *Int J Pharm*. **421**(1):160-9. doi:10.1016/j.ijpharm.2011.09.006.
14. Chen J, et al. 2017. *ACS Appl Mater Interfaces*. **9**(28):24140-24147. doi:10.1021/acsami.7b06879.
15. Ouasti S, et al. 2012. *Biomaterials*. **33**(4):1120-1134. doi:10.1016/j.biomaterials.2011.10.009.
16. Venning FA, et al. 2015. *Front Oncol*. **5**:224. doi:10.3389/fonc.2015.00224.
17. Porat-Shliom N, et al. 2013. *Cell Mol Life Sci.* **70**(12):2099-2121. doi:10.1007/s00018-012-1156-5.
18. Asparuhova MB, et al. 2009. *Scand J Med Sci Sports.* **19**(4):490-499. doi:10.1111/j.1600-0838.2009.00928.x.
19. Janota CS, et al. 2020. *Curr Opin Cell Biol*. **63**:204-211. doi:10.1016/j.ceb.2020.03.001.
20. Hohmann T, et al. *Cells*.**8**(4):362. doi:10.3390/cells8040362.

21. Hall A. 2009. *Cancer Metastasis Rev*. **28**(1-2):5-14. doi:10.1007/s10555-008-9166-3.
22. Stowers RS, et al. 2016. *Cell Mol Bioeng.* **10**(1):114-123. doi:10.1007/s12195-016-0468-1.

Chapter 1 – Ionizing radiation effects on cell mechanics of healthy and tumor breast cells on different stiffness substrates

1.1 Background

Many studies have shown a correlation between radiotherapy treatment, cell cytoskeleton (CSK) and extracellular matrix (ECM), fundamental features for the correct functioning of some biological processes. In fact, the mechanical crosstalk between cells and the ECM is necessary to maintain tissue homeostasis, guaranteeing its functionality and healthiness. When altered, it can lead to an alteration of the mechanical state of the tissue and cancer progression. In fact, while cancerous cells show a less organised CSK and lower mechanical properties, variations in the ECM composition, namely its stiffness, activate cell proliferation and invasion of tumoral cells in nearby sites. Hence, in order to better understand the effects of ionizing radiations on cells biophysical properties, the mechanical characterization of tumor cells and ECM is of critical importance. In fact, this study can offer new support to diagnosis and improve the outcomes of therapies, such as chemo- and radiotherapy.

The aim of this part of project is the investigation of biophysical properties, in particular cells spreading and migration ability, strictly associated to the cell mechanical properties, of two cell lines: an epithelial cell line, MCF10A, and an adenocarcinoma cell line, MDA-MB-231. Both cell lines, were cultivated on polyacrylamide (PAA) substrates characterized by two different stiffnesses, 1.3 kPa and 13 kPa, which simulated the healthy and cancerous tissue respectively. The study was carried out on samples in control condition and after delivery of two

different doses of X-rays, 2 and 10 Gy. These doses represent the daily and weekly dosages used in radiotherapy treatment.

1.1.1 Radiotherapy in breast cancer

Breast cancer is one of the most common types of cancer in European women. As already mentioned, the choice and success of the treatments depends on a correct diagnosis and tumor characterization [1]. Therapeutic applications can be single or, in most cases, combined. For solid and non-metastatic tumors, the first approach is surgery, which consists in eradicating the tumor from the breast and regional lymph nodes. Usually, after surgery, radiotherapy is used as an adjuvant treatment as it is considered essential to prevent recurrence of the disease. Chemotherapy represents the choice for a systemic approach in the treatment of different types of cancers at different stages [2].

In this study, radiotherapy was considered as a tool to evaluate the biomechanical alterations of cancer cells and how these can be managed as improvements for combined therapies.

Radiation therapy is a medical procedure used to control or kill malignant cells using ionizing radiation. Its purpose, in fact, is to damage the DNA of cancer cells, through complex lesions that are impossible for the cell to repair, thus eliminating the abnormal mass and effectively cleaning the tumor site [3].

To spare the healthy tissue, which is the skin and the organs that radiation must pass through to reach the cancerous site, shaped beams are pointed from different angles to intersect the tumor. Therefore, there is a much more absorbed dose at the tumor site than in the surrounding area [4].

There are several radiotherapy techniques including:

- External beam radiation therapy (EBRT), in which the radiation source is external, i.e., external to the patient's body;
- Brachytherapy (BT), in which a sealed source is placed inside or next to the area to be treated;
- Intraoperative radiotherapy (IORT), in which radiation is delivered during surgery;
- Ultra-high dose rate in radiotherapy (named FLASH radiotherapy) in which the delivered dose is in the range of 10–20 Gy with a dose rate of ~50 Gy/s. Recent experiments have shown that irradiation at doses far higher than those currently used in clinical settings, for shorter times than those currently practiced, reduces the toxicity induced by radiation while maintaining equivalent efficacy in contrasting cancer [5]. This could be a really important breakthrough for cancer treatment.

EBRT is the most used form of radiation oncology treatment. The standard therapeutic plan provides a dose of 50 Gy on 25 fractions, or a 10 Gy dose which represents the single maximum dose for the treatment of metastasis or, in IORT, a single dose boost, after the surgical intervention and before starting the cycle of 25 fractions of 2 Gy [6].

More recent studies have shown that using a lower dose (about 42.5 Gy on 16 fractions) is equally, if not even more, effective [7].

The logic of fractionation is based on the radiobiology's four Rs [8]:

1. **R**epair of sublethal damage: The repair kinetics of cancer cells are slower than that of normal cells. A limited pause between two irradiations allows normal cells to repair the damage and repopulate the tissue more quickly than cancerous cells.

2. **R**edistribution of cells within the cell cycle: cells in mitosis or late G2 phase are more radiosensitive because DNA synthesis has already doubled the genomic content within them. Cells in the late S phase are, on the other hand, more resistant to radiation damage, because DNA synthesis is still in progress, and it is easier to access the damaged points and thus repair them.
3. **R**e-oxygenation of tissue: in the interval between the single dose fractions there is a certain re-oxygenation of the hypoxic areas following the death and elimination of well oxygenated cells with consequent decompression of small vessels, reduction of the distance between capillaries and hypoxic cells, less discrepancy between oxygen supply and requirement
4. **R**epopulation: in response to the depopulation caused by irradiation, healthy and tumor tissues increase proliferative activity, recalling resting cells in the divisional cycle.

A fifth R is usually added to these: **R**adiosensitivity [9], high doses of radiation can induce greater genetic instability and, therefore, the colonies that form after irradiation are morphologically different from those formed in non-irradiated cultures. In these terms, genetic instability can affect both the number but also the properties of the surviving cells.

Based on these concepts, the purpose of radiotherapy is to administer a precisely measured dose of radiation at a defined tumor volume, with minimal damage to surrounding healthy tissues to achieve:

- eradication of the tumor;
- symptom improvement;
- improvement of the quality of life;
- prolongation of survival.

For this reason, it is very important to achieve an optimized fractionation of radiation delivery. The tumor site must initially be localized by computed tomography (CT) or magnetic resonance imaging (MRI), then, thanks to these technologies, different calculation models can be adopted to obtain an optimal dose delivery plan (Details are reported in Appendix A).

1.1.2 Mechanobiology of a cell: CSK and ECM role

Mechanobiology is a science which studies how the properties of the cell change when a physical force is applied to it. It focused on two main processes, (i) mechanosensing, that refers to the ability of the cell to sense the signals arriving from the environment, and (ii) mechanotransduction, which describes how the mechanical forces applied to the cell are transformed into biochemical signals.

Mechanosensing is an ensemble of cellular processes involving both intra and extracellular components. The main structural components contributing to mechanosensing are: integrins, CSK, and ECM [10]. (Details are reported in Appendix B)

On the other hand, transduction response is a complex combination of different signalling pathways [11-13].

Cells are systems that communicate with their surroundings by adapting responses to optimize their metabolic processes including those related to their adhesion and migration [14,15].

It is also known that both CSK and ECM have key roles in maintaining the correct functioning of many tissue processes which, if altered, have a decisive contribution to cancer progression. Indeed, cancer cells have a less organized and structured CSK with lower cellular mechanical and cytoadhesive properties than their healthy counterparts. Furthermore, the

dynamic alteration of the actin CSK has strong implications on the motility, invasion, and metastatic potential of cancer cells [16]. On the other hand, changes in the composition and architecture of the ECM determine a matrix stiffening process that activates cell proliferation and a consequent invasion mechanism. While cells undergo a softening process, their ECM exhibits a stiffening one, supporting the hypothesis of the ECM regulatory function along tumorigenesis and tumor progression [17-19]. In response to changes and stress in the tumor microenvironment (TME), CSK plays an important role in migration and adhesion processes.

Another sign of tumor invasion and progression is the epithelial-mesenchymal transition (EMT) process involved in tumor initiation, metastasis formation and resistance to therapy [20, 21]. During EMT process, epithelial cells, which are polarized and non-motile, disperse cell-to-cell junctions, exhibit impaired adhesiveness, and become motile, non-polarized and invasive mesenchymal cells. This step can lead to an increase in the migratory and invasive tendency of cells, due to the modulation of growth factor signalling and remodelling of CSK actin. EMT is induced by several factors, such as gene mutations or growth factor signalling, and cancer cells that go through this process can control several biological activities, which are essential for cell behaviour [16].

Through the mechanotransduction process, CSK converts physical stress into a biochemical response, influencing the behavior of cells (eg, division, adhesion, migration) [22]. Mechanical stimuli are then collected and sent to the cells through the activation of surface mechanosensors such as integrins [23] transient receptor potential (TRP) channels [24] and to the nucleus by means of Yes-associated protein (YAP)/Transcriptional coactivator with PDZ-binding motif (TAZ) complex [25]. YAP is a

transcriptional coactivating protein which, together with TAZ, is closely associated with mechanical and structural changes in the cellular microenvironment. These proteins can move from the cytoplasm to the nucleus, where they interact with the transcription enhancers activation domain (TEAD) family members, a protein association considered fundamental for promoting their transcriptional abilities. Also, the stiffness of the microenvironment influences mechanotransduction: stiff ECM in breast tumors can induce nuclear translocation of transcription factors, such as YAP, suggesting a close relationship between the mechanical properties of the ECM and the metastatic potential of the tumor.

Fig. 1.1 is a schematic representation of the entire mechanobiology process of a cell.

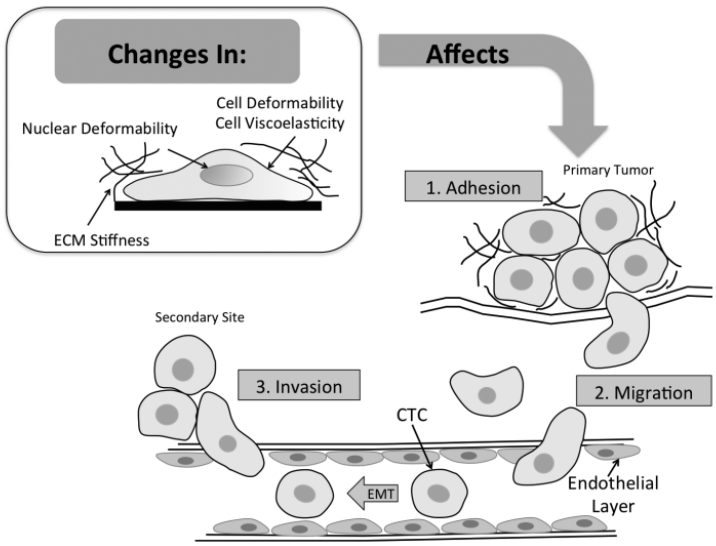

Figure 1.1 Summary of the processes involved in the mechanobiology of a cell. Adapted from [26].

1.1.3 Mechanobiological effects of ionizing radiation

Most studies have focused on both direct (30-40%) and indirect (70-60%) effects of ionizing radiation on DNA. This damage can produce mutation, carcinogenesis, or cell death upon cell recovery [27-29]. Worthy of note are the studies conducted by Woloschack and colleagues, where they analysed the radiation-induced mutations of the genes encoding the elements of the CSK. In particular, while one of their studies demonstrated that beta-actin mRNA was repressed after X-ray exposure [30], others demonstrated alterations in the mRNA expression of three elements of CSK and ECM: tubulin, actin and fibronectin [31,32]. In fact, during the first hour after exposure, it was possible to observe the accumulation of α-tubulin and γ-actin and the reduction of β-actin mRNA expression. The accumulation of transcripts for these genes has been shown to increase in a dose-dependent manner [31,32].

More recently, research on radiation-induced effects on cells has shifted to aspects of mechanobiology, specifically focusing on how DNA damage can affect the physical forces and mechanical integrity of cells. However, the scientific literature lacks a systematic and comprehensive analysis of the role of radiation in cellular mechanobiology. Therefore, given the growing importance of CSK dynamics in controlling the pathophysiology of tissues, much research has focused on quantifying the alterations of cytoskeletal proteins and related functions, such as adhesion and migration, after the therapeutic administration of ionizing radiation (Tab. 1.1 - Tab.1.3) [33].

Ionizing radiation can increase the polymerization of the actin filament and, thus, a thickening of the CSK. However, on the other hand, the same radiation can also produce an opposite effect (Tab. 1.1).

Table 1.1 Effects of radiation on actin CSK.

Cell line	Dose (Gy)	Time after irradiation	Observed effect on actin CSK	Ref.
Mel270, BLM	1 - 3	40 days	Increase of marginal actin filaments	[34]
BALBc/3T3 SVT2	1, 2	24 hours	Actin polymerization, increase actin filaments	[35,36]
HUVEC	2 - 8	n.a.	Remodelling of the actin CSK	[37]
LN229 U87	2	20, 40 hours	Activation of small GTPases Rac1K, increase in G-actin, decrease in F-actin	[38]
Cortical neurons	2, 4	24 hours	Decomposition and rearrangement of the F-actin	[39]
Calu-3 16HBE14o-	2 - 10	4 hours	Increase in F-actin depolymerization	[40]
MC3T3-E1	0.5, 5	5 days	Decrease in F-actin expression, expression of RhoA, ROCK1, and p-cofilin due to actin depolymerization	[41]
Murine exorbital lacrimal gland cells	0.036	4, 8 hours	Actin depolymerization, increase in the cellular area (*the outcomes were reversible after 24h*)	[42]
TSCC	0 - 4	24 hours	Disorganization of the F-actin	[43, 44]

Cells adhere to the ECM through the formation of focal adhesion (FA), which requires polymerization of actin and other factors including proteins and changes in CSK organization. In fact, the process of adhesion occurs when the proteins that form the ECM, such as fibronectin (FN), laminin (LN) and collagen (Col), interact with the integrin receptors, which are mainly involved in cell-ECM crosstalk.

A crucial element for cell motility is focal adhesion kinase (FAK), a protein implicated in cell cycle, survival and migration. Binding between cells and ECM activates FAKs, a signaling complex which, in turn, activates additional kinases, and therefore, leads to an increase in cellular invasiveness. Ionizing radiation can affect cell adhesion to FN through activation of Ras homolog A (Rho A)/Rho-associated protein kinase

ROCK (RhoA/ROCK) signaling pathways as they can control the FA assembly (Tab. 1.2)

Table 1.2 Effects of radiation on cell adhesion

Cell line	Dose (Gy)	Time after irradiation	Observed effect on cell adhesion	Ref.
MDA-MB-231	10	24 hours	Increase of the connection between cells and FN	[45]
U-87 MG U-373 MG MDA-MB-231	0, 2, 4, 8	24, 48 and 72 hours	Increased cell adhesion due to the activity of FAK and Src	[46]
HMEC-1	15	15 minutes	Increase cell adhesion due to FAs formation through the activation of RhoA/ROCK signalling pathways	[47, 48]
BALBc/3T3 SVT2	1, 2, 4, 8	24, 72 hours	Increased adhesion	[35,49-51]
MCF10A	2, 10	24 hours	The decreased adhesion resulted in inverse proportionality with the delivered dose. (The effects were reversible after 72h)	[52]
MDA-MB-231	2, 10	24, 72 hours	Decrease adhesion with lower dose on the softer substrate, the opposite phenomenon was observed on the stiffer substrate	

Changes in CSK, induced by radiation treatment, can also affect cell migration (Tab. 1.3). It is known that there is a strong correlation between the aggressive phenotype of cancer cell lines and the changes in the architecture of the CSK which are due, in turn, to the expression of different families of proteins such as integrins, small GTPases and the Linker of Nucleoskeleton and Cytoskeleton (LINC) complex.

Table 1.3 Effects of radiation on cell migration

Cell line	Dose (Gy)	Time after irradiation	Observed effect on cell migration	Ref.
BALBc/3T3, SVT2	4, 8	24, 72 hours	Reduced speed and motility. (*The effects were reversible after 72h for BALBc/3T3*)	[53]
BALBc/3T3, SVT2	1, 2	6, 24 hours	Reduced speed and motility	[50]
MCF10A	2, 10	24, 72 hours	After 24h cells showed an increased motility with 2 Gy; 72h after treatment cells showed a reduced motility	[52]
MDA-MB-231	2, 10	24, 72 hours	After 24 h cells showed an increase in the migration velocity (*this effect was reversible after 72h*)	
TSCC (Tca-8113)	0-4	24 hours	Increase in cell migration in a dose-dependent manner	[43]
U251, U87	0-10	24 hours	Increase in cell migration due to the expression of MMP-2 and MMP-9 enzymes	[54,55]
IOMM-Lee, CH-157-MN	7	24 hours	Increase in cell motility due to the overexpression of α3β1 integrin	[56]
NIH-3T3	1-8	21 days	Increase in cell migration due to the expression of α5β3 integrin	[57]
HMEC-1	15	15 minutes	Decrease in cell motility	[48]
RBL-2H3	0.01, 0.05, 0.1, 0.5	N.A.	Decrease in cell migration through the suppression of the MCP-1	[58]
MDA-MB-231	0.5	24, 48 hours	The expression of SUN1 and SUN2 proteins was necessary for the radiation-induced migration of cells	[59]

From this brief review analysis, it emerges that the cellular response to a physical stimulus such as ionizing radiation, in terms of adhesion and migration, is closely related to the time point after irradiation, radiation doses, and environmental conditions of the cell.

Finally, the mechanotransduction process is also influenced by the interaction with ionizing radiation. Some recent studies have also reported a direct correlation between YAP and cellular resistance to radiation. Low X-ray response is associated with high levels of YAP activation, while YAP silencing increases radiation sensitivity and cellular DNA damage [60-62].

1.2 Materials and Methods

This session concerns the methodology and techniques used to study the biophysical properties of two different cell lines, MCF10A and MDA-MB-231, and their responses to physical stimuli such as X-ray irradiation at two different doses, 2 and 10 Gy (typical for radiotherapy treatments).

Cells were seeded on substrates with two different stiffnesses, 1.3 kPa and 13 kPa, in order to simulate healthy and cancerous tissues, respectively. Finally, with microscope acquisitions, it was measured how X-rays can modify the CSK dynamics in both cell lines and how these alterations translate into different cellular mechanobiological responses. In particular spreading, migration, and YAP expression were investigated.

1.2.1 Cells lines

Two different human breast epithelial cell lines are used: MCF10A and MDA-MB-231 as models for normal and cancerous breast tissues respectively.

MCF10A in an immortalized cell line derived from benign breast tissue. This line shows the typical features of the normal breast epithelial cells, that is the lack of tumorigenicity, three-dimensional growth in collagen, dome formation in confluent cultures, and the growth in culture is controlled by hormones and growth factors [63].

Studies have shown that the three-dimensional model of this particular line is useful for dissecting cell-cell interactions in mammary gland development and for investigating how the microenvironment can affect the mammary cell functions. Additionally, this model can be used for the study of the effects of different genetic or non-genetic modifications on mammary cell transformation. Lastly, this cell line shows a basal-like phenotype, but, at the same time, shares many traits of mesenchymal cancer cells [64].

MCF10A cell line was grown in Lonza Mammary Epithelium Based Medium (MEBM), supplemented by the Mammary Epithelial Cell Growth Medium SingleQuots Kit (MEGM). This kit is composed of: i) Bovine Pituitary Extract (BPE); ii) Human Epidermal Growth Factor (hEGF); iii) Insulin (0.1%); iv) Hydrocortisone; v) Gentamicin-Amphotericin (GA-1000). While the final concentration of the BPE added to the medium was the 0.4%, the other growth factors were added in a final concentration of 0.1%.

The MDA-MB-231 cell line is taken from human breast cancer cells and represents the most frequently used breast cell line in medical studies to investigate a late-stage tumor. This type of cell is an extremely aggressive, invasive cell line and correspond to poorly differentiated TNBC. Akin to other cancer cell lines, the invasiveness of the MDA-MB-231 line is mediated by the proteolytic degradation of the ECM.

Researches have shown that in three-dimensional model, MDA-MB-231 cells present an endothelial-like morphology and are poorly differentiated and characterized by an invasive phenotype, having a stellate projection in cultures that often bridge multiple cell colonies [65].

MDA-MB-231 cell line was cultured in Lonza Dulbecco's Modified Eagle Medium (DMEM/F-12), which is used for supporting the growth of different mammalian cells. The medium was supplemented with 10% fetal bovine serum (FBS, Gibco), 1% L-Glutamine (Sigma, St. Louis, MO) and 1% Penicillin-Streptomycin (Sigma, St. Louis, MO).

1.2.2 Preparation of Substrate and Mechanical Characterization

Polyacrylamide gel substrates are used to simulate the ECM. Thereby it is possible to estimate tractions that cells apply on the substrate itself during migration and to investigate the cellular response to different condition of the ECM. Substrates with two different Young's Modulus, 1.3 kPa and 13 kPa, were used in order to simulate respectively the healthy and the cancerous tissue [66]. This was possible by a selection of proper concentrations of monomer acrylamide and the cross-linker bis-acrylamide [67].

For a stiffness of 1.3 kPa, solution was prepared in 1× Phosphate Buffered Saline (PBS 1×) with the following concentrations:

- 4% acrylamide;
- 0.15% bis-acrylamide.

For the stiffer substrate, whose Young's Modulus is 13 kPa, the concentrations used are:

- 10% acrylamide;
- 0.1% bis-acrylamide.

Both the solutions prepared were filtered with a 0.22 μm filter. Polyacrylamide gels were covalently attached to glass coverslips of 30 mm in diameter. Cover glasses were soaked with 0.25 mL of 1 M of sodium hydroxide (NaOH) and dried on a heating plate to achieve a slow evaporation of solution without reaching the boiling point. Subsequently,

under a suction arm, 0.25 mL of 3-aminopropyltriethoxysilane (APTES, Sigma, St. Louis, MO, USA) were spread uniformly on the coverslips. After 10 minutes, the cover glasses were extensively washed with distilled water and then put on the heating plate to dry. The polymerisation of the gel was achieved by mixing the solution of polyacrylamide with 1/100 total volume of 10% Ammonium Persulfate Solution (APS 10×) and 1/1000 total volume of catalyst tetramethylethylenediamine (TEMED; Fisher Scientific) that provided the desired level of cross-linking. 5 µl of this solution was deposited on the coverslips and a circular untreated cover glass (12 mm diameter) was placed on the top. After 20 minutes, the round cover glass was carefully removed with a scalpel. The substrates formed on the coverslip were attached to drilled dishes with a glass aperture of 22 mm (kit3522, Willco Wells) and then soaked with PBS 1×. To prevent bacterial contamination, the substrates were soaked with pen-strep overnight before cell culture.

1.2.3 Substrates functionalization

To allow cell adhesion, substrates were functionalized with collagen by using a bifunctional photolinker, N-sulphosuccinimidyl-6-(4′-azido-2′-nitrophenylamino) hexanoate (sulpho-SANPAH, ThermoFisher Scientific, 22589) as a cross-linking agent to immobilize collagen. A sulpho-SANPAH solution was freshly prepared at a final concentration of 0.2 mg/mL. The antibiotics solution was removed from the drilled dishes and 0.25 mL of solution was added to each plate. Then, the dishes were exposed to 365 nm UV light for 10 minutes. After the process of photoactivation, the Sulfo-SANPAH solution was removed and PAA substrates were extensively washed with PBS 1×.

Afterwards, 0.25 mL of 50 µg/mL of bovine type I collagen solution was added to every dish before being incubated at 37°C for ~2 h.

1.2.4 LINear ACcelerator (LINAC) Synergy Agility

The LINAC is the Synergy Agility produced by ELEKTA company, whose maximum field size is 40×40 cm^2 (Fig. 1.2).

Figure 1.2 LINAC Synergy Agility, produced by ELEKTA

The gantry of this machine forms a reference system of three axes (Fig. 1.3):

- Gun-Target, which is the axis that goes head to toe of a hypothetical patient lying on the table;
- Left-Right, the axis which passes the patient horizontally;
- Top-Bottom, which goes through the patent vertically.

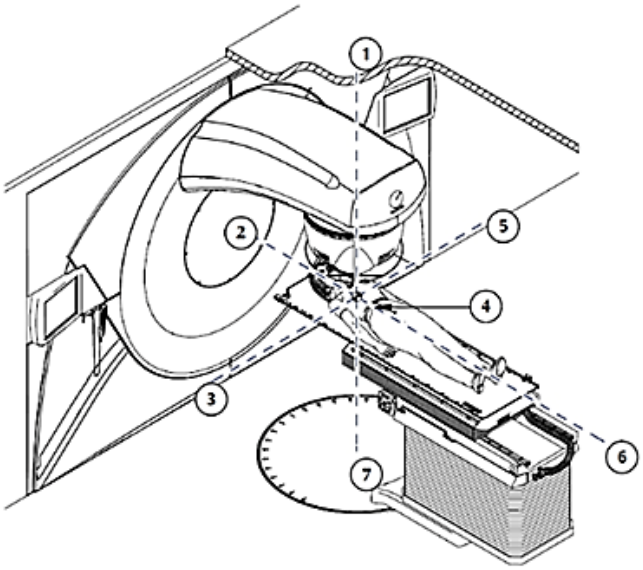

Figure 1.3 The reference system of the LINAC Synergy Agility. In particular, the gun-target axis, which goes from 2 to 6; the left-right axis, which goes from 3 to 5; and the top-bottom axis, which goes from 1 to 7. The centre of this system of reference is indicated with the number 4

The gantry Agility is characterised by having a collimator only in one direction, along the gun-target axis.

Along the left-right axis, also called the x-axis, there are 160 leaves that minimise the beam transmission, effectively making the use of a collimator unnecessary. The leaves are 0.5 cm wide and each one of them can move with a maximum velocity of 3.5 cm/s. Using a dynamic leaf guard, an entire group of leaves can be rotated at the same time and their speed can be increased up to 6.5 cm/s. It is worth mentioning that the absence of a collimator along the x-axis allows a faster modification of the irradiated field.

Along the top-bottom axis, also called the y-axis, there are two different collimators whose velocity can reach up to 9 cm/s.

The main characteristics of the gantry are reported in the following table (Tab. 1.4).

Table 1.4 LINAC technical characteristics.

Characteristic	**Dimension**
Maximum Field Size	40×40 cm^2
Leaf Width	0.5 cm
Maximum Leaf Distance from Central Axis	From -15 to 20 cm
Maximum Collimator Distance from Central Axis	From -12 to 20 cm
Leaf Thickness	9 cm
Maximum Leaf Velocity	3.5 cm/s
Maximum Collimator Velocity	9 cm/s
Maximum Gantry Velocity	5.5 °/s

The LINAC Synergy Agility produces two different kinds of beams, a photon beam and an electron one. In particular, the device allows the user the possibility of selecting one of the following beams:

- 6, 10 or 15 MV photon beam;
- 4, 6, 9, 12 or 15 MeV electron beam.

While the photon beam can be modified with a 60° wedge filter in order to obtain a filed size of 30x40 cm^2, the electron one can be adjusted with the application of different filters, such as the 4×4 cm^2 or the 25×25 cm^2 one.

Although the device offers different beams, the one used for the purpose of this project is the 6 MV photon beam, usually employed in the external beam radiotherapy.

1.2.4.1 X-Ray Volumetric Imaging system

LINAC Synergy Agility is equipped with a kilovoltage X-ray tube and a Caesium Iodine (CsI) scintillation detector. This system, in which the detector is placed orthogonally to the treatment head, is called X-ray Volumetric Imaging (XVI) system.

The XVI system is used to achieve the correct positioning of the patient on the table and can be used for image-guided radiation therapy (IGRT).

In a 360° rotation, the system can acquire an entire volume scan with an image quality slightly inferior compared to a diagnostic CT-scan. However, the scan has a duration of approximately 2 minutes, during which motion artefacts can arise.

The images produced during the scan can be acquired with three different Field Of View (FOV):

- Small, which allows volume reconstructions up to 270 mm in diameter;
- Medium, which can reconstruct images up to 410 mm in diameter;
- Large, which enables volume reconstruction up to 500 mm in diameter.

In addition to this, the device can provide a 4D acquisition during which a CT is slowly acquired. Throughout the reconstruction of the image, the patient's breathing phases are taken into consideration through the analysis of the position of the diaphragm. This analysis is given by the examination of the grey tone gradients of the image. This type of acquisition is done with a 200° rotation of the gantry, which moves with a velocity of 50°/minute. Hence, the acquired images are ~1400, which have to be divided into 10 different respiratory phases.

1.2.4.2 HexaPOD

The HexaPOD treatment table system (Fig.1.4) is a robotic carbon fibre table used to obtain, by computer controlling, the best patient positioning. This device is composed of:

– HexaPOD evo Couchtop, which is rigidly mounted on top of the standard treatment table. It can adjust not only translational errors, but rotational ones too.
– The software iGuide™, which can control the HexaPOD table.

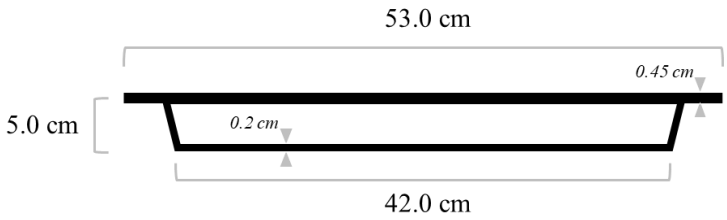

Figure 1.4 The HexaPOD table dimensional features.

The axis of the HexaPOD must be indistinguishable from the reference system formed by the gantry. If not so, translational and rotational errors may occur, and the patient could be positioned further from the optimal position that was intended.

1.2.5. Irradiation of samples

To irradiate cell samples, a treatment plan was developed. The Treatment Planning System (TPS) is usually employed in external beam radiation therapy to generate beam shape and study dose distribution to maximise tumor control and, at the same time, minimise complication to the healthy tissue. The TPS used was Monaco™, produced by ELEKTA. The dose distribution was analysed through two different plexiglass plaques, one thicker than the other, and a CT-scan was performed on them to observe their ability to attenuate X-rays. The choice of using plexiglass, which is a water-equivalent material, is due to its ability to attenuate X-rays similarly to the soft tissue. To irradiate the samples two opposing beams, at 0° and at 180°, have been used and the dose was delivered on a 20×20 cm^2 field. Through the TPS the dose has been estimated in monitor

units (MU). A MU is a measure of the output from the LINAC, and it is quantified by monitor chambers. These devices, built in the treatment head of the LINAC, are ionizing chambers that measure the dose delivered by the beam. In this project, the samples were irradiated with ~80 MUs and ~400 MUs, which are equivalent to 2 G and 10 Gy respectively, half of which were delivered at 0° and the other half, after the rotation of the gantry, at 180°. Details of the treatment plan are given in Appendix C.

The cell plates were placed between the two plaques, with the thinner one on top, upon the treatment table in order to be at the isocentre of the X-ray beam. On the thicker plaque, the cell plates were positioned in the area delimited by the masking tape and a system of two laser axis was used to centre them (Fig. 1.5).

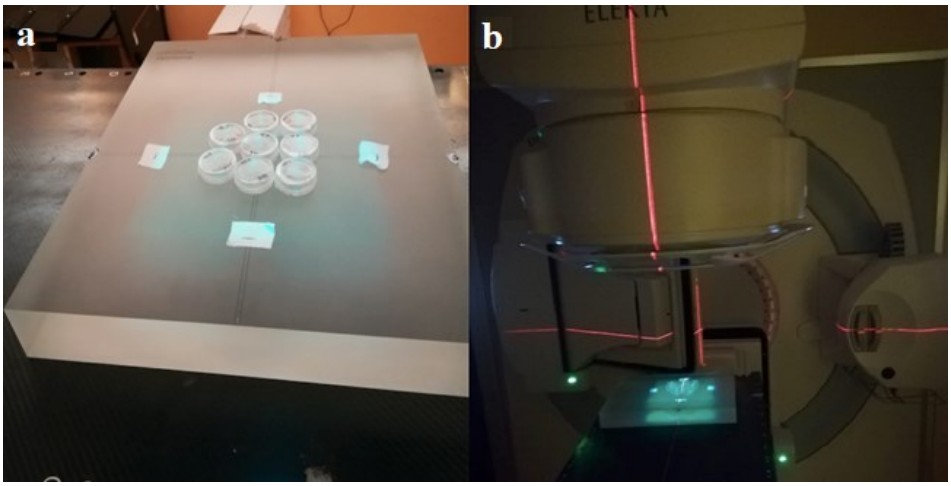

Figure 1.5 The experimental set-up. a) The plate upon which the cell samples were placed. The masking tape marks the area where the cell plates were positioned. b) System of two laser axis was used in order to centre the samples on the plate.

The first plate was 5 cm thick and was used as an anti-scatter plate. The second plaque, the thinner one (3 cm thickness), was to simulate the dose build-up effect.

1.2.6 Experimental condition

The experimental conditions included:

- healthy and breast cancer cell lines (MCF10A and MDA-MB-231, respectively);
- two substrates (1.3 and 13 kPa, simulating the healthy and the cancerous tissue, respectively);
- two doses of irradiation (2 and 10 Gy);
- two times after irradiation (24 and 72 h).

Both cell lines were seeded on the substrates with a density of ~12000 cells per cell plate. In order to preserve the cells during the transport to the facility, the medium was supplemented with HEPES Buffer (Fisher Scientific), to maintain a physiological pH despite the changes in carbon dioxide concentration.

After irradiation, the cell plates were washed in PBS 1× and new warm medium was added before incubating them at 37°C.

1.2.7 Cell Staining

To study the organization of the CSK, in particular the actin filaments, immunofluorescence was performed. The immunofluorescence procedure can be divided in four different phases:

- Fixation;
- Permeabilization;
- Blocking;
- Immunostaining.

Fixation: cells plated were cleared from the medium and 250 µL of 4% paraformaldehyde, pre-heated to 37 °C, was added to each plate. Paraformaldehyde is the most used fixative and its function is to

chemically bond adjacent macromolecules, such as proteins, together. This process is called cross-linking. After 15 minutes, the cell plates were washed with PBS 1×.

Permeabilization: t-Octylphenoxypolyethoxyethanol, Polyethylene glycol tert-octylphenyl ether (Triton-X 100), diluted at 0.1% in PBS 1×, introduces a detergent monomer into the lipid membrane to permeabilize it.

Blocking: it is usually performed with a solution of excess proteins and its goal is to decrease the amount of nonspecific binding in the biological sample. Thereby, there is a reduction of background staining, mostly given by the interactions between the antibody and non-target molecules, effectively making easier to identify the correct signal and have a cleaner result. To do that, cell plates were incubated with 200 µL of 10% Bovine Serum Albumin (BSA) in PBS 1× for 1 hour at room temperature.

Immunostaining for mechanosensing: to label the actin filaments, the antibody Alexa Flour™ 488 Phalloidin (Fischer Scientific), was diluted at 1:200 in 0.1% BSA solution in PBS 1× and 200 µL of the solution was added to each cell plate. After leaving the solution overnight, the samples were washed with PBS 1× several times. To label nuclei, Hoechst 33342 (Fisher Scientific) fluorescent dye, which is a cell-permeable DNA stain that emits blue fluorescence at 460 to 490 nm, was employed. The fluorophore was diluted at 1:10000 in 0.1% BSA solution in PBS 1× and 200 µl of the solution was added to each sample. After 10 minutes, the cell plates were washed twice in PBS 1× and then covered with PBS 1×.

Immunostaining for mechanotrasduction: YAP was localized by YAP1 polyclonal rabbit antibody (PA1–46189, ThermoFisher Scientific) and Alexa546 mouse anti-rabbit secondary antibody. Lamin A/C was localized

by mouse monoclonal lamin A/C antibody (Santacruz, SC-376248) and Alexa488 goat anti-mouse secondary antibodies (Life Technologies, A11008). Cell plates were washed 2 times in PBS 1× and then covered with PBS 1×.

All samples were always wrapped in aluminium foil to avoid fluorophore bleaching and stored at 4 °C.

1.2.8 Inverted microscope and acquisition

Cells images were acquired with Olympus IX81 inverted microscope (Figure 3.12), fully motorised, and designed for long-term imaging of living cells. It is provided with an environmental chamber that maintains the physiological values of temperature (37 °C), CO_2 levels (~5%), and humidity.

In the inverted configuration, the beam propagates from the bottom upwards and the scattering force that pushes the particle upwards is therefore opposite to the force of gravity, thus ensuring good axial stability. The microscope is equipped with (i) beam-splitter that deflects the laser beam towards the entrance opening of the objective and passes the light of the sample illumination lamp until it reaches the eyepieces; (ii) the condenser lens serves to convey the light coming from the illumination lamp onto the sample and to collect the scattered laser radiation and not from the sample to send it to the position sensor; (iii) the objectives.

There are different objectives available, which are 4×, 10×, 20×, 40× dry and 60× and 100× oil immersion. In addition to this, Fig. 1.6 shows the lenses system designed to maximise signal-to-noise (S/N) ratio and optical performance for live cell fluorescent imaging. The acquisitions were carried out for cell spreading and cell migration analysis.

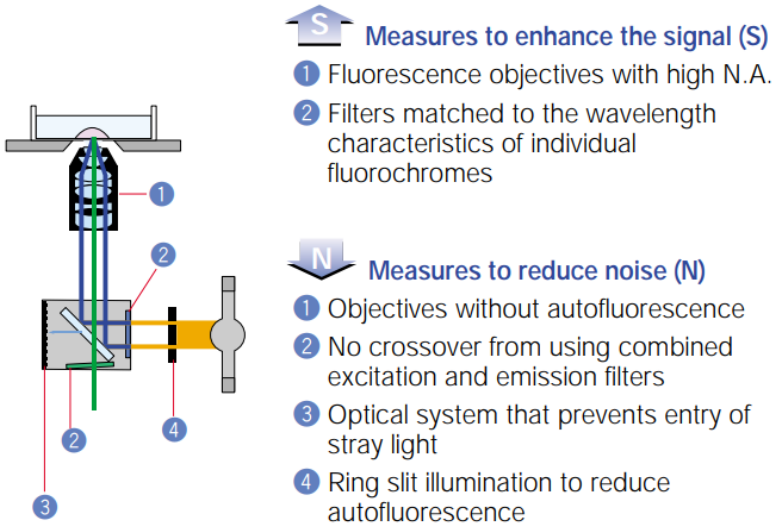

Figure 1.6 Lens system to maximise S/N. Adapted from [68].

- **Cells spreading**

To investigate cells spreading, the fluorescence images were acquired with 10× objective. The examination of morphology and CSK structure was conducted both in control condition, before the irradiation of the samples, and after the treatment with two doses of X-ray. In order to evaluate cells spreading, through the delineation of cells contours, ImageJ Fiji software (NIH, Bethesda, MD, USA) was employed. To measure the cell area, a thresholding process was used on each image and the cell of interest was detected through the selection tools offered by the software (Fig. 1.7).

The measurements of interest, which are Area, Perimeter and Fit Ellipse, were selected through the command "set measurements" available in the Analyse Menu. After selecting all cells in the image, each Region of Interest (ROI) was recorded through the tool ROI manager. Afterwards,

the measures were shown in a popup box and stored in a folder. The same procedure was applied to nuclei images too.

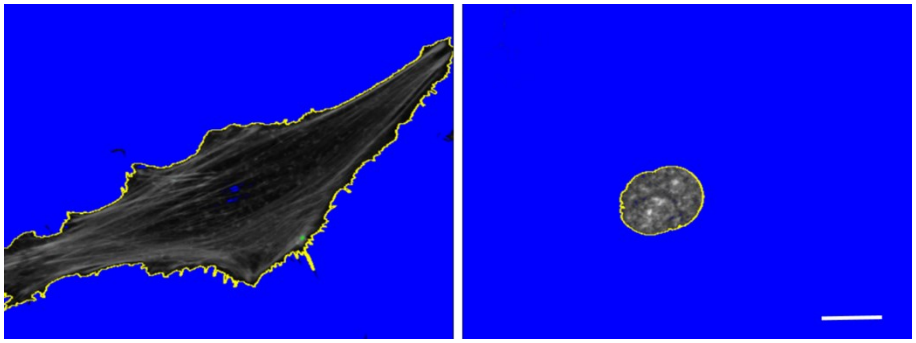

Figure 1.7 Cell spreading analysis. Both cells and nuclei of interest are selected and represented with the yellow contour. Scale bar:15 µm

- **Cell Migration**

Migration analysis was performed with the use of time-lapse microscopy. Microscope images are recorded and then observed at a greater speed, due to the velocity of cells movements. In fact, since cells move with a rate of a few µm/minute, the images acquired are speeded up in order to give an accelerated view of the microscopic process.

The images were acquired with Olympus IX81 microscopy system with a 4× objective. The cell plates were placed in the incubator featured in the microscope to keep a suitable environment for the living cells.

Cells movements were tracked by taking pictures of 10 different regions for each sample at regular intervals of 10 minutes. The entire procedure lasted 24 h to obtain videos of 144 frames.

The migration analysis was performed with ImageJ Fiji software for all cells of interest that remained in the video for the entire recording time. Two different plug-ins were employed:

– Manual tracking;

– Chemotaxis tool.

The first plug-in, after the definition of same parameters as the x/y calibration and the time interval between two consecutive frames, allows the user to obtain a pop-up table with the list of XY coordinates, velocity and distance covered between two frames, by clicking on the cell of interest.

In order to determine cells trajectories, the position of each cell, in particular the cell centroid, has been marked in every frame (Fig. 1.8). This tracking method was performed manually with the point and click system and the track of each cell was stored in a folder.

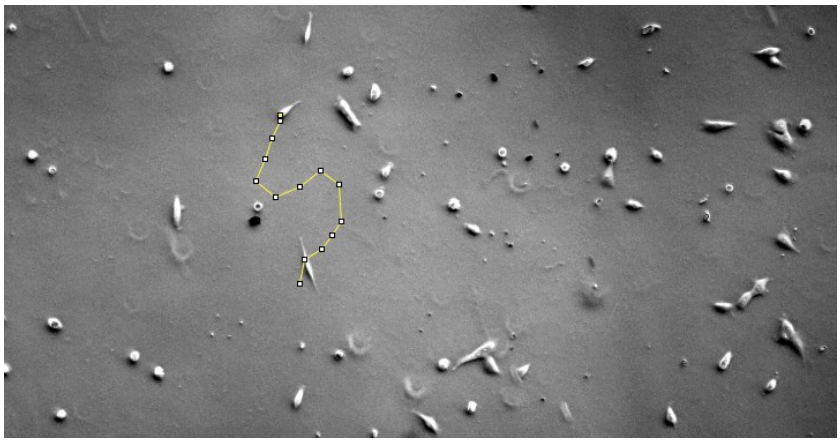

Figure 1.8 The trajectory of each cell was reconstructed manually (yellow line) by marking the centroid of the cell in each frame.

The Chemotaxis tool is a plug-in which offers several graphs and statistical test that allows advanced analysis of chemotaxis experiments. After setting the aforementioned parameters, the tracks obtained with Manual Tracking can be loaded into the Chemotaxis Tool and be used to evaluate some static features.

In the case at hand, the plug-in was used to calculate the velocity and directionality.

In addition, to describe the efficiency of cell migration, another parameter has been calculated: the persistence. It describes the time a cell employs to change its direction and is generally higher in tumor cells that not only move faster, but also more directionally. To determine the persistence, the mean square displacement (MSD) of each cell was calculated. MSDs were estimated starting from trajectories using the following formula:

$$MSD(\tau) = \langle [x(t-\tau) - x(t)]^2 + [y(t-\tau) - y(t)]^2 \rangle \qquad (1)$$

where t is the time and τ is the lag time.

To estimate diffusion coefficient D and directional persistence P, MSDs curves were fitted with the Fürth's Formula:

$$MSD(\tau) = 4D\left(\tau - P\left(1 - e^{-\frac{\tau}{P}}\right)\right) \qquad (2)$$

The fitting was done with ordinary nonlinear least-squares regression analysis.

- **Biophysical migration parameters**

Single cell trajectories were determined using ImageJ and Manual Tracking plugin (http://rsweb.nih.gov/ij/). Their orientation was calculated by using the ellipse-fitting function in ImageJ and, then, cell trajectories were rigidly rotated around the starting point P(x(0), y(0)) by using the rotation matrix as represented in Fig. 1.9. After the coordinate transformation, we obtained the new coordinates x′(t) and y′(t) at every time t and the principal direction of the rotated trajectory results to be aligned to y′-axis. Once rotated, the net displacements travelled along x′- and y′-directions were calculated as follows:

$$\Delta x' = x'_{max} - x'_{min} \quad (3)$$

$$y'_{max} - y'_{min} \quad (4)$$

where x′/y ′$_{max}$ and x′/y ′$_{min}$ are the maximum ad the minimum values of the rotated coordinates x′ and y′.

The **trajectory extension ratio (TER)** and the **area traveled (AT)** were calculated with the following expressions

$$TER = \frac{\Delta_{x\prime}}{\Delta_{y\prime}} \quad (5)$$

$$AT = \frac{\pi\, \Delta x' \Delta y'}{4} \quad (6)$$

TER can vary between 0 and 1 and is inversely related to the directionality of the cells: values close to 1 indicate random trajectories, while when TER approaches 0 the trajectories are approximated with a straight line.

MSD on x′- and y′- directions (MSD_x and MSD_y) were calculated, starting from rotated trajectories, using the following formula:

$$MS(\tau) = \langle [x(t-\tau) - x(t)]^2 \rangle \quad (7)$$

$$MSD(\tau) = \langle [y(t-\tau) - y(t)]^2 \rangle \quad (8)$$

where x′ (t) and y′(t) are the rotated coordinates of cell at time t, τ is the lag time and < > indicated the temporal mean.

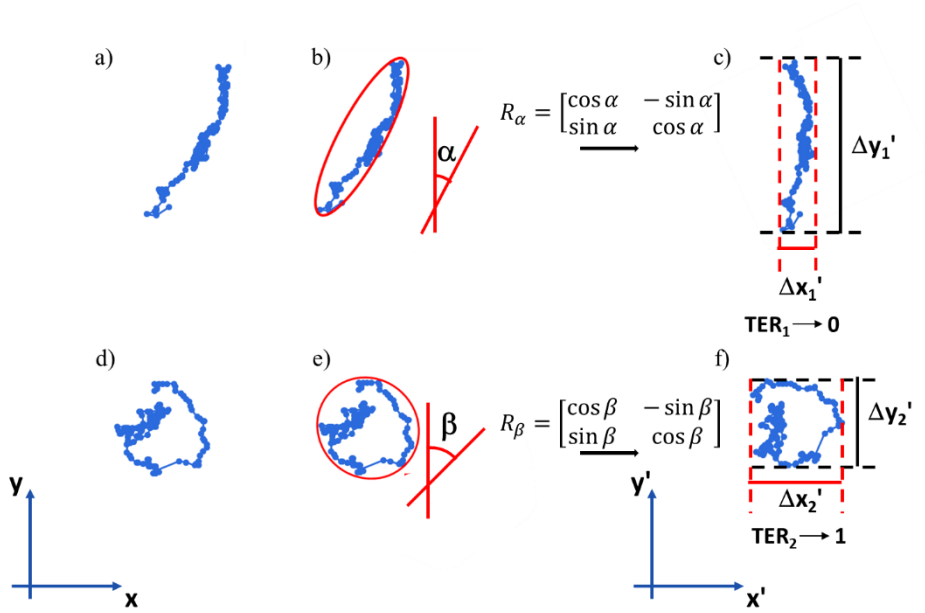

Figure 1.9 Examples of cell trajectories (a-d) in the reference system. Their orientations α and β are calculated using the fitting-ellipse function in Image J (b-e) and then the rotation matrices R_α and R_β rotate the trajectories in the new reference system x′-y′ (c-f).

Individual cells, identified by visualization of single nuclei, were outlined and changes in cell shape in control and irradiated conditions were quantified by two morphological parameters, the shape factor (SF) and circularity index (CI), defined as follows:

$$SF = \frac{4\,\pi\,A}{P^2} \quad (9)$$

$$CI = \frac{axis_{minor}}{axis_{major}} \quad (10)$$

where A and P are the area and the perimeter of cells calculated by using the "Measure" command in ImageJ, whereas $axis_{major}$ and $axis_{minor}$ are the major and the minor axis of the best-fitting ellipse determined by using the ellipse-fitting function in ImageJ.

Both parameters can change between 0 and 1, where the upper limit connotes a perfect circular cell, while the lower limit indicates, in the case of SF, a cell with very pronounced edge roughness and, in the case of CI, a cell that can be approximated with a straight line.

1.2.9 Confocal microscope and acquisition

LSM-800 confocal microscope (Zeiss) was used for cell acquisition.

A confocal microscope is a particular type of microscope with increased resolution and contrast. The basic components of this machine are the pinholes, the objective lenses, low-noise detectors, fast scanning mirrors, filters for wavelength selection and laser illumination. In particular, it uses pinholes to block out-of-focus light in image formation, because thicker samples tend to scatter light also below the focal plane of the objective. Using confocal microscopy, the illumination and detection optics are always focused on the same spot on the sample, and the image is reconstructed by moving the light across the sample itself, so that anything outside the focusing spot does not contribute to the image formation. To acquire a z-stack, the focal point is changed, and the scanning process is repeated over the new slice.

To quantify **YAP** concentration and **lamin A/C** level in cells, the samples were observed with LSM710 confocal microscope (Carl Zeiss Inc., Peabody, MA, USA) with a 63× objective. 10 z-stack images, averaging 4 frames each acquisition and with a bit depth of 12 bit, were

acquired for each sample. Each image was characterized by a size of 13.8 μm × 13.8 μm with a pixel size of 0.13 μm.

Z-stacks for the red channel (YAP) were projected into a single image using the 'sum projection' function in ImageJ. YAP and lamin A/C images were used to extract individual cellular and nuclear outlines using ImageJ ROI manager tool and YAP expression at each condition was evaluated in terms of integrated fluorescence intensity within individual cellular and nuclear boundaries, Y_C and Y_N, respectively. The total YAP expression in the cytoplasm was calculated as difference between Y_C and Y_N. Then, the following parameters were evaluated:

$$Y_{N/C} = \frac{Y_N}{Y_C} \tag{11}$$

representing nuclear to cytoplasmic ratio of total YAP. Values lower or higher than 1 indicate prevalent localization of YAP in the cytoplasm or in the nucleus, respectively.

The individual intensities of YAP, in the nucleus and in the cytoplasm, were calculated according to:

$$Y_N^d = \frac{Y_N}{A_N} \tag{12}$$

$$Y_C^d = \frac{Y_C}{A_{Cell} - A_N} \tag{13}$$

where A_N and A_C are the nucleus and the cytoplasm area, whereas Y_N^d and Y_C^d represent the nuclear and cytoplasmic density/concentration of YAP, respectively.

Finally, the nuclear to cytoplasmic ratio of YAP density was calculated:

$$Y_{N/C}^{d} = \frac{Y_N^d}{Y_C^d} \tag{14}$$

This parameter is the most used to study the effects of translocation processes from nucleus to cytoplasm and *vice versa* and indicates if YAP is more concentrated into the cytoplasm ($Y_{N/C}^{d} \ll 1$) or in the cytoplasm ($Y_{N/C}^{d} \gg 1$).

To quantify lamin A/C level, the z-stacks for the green channel (lamin A/C) were projected into a single image using the 'maximum projection' function in ImageJ. Then, lamin A/C expression at each condition was evaluated in terms of integrated fluorescence intensity within individual nuclear boundaries.

1.2.10 Statistical Analysis

Experiments were performed in duplicate, both before and after irradiation. Data obtained in the migration and spreading analysis were used to calculate the median, the first and the third quartile of each measurement of interest.

Statistical analysis was performed with KaleidaGraph, a software that offers statistics, linear and nonlinear curve fitting and allows the user to easily manipulate and analyse data. KaleidaGraph presents a variety of basic statistics, such as the Student's t-test or ANOVA (Analysis of Variance) test. In this project, the differences between each condition were determined through the comparison between pairs of samples with the Kruskal-Wallis test (Appendix D)

Statistical difference was shown as: *P<0,05; **P < 0,01; ***P < 0,001.

1.3 Results and discussion

This paragraph shows the results of the effect of ionizing radiation on cell spreading, migration, biophysical migration parameters and YAP expression. These parameters were investigated by considering two substrates of different stiffnesses (which simulate the stiffness of a healthy and a tumor tissue) and irradiating the samples at two doses of photons (2 and 10 Gy). The analyses were performed at two times after irradiationt: 24 and 72 h

The experimental activity was carried out thanks to the collaboration with various departments of the University of Naples Federico II: Interdepartmental Research Center on Biomaterials and the Department of Chemistry, Materials and Production Engineering (for sample preparation and acquisition by microscopes), Istituto Nazionale Tumori IRCCS Fondazione G. Pascale, in Naples (for radiotherapy treatment), and Istituto Italiano di Tecnologia (IIT), in Naples (for acquisition facilities).

1.3.1 Spreading Analysis Results

The correlation between ECM mechanical properties and some biological processes, such as cell adhesion, is closely related to myosin-tension formation within actin stress fibres and FAs. In this way, CSK can transmit mechanical forces to the nucleus, modifying its shape, distorting the nuclear envelope and evoking biochemical responses thanks to LINC complex [69].

As parameters for evaluating cell adhesion, and direct effects on nuclei, spreading and nuclear area of both MCF10A and MDA-MB-231 cells were investigated. Phase of the cell cycle was not considered; in this way it was also possible to consider the variability of cases similar to the in vivo condition.

Study of mechanosensing ability was conducted for both cell lines in control condition, and then the samples were irradiated to investigate the effects of X-rays at 24 and 72 h after treatment. Fig. 1.10 shows a summary panel of all the experimental conditions used with two-color channels (actin in green, and nuclei in blue) and their merge, by summing the z-stack projections.

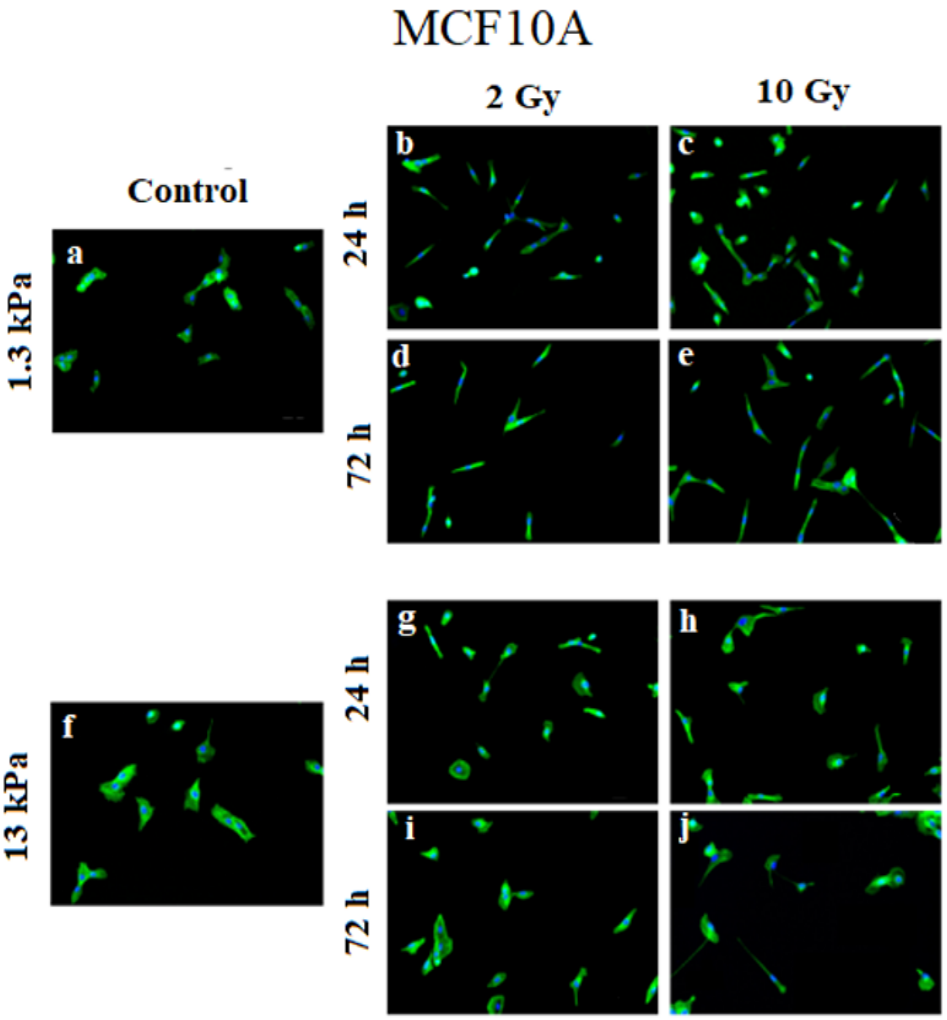

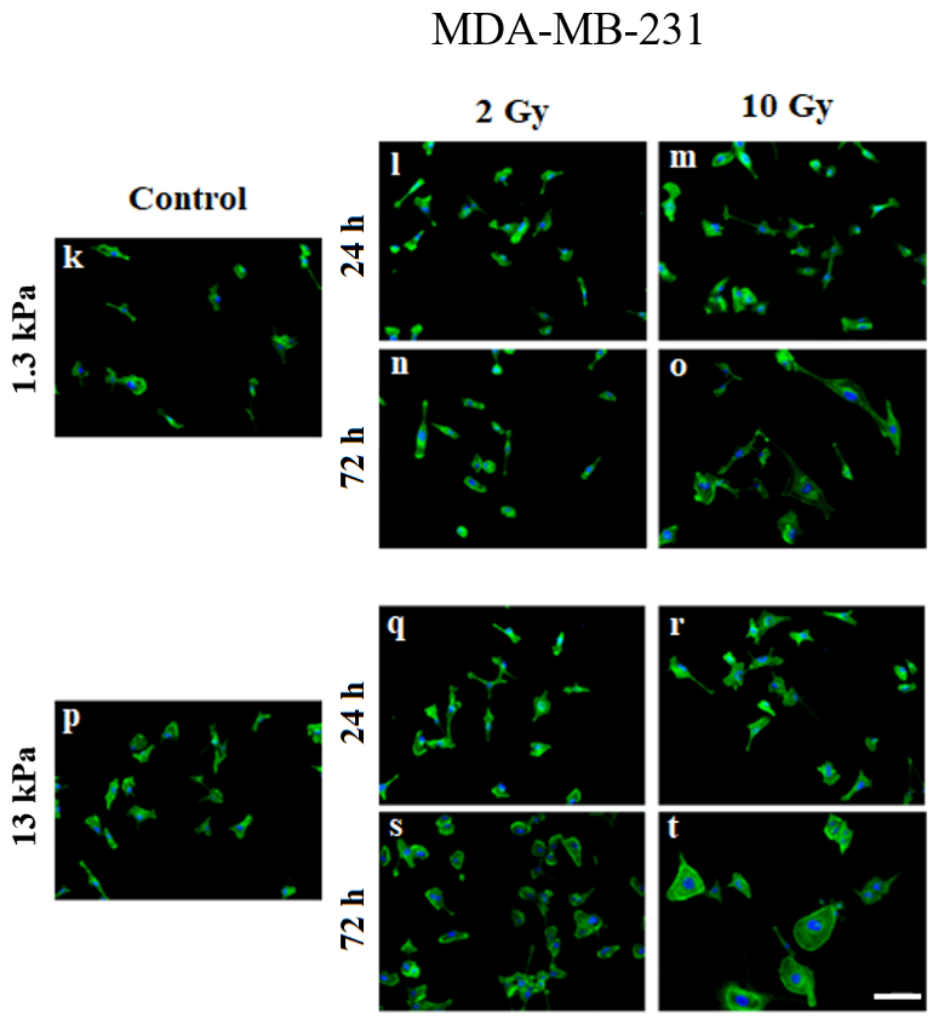

Figure 1.10 Panel of representative images of spreading of MCF10A (a-j) and MDA-MB-231 (k-t) in all experimental conditions. Cells were stained for F-actin (green) and nuclear DNA (blue). Scale bar:50 µm.

Data obtained from images analysis are shown in Fig. 1.11 and reported in Tab. 1.5 and 1.6. Statistical analyses are reported in Annex I

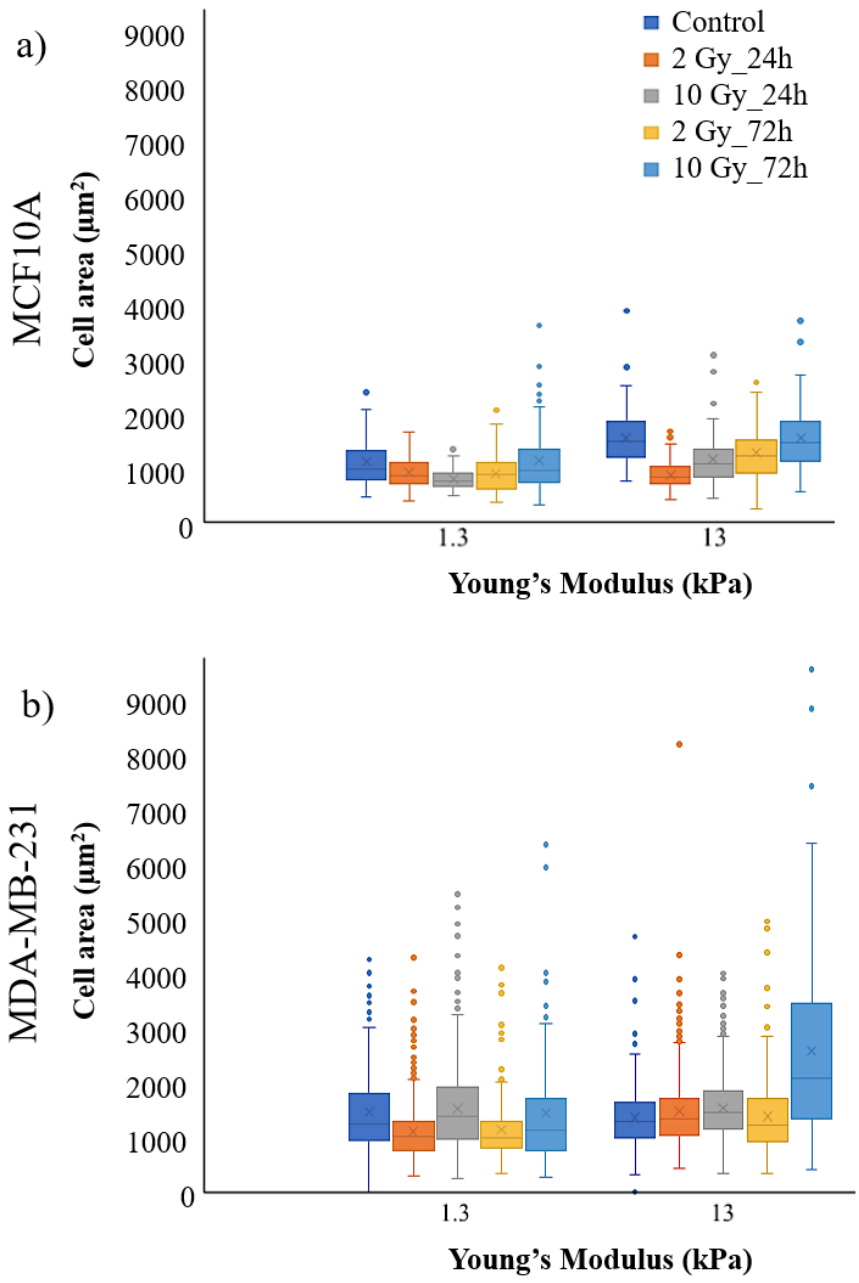
a)
MCF10A
Cell area (µm²)
9000
8000
7000
6000
5000
4000
3000
2000
1000
0
Control
2 Gy_24h
10 Gy_24h
2 Gy_72h
10 Gy_72h
1.3
13
Young's Modulus (kPa)
b)
MDA-MB-231
Cell area (µm²)
9000
8000
7000
6000
5000
4000
3000
2000
1000
0
1.3
13
Young's Modulus (kPa)

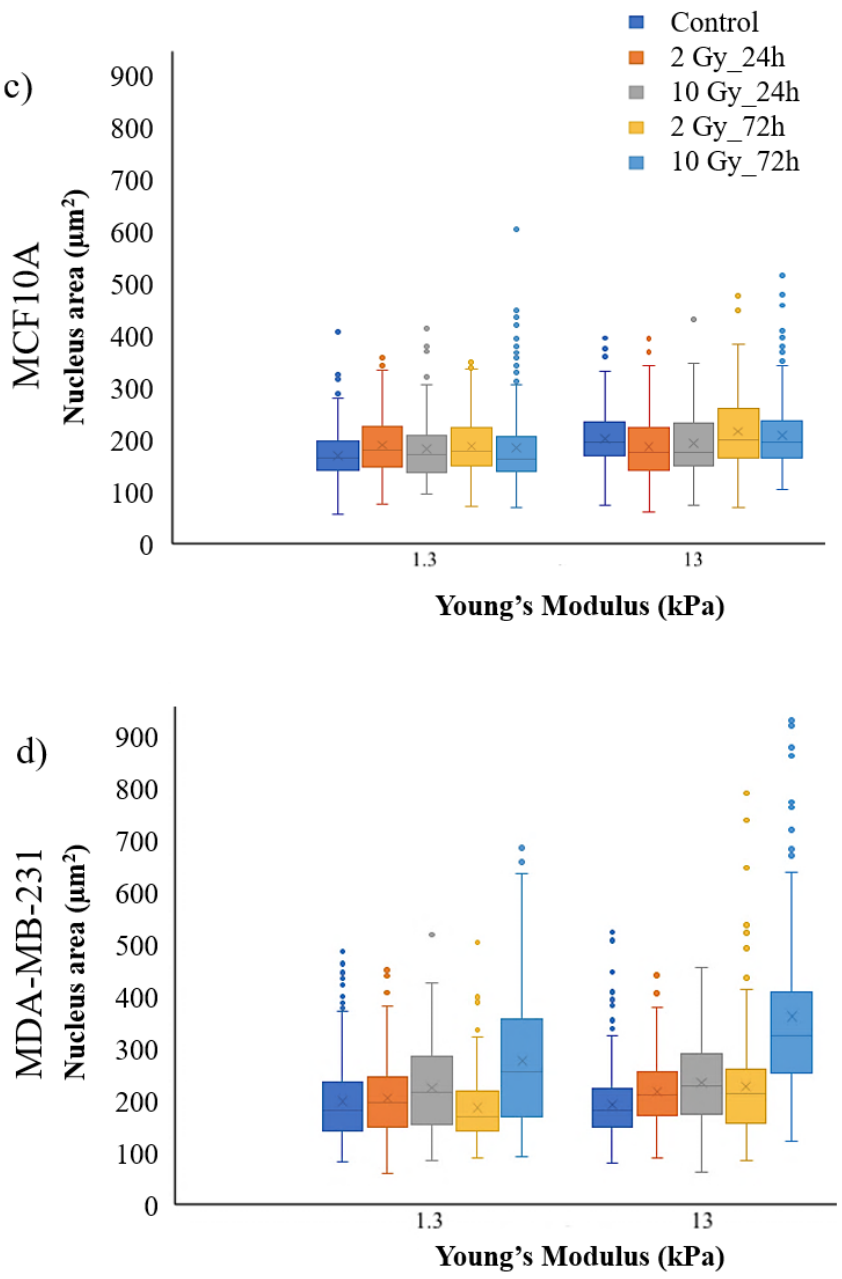

Figure 1.11 Box plots (mean, median, interquartile range, and outliers) of spreading areas (a-b) and nuclei areas (c-d). n>60 for cell spreading data, n>110 for nucleus data.

Table 1.5 Median values of cell area in experimental conditions.

Dose (Gy)	***Time after irradiation (h)***	***Young's Modulus (kPa)***	***Median MCF10A (μm^2)***	***Median MDA-MB-231 (μm^2)***
Control		1.3	932.515	1140.500
		13	1404.699	1179.000
2	24	1.3	805.905	921.550
		13	791.916	906.500
10	24	1.3	824.556	1263.500
		13	1147.948	1033.250
2	72	1.3	711.740	1288.000
		13	1019.103	1132.000
10	72	1.3	909.556	1333.000
		13	1386.436	1925.000

Table 1.6 Median values of nucleus area in experimental conditions

Dose (Gy)	***Time after irradiation (h)***	***Young's Modulus (kPa)***	***Median MCF10A (μm^2)***	***Median MDA-MB-231 (μm^2)***
control		1.3	155.800	164.700
		13	185.150	165.350
2	24	1.3	170.000	179.750
		13	166.650	191.650
10	24	1.3	161.700	197.750
		13	165.700	208.900
2	72	1.3	169.150	154.300
		13	189.400	194.000
10	72	1.3	153.500	232.500
		13	185.550	298.000

Spreading analysis show that while in healthy cells different substrate stiffnesses entails different levels of spreading and nuclear area, in cancerous cells, these characteristics turn out to be independent of the stiffness of the substrate they are seeded on, confirming a compromised mechanosensing system.

After irradiation, MCF10A cells were less spread compared to the control ones. This outcome has been observed in all conditions, and in

particular on the stiffer substrate, after irradiation with the lower dose (cell area ~800 μm^2). Investigating the nucleus area, an increase in the nuclear area of cells on soft substrates and irradiated with both low and high dose was observed. It can be assumed that this effect is due to a defence mechanism, controlled by microtubules and intermediate filaments and activated by the microenvironment. On the stiffer substrate, however, nuclear area appeared to be reduced together with spreading area. Analysis performed 72 h after irradiation shows that cells irradiated with 2 Gy exhibited a decrease in the spreading area on both substrates, in accordance with the results obtained from 24 h analysis. Cells on which the higher dose was delivered were able to restore their spreading area to their initial values.

On the other hand, MDA-MB-231 cells were found to be more sensitive to both doses of irradiation, although the effects of radiotherapy changed profoundly over time and with doses. 24 h after irradiation, MDA-MB-231 cells on the softer substrate showed a decrease in the spreading area when irradiated with 2 Gy. This phenomenon was not observed in cells irradiated with 10 Gy, in which the spreading area is equal to that of the control. Therefore, higher dose does not seem to affect cells on the softer substrate. This is probably due to the protective function of the microenvironment, which simulate the healthy tissue, on cells. Considering the stiffer substrate, it is noticeable how cells showed a different behaviour. The spreading area, in fact, increases in the 24 h following irradiation for both doses. After 72 h, only cells on stiff substrate irradiated with 2 Gy were able to restore their original spreading values, while the spreading area of cells treated with the higher dose result to be 1.9-fold higher than that of the control condition (1925.000 μm^2 at 10 Gy, versus 1179.000 μm^2 of control). Finally, the higher dose induced a

significant increase in the nuclear area indicating that the tumor cells, unlike the healthy ones, were more sensitive to 10 Gy than to the 2 Gy dose.

Examining the results, it is clear that radiations had a less relevant impact on healthy cells than cancerous ones. This phenomenon indicates that the MCF10A cell line has a stronger ability to preserve its assets on both substrates, and confirm that substrates, which simulated healthy ECM, have a radioprotective effect on cells [54].

1.3.2 Migration Analysis Results

Cell motility is a complex process requiring repeated cycles of adhesion to and detachment from the ECM, strictly related to the FA life cycle (assembly–maturation–disassembly). In order to study the migration ability of both MCF10A and MDA-MB-231 cell lines, two different parameters were estimated: velocity and persistence, the latter representing the capability of cells to change direction during their motion.

Since these are 2D models, the O_2 concentration is assumed to be equal to that in the medium, therefore the influence of hypoxia on the ETM has not been considered.

Cells speed was estimated by the manual reconstruction of cells trajectories. Data obtained are shown in Fig. 1.12 and reported in Fig. 1.13, and Tab. 1.7. Statistical Analysis are reported in Annex II.

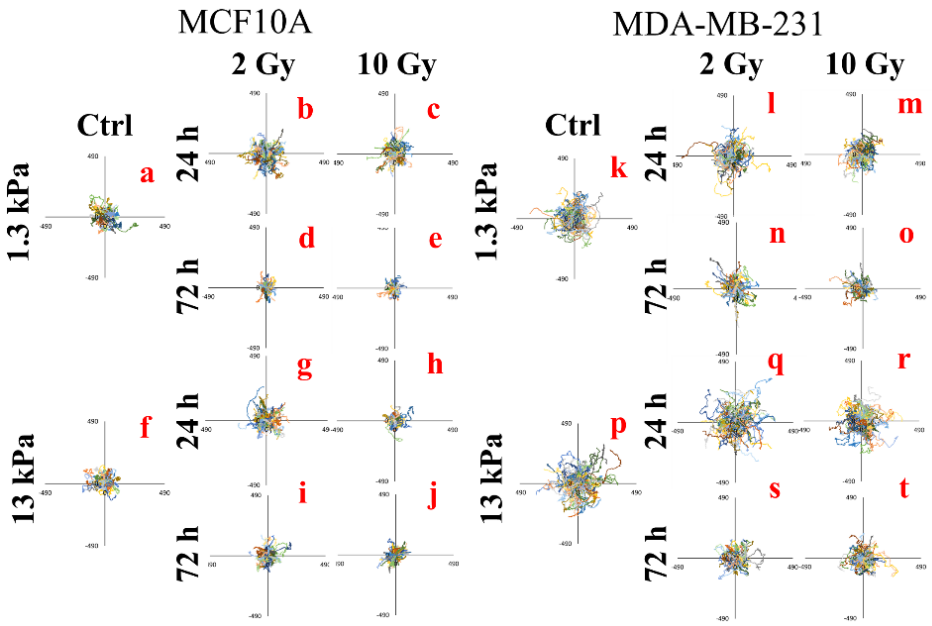

Figure 1.12 Plot at origin of trajectories of MCF10A and MDA-MB-231 before (a,f,k,p) and after RT (b-e,g-j,l-o,q-t). n>58 for all conditions.

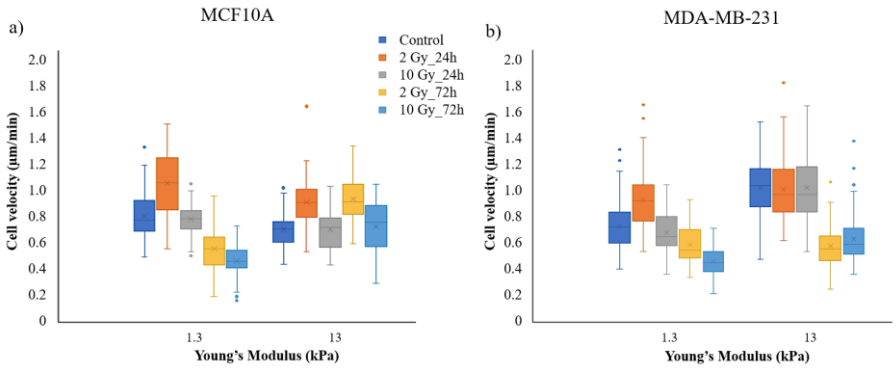

Figure 1.13 Box plots (mean, median, interquartile range, and outliers) of migration velocity of MCF10A (a) and MDA-MB-231(b) in all experimental conditions. n>58 for all conditions.

Table 1.7 Median values of velocity in all experimental conditions

Dose (Gy)	***Time after irradiation (h)***	***Young's Modulus (kPa)***	***Median MCF10A (µm/min)***	***Median MDA-MB-231 (µm/min)***
control		1.3	0.8	0.7
		13	0.7	1.0
2	24	1.3	1.0	0.9
		13	0.9	0.9
10	24	1.3	0.8	0.6
		13	0.7	0.9
2	72	1.3	0.5	0.5
		13	0.9	0.5
10	72	1.3	0.5	0.4
		13	0.7	0.6

MCF10A cells in control condition presented a higher velocity value on the softer substrate than on the stiffer one, effectively meaning that the speed of healthy cells is inversely proportional to the Young' Modulus of the substrate. This effect can be explained considering that migration velocity depends on different cycles of adhesion and deadhesion from the ECM. Several researches have shown that with increasing substrates stiffness on which cells have been grown there is a more organised CSK. In fact, in these circumstances, cells form bigger stress fibres and longer FAs. Longer FAs require a longer time to assemble and disassemble, leading to a decrease in cells velocity.

Conversely, the velocity of cancerous cells showed the opposite trend. MDA-MB-231 cell velocity increased with increasing stiffness of the substrate. Furthermore, results showed that MDA-MB-231 cells velocity is higher than that of the other cell line. In particular, the higher speed of cancerous cells is justified by the less organized CSK of tumoral cells. In fact, cells with a more organized CSK, such as the MCF10A, have higher mechanical properties and have a greater ability to form mature FAs. In addition to this, malignant cells, due to ECM stiffening, show high levels

of FAK, a non-receptor tyrosine kinase involved in the process of disassembling of FAs. Thus, the presence of high levels of FAK in tumoral cells promotes the increase in the assembly/disassembly rate of FAs and disallow the formation of a more organized CSK, leading to an increase in migration velocity and tumor cells invasion.

MCF10A cells, 24 h from irradiation, showed an increase in the velocity on both substrates. This effect was distinctive of lower doses, due to the reduced adhesion. The higher dose did not cause any significant change respect to control condition. There was a decrease in migration velocity for cells on soft substrates and analysed 72 h after irradiation. This data is in partial accordance with radiotherapy effect on the adhesion. In fact, cells treated with higher doses showed an increase in their adhesion ability, while the opposite effect was observed with cells irradiated with 2 Gy.

Based on the data gathered in the cell adhesion analysis, it is evident that lower doses produce more durable effects, especially on stiffer substrates, that promote the decrease in the spreading area and the enhancement of migration velocity.

MDA-MB-231 cell line showed a different response to radiations. Cells on the soft substrate, 24 h after irradiation, reacted by increasing their velocity when irradiated with 2 Gy. At 72 h from irradiation, however, there was a trend reversal since the increase of adhesions led cells to move slower. The analysis of cells velocity, when irradiated with 10 Gy, reported a time-dependent reduction of speed.

Conversely, velocity of cells on stiffer substrate and analysed 24 h after irradiation resulted equal to that of the control condition. Regardless, the examination of samples 72 h after irradiation showed a reduction in the

speed independently from the dose delivered. This effect was probably due to the increased adhesion.

As previously mentioned, another fundamental element estimated in the migration analysis was the **directional persistence** of both cell lines. Whereas the migration velocity is easy to calculate and interpret, the persistence describes the time a cell employs to change its direction and has been estimated by fitting the MSD over time with the Fürth's formula (2). Data obtained are shown in Fig. 1.14 and reported in Tab. 1.8.

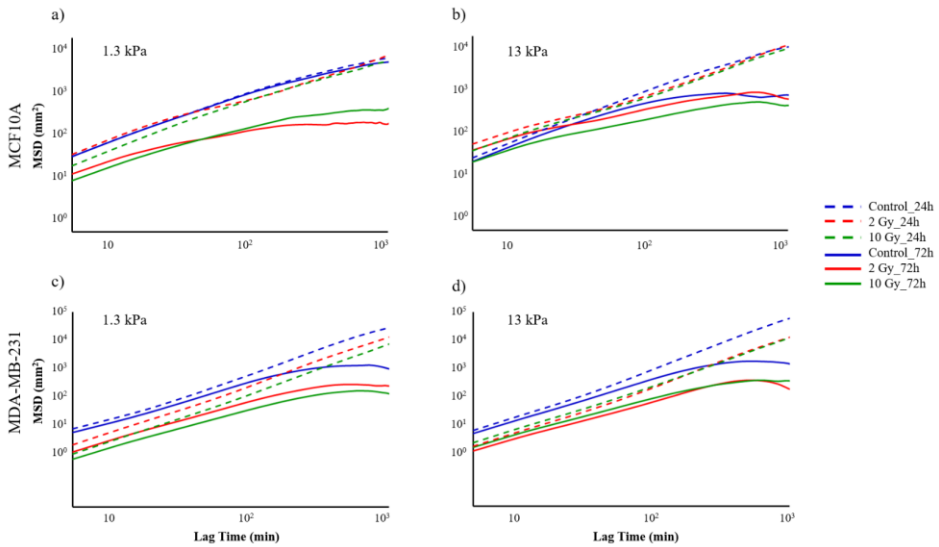

Figure 1.14 MSDs calculated from cell trajectories of MCF10A (top) and MDA-MB-231(bottom) on soft (a,c) and stiff (b,d) substrates.

Table 1.8 Values of diffusion coefficient (D), persistence (P) and goodness-of-fit (R^2) are listed. These values were obtained by fitting the MSD of both cell lines' trajectories over time.

		Young's Modulus (kPa)	MCF10A			MDA-MB-231		
			D (μm^2/min)	P (min)	R^2	D (μm^2/min)	P (min)	R^2
Control		1.3	3.199	0.018	0.919	13.009	59.776	0.999
		13	3.030	0.018	0.978	21.469	114.917	0.999
2 Gy	**24 h**	1.3	6.675	19.545	0.999	11.833	62.148	0.999
		13	7.141	73.785	0.999	22.158	112.105	0.999
	72 h	1.3	2.000	48.350	0.999	6.739	84.944	0.999
		13	3.263	17.531	0.991	7.305	122.016	0.999
10 Gy	**24 h**	1.3	5.231	35.773	0.999	7.595	97.893	0.999
		13	2.577	0.016	0.976	12.087	71.349	0.999
	72 h	1.3	1.751	0.094	0.999	4.338	103.996	0.999
		13	2.901	25.736	0.999	6.487	100.964	0.999

The persistence time of healthy cells approached to 0, showing that MCF10A cells move with a random Brownian motion. This effect was observed on both substrates.

MCF10A cells, 24 after irradiation, at a dose of 2 Gy, showed an increase in the directional persistence time compared to that of cells in control condition. This effect was observed on both substrates. However, 72 h after irradiation, there was a decrease in the persistence of cells grown on the stiffer substrate (17.531 min). Considering 10 Gy dose, an increase in the persistence was observed 24 h after irradiation and in cells seeded on the softer substrate (35.773 min.). Conversely, cells grown on the stiffer substrate showed a reduction in their persistence, which was equal to control condition. This trend was completely reversed in the analysis of the samples 72 h after irradiation. All these effects imply that irradiation can have a strong impact on healthy samples.

The MDA-MB-231 cell line, compared to its healthy counterpart, was more directionally stable on both substrates stiffnesses. In fact, the

persistence time resulted ~1 hour and ~2 h on soft and stiff substrates, respectively. This result suggested that the ECM stiffening stimulates malignant cells to invade other sites by increasing their directional persistence. MDA-MB-231 cells not only changed their velocity after irradiation, but also their persistence time. In all analysed conditions, however, their persistence time remained over 1 hour. In particular, cells grown on soft substrate and irradiated with a dose of 10 Gy produced a time-dependent increase in the directional persistence. These effects can be explained considering that cancerous cells have a higher ability to preserve their original condition. Specifically, the MDA-MB-231 cell line proved to be able to maintain a high directional stability in its motion.

MCF10A cells, 24 after irradiation and regarding a dose of 2 Gy, showed an increase in the directional persistence time compared to that of the control condition. This effect was observed on both substrates. However, 72 h after the dose was delivered, there was a decrease in the persistence of cells grown on the stiffer substrate. Considering the higher dose, an increase in the persistence was observed 24 h after irradiation and in cells seeded on the softer substrate. Conversely, cells grown on the stiffer substrate showed a reduction in their persistence, which was equal to that of the control condition. This trend was completely reversed in the analysis of the samples 72 h after irradiation. All these effects imply that irradiation can have a strong impact on healthy samples.

MDA-MB-231 cells not only changed their velocity after irradiation, but also their persistence time. In all analysed conditions, however, their persistence time remained over 1 hour. In particular, cells grown on soft substrate and irradiated with a dose of 10 Gy produced a time-dependent increase in the directional persistence. These effects can be explained

considering that cancerous cells have a higher ability to preserve their original condition. Specifically, the MDA-MB-231 cell line proved to be able to maintain a high directional stability in its motion, however, it does not seem to be affected by any kind of gradient as no clear direction emerges.

1.3.3. Biophysical migration parameters

Cell trajectory and the area travelled by the cell, represent two other parameters that indicate not only the state of cell adhesion, but also the cellular polarization, a prerequisite for directional movement, and the formation of protrusions on the cell perimeters. The study aimed at analysing the tendency of healthy and metastatic tumor cells to move in a directional way when interacting with different stiffness substrates and after exposure to ionizing radiation [70].

To describe the ability of cells to move and their tendency to do so in a directional way, **TER, the displacement along the principal direction y′**, and **AT** were analysed, using formulas (5), (8) and (6), respectively. For results previously obtained and since the most significant responses were recorded after 72 h, the experiment was carried out on this experimental condition. Data obtained are reported in Fig. 1.15. Statistical Analysis are reported in Annex III.

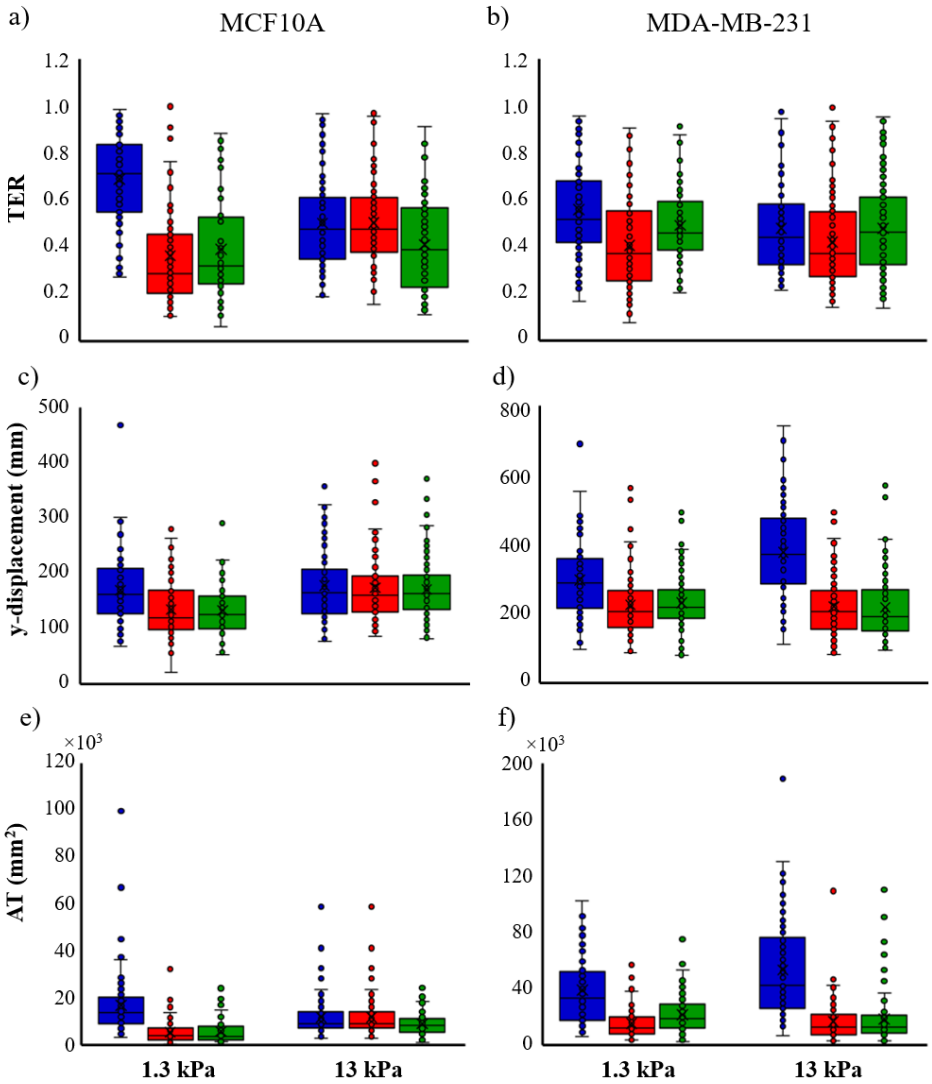

Figure 1.15 Box plots (mean, median, interquartile range, and outliers) of TER (a,b), y-displacement (c,d) and AT (e,f) parameters of MCF10A (a-e) and MDA-MB-231 cells (b-f) in control condition (blue) and 72 h after irradiation with doses of 2 Gy (red) and 10 Gy (green). n > 58 for MCF10A cells, n > 82 for MDA-MB-231 cells.

Under control conditions, TER of normal and tumor cell lines was strongly influenced by substrate stiffness. TER of MCF10A cells decreased by 27%, while that of MDA-MB-231 cells by 14% when

substrate stiffness increased. A comparison between the two cell lines shows that TER of MCF10A cells is 19% and 5% greater than that of tumor cells on soft and stiff substrate, respectively. This phenomenon indicates that the directionality of cell trajectories is greater on substrates similar to the tumor pathological environment.

Regarding the displacement along y′ and AT, MCF10A cells moved along y′ regardless of substrate stiffness, while their AT decreased by 28% on rigid substrate. In contrast, both displacement along y′ and AT of MDA-MB-231 showed a significant increase of 27 and 38% when grown on stiff rather than soft substrate.

After irradiation, MCF10A cells grown on soft substrate responded to irradiation by reducing all parameters very significantly and independently of the delivered dose: TER decreased by 47%, displacement along y′ by 21%, and AT by 68% at a dose of 2 Gy; while TER, displacement along y′, and AT decreased by 43%, 22 and 66%, respectively, in the case of a dose of 10 Gy.

On the stiff substrate, 2 Gy dose had no effect, while at 10 Gy cells decreased their migration parameters: TER, displacement along y′, and AT reduced by 15, 10 and 30%, respectively. MDA-MB-231 were found to be more radiosensitive, particularly on the rigid substrate. Only TER was more significantly reduced when cells adhered to soft substrate: it decreased by 27 and 12% after irradiation with doses of 2 and 10 Gy, respectively (with values similar to the control conditions). This reduction was also recorded for displacement along y′ (26 and 20% after irradiation with 2 and 10 Gy, respectively) and for AT (61 and 45% after irradiation with 2 and 10 Gy, respectively). On the rigid substrate, the TER was reduced only with the lowest dose (12% reduction), while displacement

along y′ decreased by 42 and 46%, and the AT by 69 and 66% after irradiation with 2 and 10 Gy, respectively.

Cell motility can be explained by evaluating not only adhesion in terms of spreading area, but also in terms of cell shaping. So, a deeper analysis of the influence of substrate stiffness and irradiation on cell morphology has been performed by introducing two parameters to describe cell shape: **SF** and **CI**. Parameters were calculated using formulas (10) and (9), respectively and results are shown in Fig. 1.16.

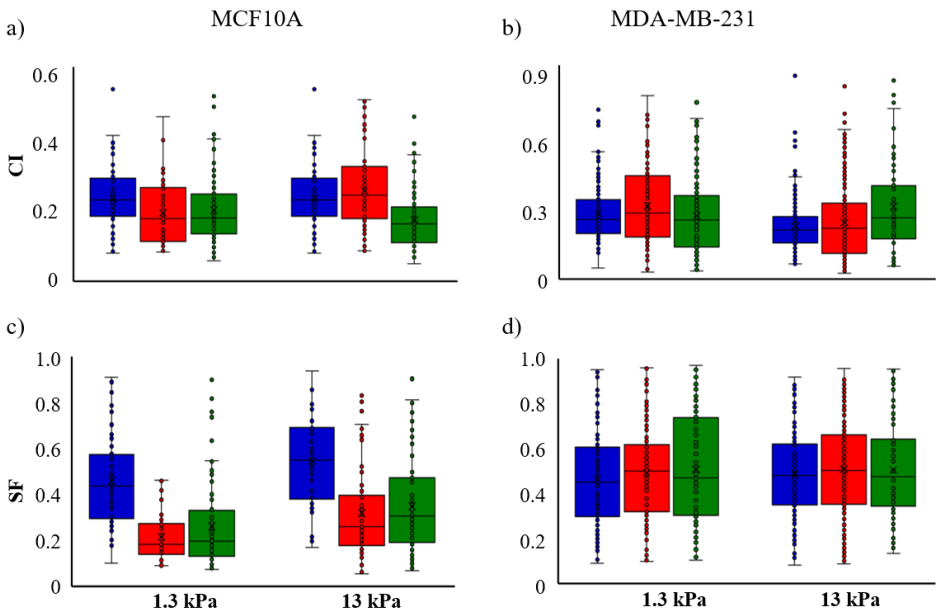

Figure 1.16 Box plots (mean, median, interquartile range, and outliers) of SF (a,b) and CI (c, d) of MCF10A (a, c) and MDA-MB-231 cells (b ,d) in control condition (blue) and 72 h after irradiation with doses of 2 Gy (red) and 10 Gy (green). n > 50 for MCF10A cells, n > 75 for MDA-MB-231 cells.

Under control conditions, MCF10A showed low SF values not dependent on substrate stiffness (0.23 and 0.22 on soft and hard substrates, respectively), while their CI increased by 19% in cells on stiff substrate, indicating a more flattened and round shape. In contrast, MDA-MB-231

showed significantly lower SF on stiff substrate (0.28 and 0.22 on 1.3 and 13 kPa substrates, respectively) and a CI close to that of MCF10A on soft substrate.

After irradiation, MCF10A on soft substrate reduced their SF by 18 and 14%, while on rigid substrate the SF increased by 16% at a dose of 2 Gy and decreased by 21% at a dose of 10 Gy.

This trend is different for CI: MCF10A cells reduced their CI by 53 and 43% on the soft substrate and by 42 and 36% on the hard substrate. The effects of X-rays on MDA-MB-231 were not significant, except in two cases: on soft substrate the SF of the cells irradiated with a dose of 2 Gy increased by 12%, while on the rigid substrate the SF of the cells irradiated with a dose of 10 Gy increased by 36%.

1.3.4. YAP expression

Below is a comparison between $Y_{N/C}^{d}$ which is the most used to study the effects of translocation processes from nucleus to cytoplasm and $Y_{N/C}$ to thoroughly investigate the effects of ionizing radiation on the YAP mechanotransduction process [71]. Data obtained are shown in Fig. 1.10 and reported in Fig. 1.14 – 1.18, and Tab. 1.7. Statistical Analysis are reported in Annex IV.

Cytoplasmic and nuclear YAP densities were calculated individually and reported in Annex V.

YAP concentration of both the nucleus and the cytoplasm was calculated measuring the integrated fluorescence with ImageJ software (Fig. 1.17). This ratio was calculated for both cell lines at 24 and 72 h after irradiation at 2 and 10 Gy doses, using formula (12). Fig. 1.18 and Tab. 1.9 show the results obtained.

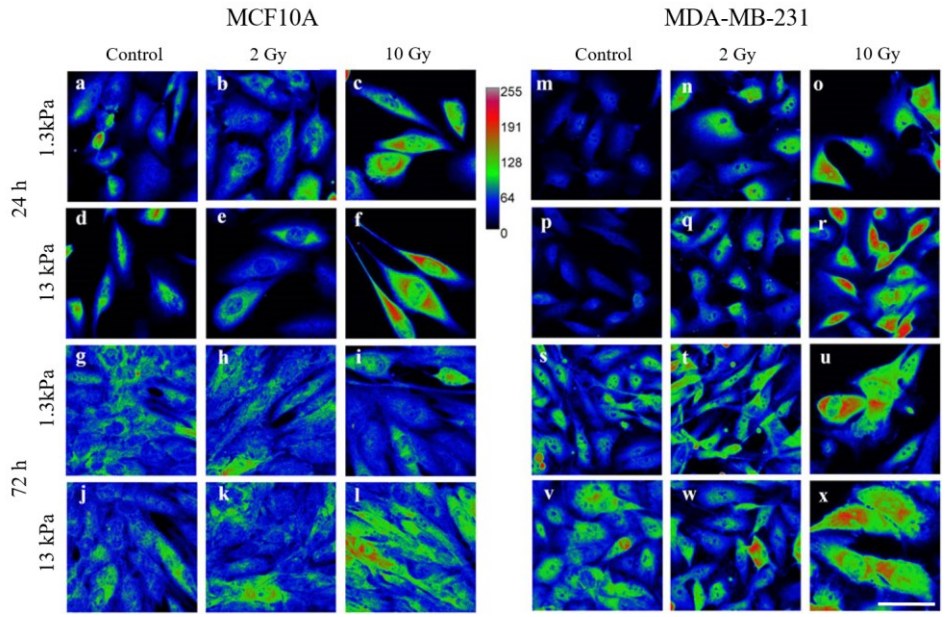

Figure 1.17 Panel of representative images of YAP immunofluorescence in MCF10A (a-l) and MDA-MB-231 (m-x), shown as rainbow RGB look-up table, in all experimental conditions. Colour bar: YAP intensity (A.U.). Scale bar: 50 μm.

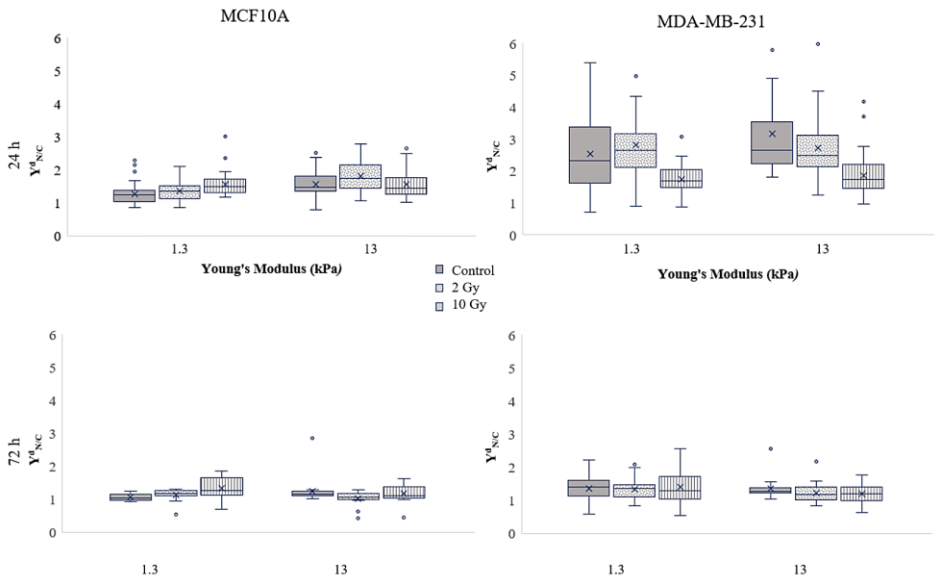

Figure 1.18 Box plots (mean value, the median, the interquartile, and the outliers) of the normalized YAP nucleus to cytoplasm ratio, $Y^{d}_{N/C}$. The values have been estimated for both cell lines 24 (top) and 72 h (bottom) after irradiation.

Table 1.9 Median values of $Y_{N/C}^{d}$ in all experimental conditions

Dose (Gy)	***Time after irradiation (h)***	***Young's Modulus (kPa)***	***Median MCF10A***	***Median MDA-MB-231***
control		1.3	1.240	2.331
		13	1.470	2.659
2	24	1.3	1.356	2.660
		13	1.733	2.496
10	24	1.3	1.500	1.669
		13	1.434	1.738
control		1.3	1.034	1.399
		13	1.166	1.263
2	72	1.3	1.184	1.351
		13	1.067	1.184
10	72	1.3	1.264	1.290
		13	1.107	1.207

Under control conditions, MCF10A was characterized by a YAP ratio close to 1 on both substrates, however there is a slight but significant increase in this ratio from 1.3 to 13 kPa of the Young's modulus of the substrates, a sign that the cells perceive the different mechanical properties of their microenvironment.

MDA-MB-231 showed a YAP ratio strongly above 1, indicating substantial accumulation of YAP in the nucleus. The ratio value was not significantly changed from 1.3 to 13 kPa Young's modulus. This phenomenon is justified by the fact that YAP is highly active in almost all tumor cells [72].

After 24 h from irradiation, a dose-dependent increase in the soft substrate ratio occurs in healthy cell line. On the stiffer substrate, YAP concentration showed higher values than the control condition after being irradiated with a 2 Gy dose, while the higher dose did not affect the YAP ratio.

In MDA-MB-231 cell line, YAP concentration decreased with dose in both conditions, supporting the idea of a radiation exposure repressive effect on the activation of YAP signalling. The values obtained from the analyses carried out 72 h after irradiation show that the MDA-MB-231 cells reduced the values of $Y_{N/C}^{d}$ under all conditions, exhibiting identical ratios on both substrates and in both controls and irradiations' conditions.

Despite being the most widely used information, the $Y_{N/C}^{d}$ has been demonstrated some limitations, because, unlike $Y_{N/C}$, does not provide details on the intensity of nuclear and cytoplasmic YAP expression. Fig.1.19 and Tab. 1.10 show the nuclear to cytoplasmic ratio of total YAP, calculated with formula (11).

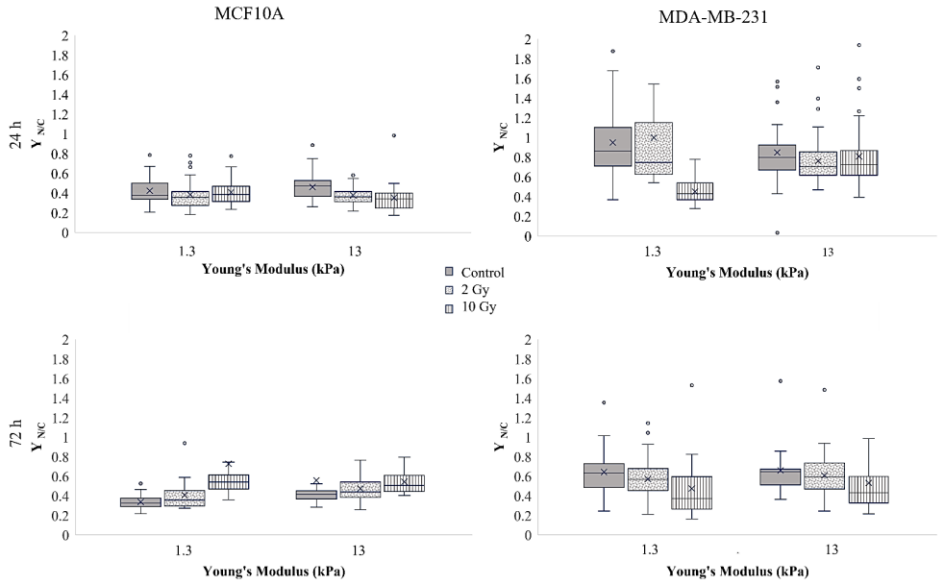

Figure 1.19 Box plots (mean value, the median, the interquartile, and the outliers) of the nuclear to cytoplasmic ratio of total YAP, $Y_{N/C}$. The values have been estimated for both cell lines 24 (top) and 72 h (bottom) after irradiation.

Table 1.10 Median values of $Y_{N/C}$ in all experimental conditions.

Dose (Gy)	***Time after irradiation (h)***	***Young's Modulus (kPa)***	***Median MCF10A***	***Median MDA-MB-231***
control		1.3	0.377	0.862
		13	0.472	0.798
2	24	1.3	0.357	0.747
		13	0.361	0.704
10	24	1.3	0.386	0.429
		13	0.340	0.717
control		1.3	0.324	0.633
		13	0.415	0.647
2	72	1.3	0.356	0.570
		13	0.441	0.593
10	72	1.3	0.541	0.372
		13	0.506	0.431

Under control conditions the trend is the same as that reported for $Y_{N/C}^{d}$. after irradiation MCF10A showed a substantial reduction of $Y_{N/C}$ on the rigid substrate after 24 h when irradiated with the highest dose, while at longer times this response was completely reversed with a dose-dependent increase of the same parameter on both substrates.

MDA-MB-231, unlike $Y_{N/C}^{d}$, after 24 h and on the rigid substrate, does not show more dose-dependent increases than YAP. Moreover, after 72 h there is instead a decrease in time- and dose-dependent on both substrates rigidities.

In the late response to irradiation, the YAP sequestration process in the nucleus of MCF10A or in the cytoplasm of MDA-MB-231 could be a mechanism by which cell growth or apoptosis is regulated. Dephosphorylation of YAP, which is associated with its transport in the nucleus, reduces the binding of p73 and the consequent cellular apoptosis downstream in breast cancer cells [72]. However, other research has

revealed that YAP phosphorylation in response to ionizing radiation could prevent YAP from functioning as a p73 co-activator to enhance proapoptotic genes, thus contributing to cell protection [73,75].

Changes in YAP localization are influenced by the different stiffness of the nucleus: rigid nuclei require contractile forces from the CSK promoting the displacement of YAP towards the nucleus. The nuclear stiffness is, in turn, regulated by the expression of the lamin A/C.

Therefore, the effect of radiation on lamin A/C was evaluated to understand whether changes in YAP localization after irradiation can be influenced by changes in lamin A/C expression. The images are quantified in terms of integrated fluorescence intensity with ImageJ software (Fig. 1.20). The results are shown in Fig. 1.21.

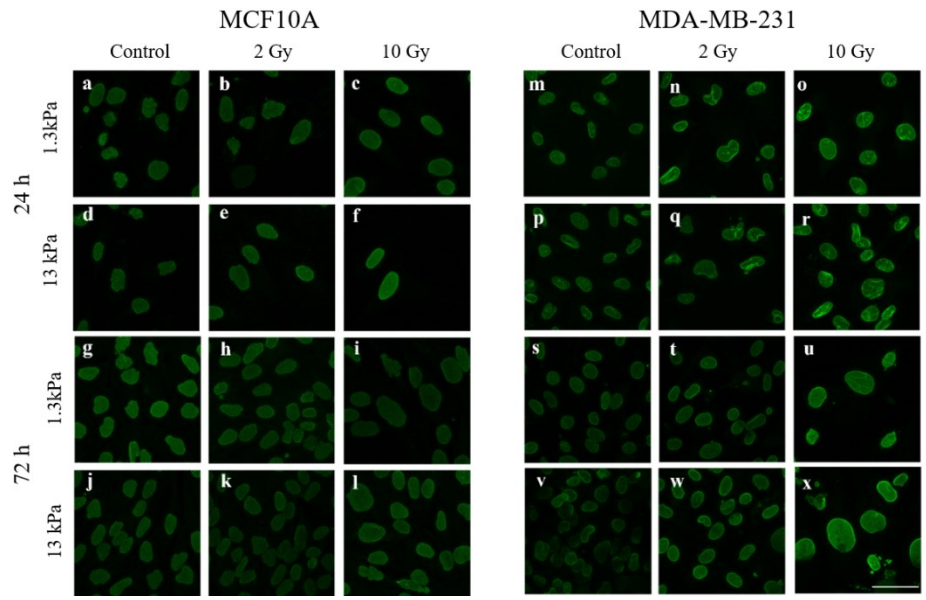

Figure 1.20 Panel of representative images of lamin A/C immunofluorescence in MCF10A (a-l) and MDA-MB-231 (m-w) in all experimental conditions. Scale bar, 50 µm.

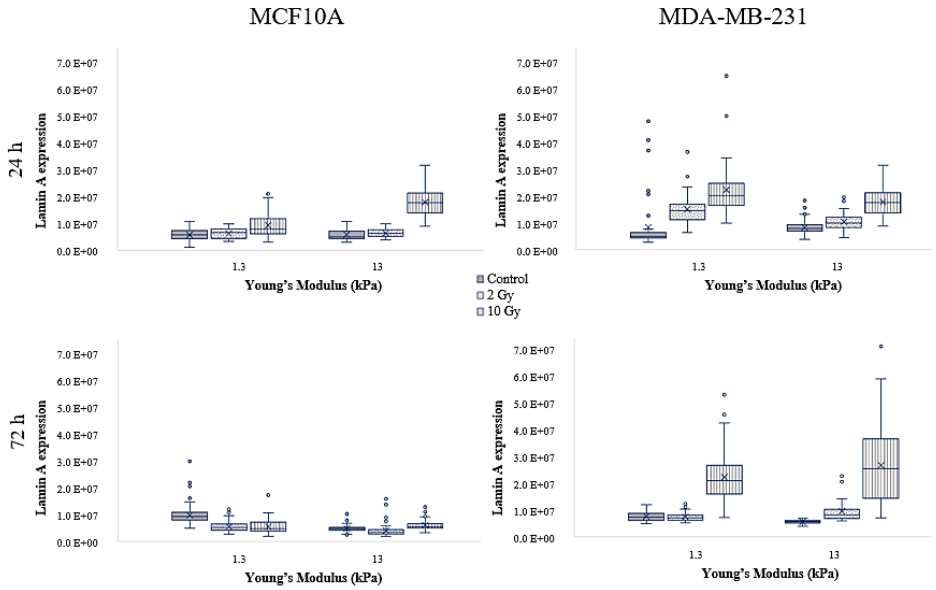

Figure 1.21 Box plots (mean value, the median, the interquartile, and the outliers) of the levels of lamin A/C expression. The values have been estimated for both cell lines 24 (top) and 72 h (bottom) after irradiation.

After 24 h from irradiation there was a dose-dependent increase in the expression of lamin A/C in both cell lines and on both stiffnesses. After 72 h, this response was completely reversed in healthy cells and accompanied by the nuclear translocation of YAP. In contrast, the higher levels of lamin A/C, together with the reduction of the nuclear localization of YAP, persisted in the tumor cells, when irradiated with the higher dose of 10 Gy. These results suggest that the variations in $Y_{N/C}$ expression could be attributed to the effects that irradiation can have on the levels of lamin A/C and, consequently, on nuclear deformability.

References

1. Gradishar WJ, et al. 2020. *J Natl Compr Canc Netw.* **18** (4):452-478. doi:10.6004 / jnccn.2020.0016
2. Waks AG. 2019. *JAMA*. **321** (3):288-300. doi:10.1001/ jama.2018.19323.
3. Iliakis G. 1991. *Bioessays*. **13** (12):641-8. doi:10.1002 / bi. 950131204
4. R Symonds, John Mills, Angela Duxbury Walter and Miller's Textbook of Radiotherapy: Radiation Physics, Therapy and Oncology. Elsevier 8th Edition - July 11, 2019
5. Durante M, et al. 2018. *Br J Radiol.* **91**(1082):20170628. doi:10.1259/bjr.20170628.
6. Minniti G, et al. 2012. *Handb Clin Neurol*. **104**:215-28. doi:10.1016/B978-0-444-52138-5.00016-5.
7. Whelan TJ, et al. 2010. *N Engl J Med*. **362**(6):513-20. doi:10.1056/NEJMoa0906260.
8. Withers HR. The four R's of radiotherapy. In: Lett JT, Adler H, editors. Advances in Radiation Biology, Vol. 5. New York: Academic Press; 1975.
9. Steel GG, et al. 1989. *Int J Radiat Biol*. **56**(6):1045-8. doi:10.1080/09553008914552491
10. Jansen KA, et al. 2015. *Biochim Biophys Acta*. **1853**(11 Pt B):3043-52. doi:10.1016/j.bbamcr.2015.05.007
11. Moore SW, et al. 2010. *Dev Cell.* **19**(2):194-206. doi:10.1016/j.devcel.2010.07.018.
12. del Rio A, et al. 2009. *Science*. **323**(5914):638-41. doi:10.1126/science.1162912.
13. Kobayashi T, at al. 2010. *Curr. Opin. Cell Biol.* **22**:669-676 doi:10.1016/j.ceb.2010.08.023.
14. van Helvert S, et al. 2018. *Nat Cell Biol*. **20**(1):8-20. doi:10.1038/s41556-017-0012-0.
15. Pastushenko I, et al. 2019. *Trends Cell Biol*. **29**(3):212-226. doi:10.1016/j.tcb.2018.12.001.
16. Yilmaz M, et al. 2009. *Cancer Metastasis Rev*. **28**(1-2):15-33. doi:10.1007/s10555-008-9169-0.
17. Panzetta V, et al. 2017. *Acta Biomater*. **57**:334-341. doi:10.1016/j.actbio.2017.05.002.
18. Stowers RS, et al. 2016. *Cell Mol Bioeng*. **10**(1):114-123. doi:10.1007/s12195-016-0468-1.
19. Panciera T, et al. 2020. *Nat. Mater*. **19**:797–806. doi:10.1038/s41563-020-0615-x.
20. Shibue T, et al. 2017. *Nat Rev Clin Oncol*. **14**(10):611-629. doi:10.1038/nrclinonc.2017.44.
21. Dongre A, et al. 2019. *Nat Rev Mol Cell Biol*. **20**(2):69-84. doi:10.1038/s41580-018-0080-4.

22. Ladoux B, et al. 2017. *Nat Rev Mol Cell Biol*. **18**(12):743-757. doi:10.1038/nrm.2017.98
23. Sun Z, et al. 2016. *J Cell Biol*. **215**(4):445-456. doi:10.1083/jcb.201609037.
24. Shapovalov G, et al. 2016. *Semin Immunopathol*. **38**(3):357-69. doi:10.1007/s00281-015-0525-1.
25. Low BC, et al. 2014. *FEBS Lett*. **588**(16):2663-70. doi:10.1016/j.febslet.2014.04.012.
26. Nematbakhsh Y, et al. In Y. Sun, D. Kim, & C. Simmons (Eds.), pp. 169-185. Cambridge University Press. 2015. doi:10.1017/CBO9781139939751.011
27. Sinclair WK, et al. 1987. *Radiat Res*. **112**(3):407–417. doi:10.2307/3577094.
28. Smith CA. 1987. *J Cell Sci Suppl*. **6**:225-41. doi:10.1242/jcs.1984.supplement_6.16.
29. Elkind MM. 1984. *Radiat Res*. **100**(3):425-49.
30. Woloschak GE, et al. 1990. *Cancer Res*. **50**(2):339-44.
31. Woloschak GE, et al. 1990. *Mol Carcinog*. **3**(6):374-8. doi:10.1002/mc.2940030609.
32. Woloschak GE, et al. 1991. *Int. J. Radiat. Biol*. **59**(5):1173-1183. doi:10.1080/09553009114551051.
33. La Verde G, et al. 2021. *Biomedicines.* **9**(9):1102. doi:10.3390/biomedicines9091102.
34. Jasińska-Konior K, et al. 2019. *Sci Rep.* **9**:7008. doi:10.1038/s41598-019-43453-7
35. Panzetta V, et al. Proceedings of the 2017 IEEE 5th Portuguese Meeting on Bioengineering (ENBENG), Coimbra, Portugal, 16–18 February 2017; pp. 1–4
36. Panzetta V, et al. 2017. *Cytoskeleton* (Hoboken). **74**(1):40-52. doi:10.1002/cm.21334.
37. Mohammadkarim A, et al. 2018. *J Mech Behav Biomed Mater*. **85**:188-193. doi:10.1016/j.jmbbm.2018.06.009.
38. Hohmann T, et al. 2017. *Int J Mol Sci*. **18**(9):2001. doi:10.3390/ijms18092001.
39. Du Y, et al. 2014. *Neural Regen Res*. **9**(11):1129-37. doi:10.4103/1673-5374.135315.
40. Savla U, et al. 1998. *Radiat Res*. **150**(2):195-203.
41. Huang Q, et al. 2020. *Exp Ther Med*. **20**(6):283. doi:10.3892/etm.2020.9413.
42. Lamers ML, et al. 2014. *Acta Odontol Scand*. **72**(5):386-91. doi:10.3109/00016357.2013.847488.
43. Zheng Q, et al. 2015. *Hum Exp Toxicol*. **34**(9):894-903. doi:10.1177/0960327114561664.
44. Stroka KM, et al. 2011. *Cell Mol Bioeng*. **4**(1):9-27. doi:10.1007/s12195-010-0142-y.
45. Lee SH, et al. 2014. *Radiat Res*. **181**(6):650-8. doi:10.1667/RR13543.1.

46. Nguemgo Kouam P, et al. 2019. *Radiat Oncol*. **14**(1):25. doi:10.1186/s13014-019-1230-3.
47. Cox EA, et al. 2001. *Mol Biol Cell*. **12**(2):265-77. doi:10.1091/mbc.12.2.265.
48. Rousseau M, et al. 2011. *Biochem Biophys Res Commun*. **414**(4):750-5. doi:10.1016/j.bbrc.2011.09.150.
49. Panzetta V, et al. 2019. *Radiat Prot Dosimetry*. **183**(1-2):116-120. doi:10.1093/rpd/ncy303.
50. Panzetta, et al. 2015. *J Mech. Med. Biol*. **15**:1540022 doi:10.1142/S0219519415400229.
51. Edwards JG, et al. 1971. *Nat New Biol*. **231**(22):147-8. doi:10.1038/newbio231147a0.
52. Panzetta V, et al. 2020 *Cancers* (Basel) **12**(5):1170. doi:10.3390/cancers12051170.
53. Fusco S, et al. 2015. *Acta Biomater*. **23**:63-71. doi:10.1016/j.actbio.2015.05.008.
54. Cordes N, et al. 2003. *Br J Cancer*. **89**(11):2122-32. doi:10.1038/sj.bjc.6601429.
55. Park CM, et al. 2006. *Cancer Res.* **66**(17):8511-9. doi:10.1158/0008-5472.CAN-05-4340.
56. Gogineni VR, et al. 2011. *Int J Oncol*. **38**(6):1615-24. doi:10.3892/ijo.2011.987.
57. Wild-Bode C, et al. 2001. *Cancer Res*. **61**(6):2744-50.
58. Song CH, et al. 2019. *Int J Radiat Biol.* **95**(11):1498-1506. doi:10.1080/09553002.2019.1642535.
59. Imaizumi H, et al. 2018. *Cancer Sci*. **109**(4):1158-1165. doi:10.1111/cas.13545.
60. Akervall J, et al. 2014. *Eur J Cancer.* **50**(3):570-81. doi:10.1016/j.ejca.2013.11.007.
61. Fernandez-L A, et al. 2012. *Oncogene.* **31**(15):1923-37. doi:10.1038/onc.2011.379.
62. Xu X, et al. 2019. *Cancer Manag Res.* **11**:7577-7585 doi:10.2147/CMAR.S210825
63. Soule HD, et al. 1990. *Cancer Res*. **50**(18):6075-86.
64. Qu Y, et al. 2015. *PLoS One*. **10**(7):e0131285. doi:10.1371/journal.pone.0131285.
65. Kenny PA, et al. 2007. *Mol Oncol.* **1**(1):84-96. doi:10.1016/j.molonc.2007.02.004.
66. Levental KR, et al. 2009. *Cell.* **139**(5):891-906. doi:10.1016/j.cell.2009.10.027
67. Damljanović V, et al. 2005. *Biotechniques*. **39**(6):847-51. doi:10.2144/000112026.
68. Manual available from: https://www.olympus-lifescience.com/data/olympusmicro/brochures/pdfs/ix71.pdf?rev=EABE (Accessed on June 2022).

69. Alam S, et al. 2014. *Prog Mol Biol Transl Sci*. **126**:205-15. doi:10.1016/B978-0-12-394624-9.00008-7.
70. Panzetta V, et al. 2020. *Front Phys.* **414**. doi:10.3389/fphy.2020.575906.
71. La Verde G, et al. 2022. *Front Bioeng Biotechnol*. **10**:969004. doi:10.3389/fbioe.2022.969004.
72. Zanconato F, et al. 2016. *Curr Opin Pharmacol*. **29**:26-33. doi:10.1016/j.coph.2016.05.002
73. Matallanas D, et al. 2007. *Mol Cell*. **27**(6):962-75. doi:10.1016/j.molcel.2007.08.008.
74. Strano S, et al. 2005. *Mol Cell.* **18**(4):447-59. doi:10.1016/j.molcel.2005.04.008.
75. Levy D, et al. 2008. *Mol Cell.* **29**(3):350-61. doi:10.1016/j.molcel.2007.12.022.

Chapter 2 – From chemotherapy to Nanomedicine: formulation and stability study of NPs Ha-coated

2.1 Background

Nanomedicine is increasingly becoming the best frontier of chemotherapy, as it uses NPs for drug delivery. These devices can be of different nature and have specific binding affinities for one or more drugs. With this method it is possible to overcome the adverse effects due to traditional systemic administration with the result of an improved targeted therapy. If on the one hand the use of NPs guarantees many beneficial effects for therapeutic purposes, on the other they present several challenges, first the determination of formulation stability. The management of this aspect, through a physicochemical characterization, allows the creation of a "predictable" final product, improving the drug performance to the optimum.

The aim of this part of the work was to synthesize, through the nanoprecipitation technique, two kinds of poly (lactic acid-co-glycol) (PLGA) NPs: NPs coated with hyaluronic acid (HA-PP-NPs) and NPs without hyaluronic acid (PP-NPs) used as a control for the first ones. To perform stability studies, two different techniques were used: Dynamic Light Scattering (DLS) traditionally used to measure NPs physico-chemical parameters and Surface Enhanced Raman Scattering (SERS) spectroscopy for the investigation on the surface variations of HA-PP-NPs over time. Merging the results obtained from these two measurements, it was possible to define the aging and storage time of the formulation within which it is still possible to guarantee the maintenance of the chemical-physical characteristics of the formulation.

2.1.1. Chemotherapy in Breast Cancer

Cancer treatment involves a multidisciplinary approach to global disease management. Surgery and radiotherapy are often the primary therapeutic choice for the treatment of malignant cancer.

However, when the tumor develops metastatic disease, there will potentially be multiple sites for the tumor cells to migrate and proliferate. In this case chemotherapy is helpful, because it relies on specific drugs which, spreading throughout the body, can cause cell death in the metastasis.

The choice of the therapeutic plan is influenced by the nature and stage of the tumor, as well as by the patient characteristics, for this reason it is always desirable to provide "tailored" therapies to increase their efficacy.

Regarding the timing of administration, there are different scenarios [1]:

- Before surgery: chemotherapy is adopted to reduce a tumor that is too large and facilitate its removal, or when the tumor is too firmly attached to the surrounding healthy tissue and cannot be removed by surgery alone. In this situation, chemotherapy can be given even before radiotherapy and it is defined as neo-adjuvant therapy
- After surgery: the entire tumor mass visible has been removed, but there is a risk that some tumor cells, remaining in circulation and not otherwise detectable by diagnostic tools, could generate a relapse. In such cases, chemotherapy causes the death of these possible cells' residuals, thus reducing the risk of disease recurrence. This is defined as adjuvant therapy.
- During radiotherapy: sometimes chemotherapy is applied simultaneously with radiotherapy, as chemoradiotherapy.

- In the presence of advanced disease, for which local treatments are not possible: chemotherapy does not aim to cure the disease, but is used to reduce its volume, slow down its growth and control symptoms. When used for these purposes, the duration of chemotherapy is not defined, but is decided based on the disease response and the side effects of the treatment. Furthermore, chemotherapy can be repeated, with other drugs, if the disease starts to grow again after a certain period of response (first, second, …, n. lines of chemotherapy).
- High-dose chemotherapy and subsequent bone marrow transplant: for some types of cancer, chemotherapy is given in very high doses. Normally, high dosages destroy the bone marrow that produces blood cells. For this reason, at the end of the treatment it is necessary to reintegrate the bone marrow with the transplantation of stem cells taken from the same patient before the treatment or from a compatible donor.

Conventional chemotherapy is a treatment that involves the use of toxic drugs to destroy cancer cells, however, undesirable outcomes are due to the single therapeutic modality, which fails to overcome the physiological complexity of tumors [2].

To address this problem, the combination of drugs capable of acting synergistically or independently on different signalling pathways in cancer cells and reducing each dose of drug to reduce side effects is now widespread [3].

Breast cancer therapy involves a combination of neoadjuvant chemotherapy, operable tumor surgery, radiotherapy, and adjuvant chemotherapy and/or endocrine therapy [4, 5]

Neoadjuvant chemotherapy is widely used in early stage and locally advanced breast cancer to reduce disease and promote surgical removal by lumpectomy followed by full breast irradiation or mastectomy [6-8].

Adjuvant therapy is a systemic therapy with cytotoxic agents, targeted molecular agents used individually or in combination, also after local irradiation treatments [9].

In metastatic breast cancer, surgical excision is considered palliative [10] therefore systemic chemotherapy appears to be the main treatment strategy [11]. This therapeutic approach faces a major obstacle: there is no effective first-line chemotherapy protocol for the treatment of metastases, therefore metastatic breast cancer is considered largely untreatable or with little hope of resolution.

Another important phenomenon that leads to a reduction in the therapeutic efficacy of drugs and therefore to the failure of cancer treatment is multi-drug resistance (MDR). It is associated with various factors such as the interaction with the drug itself, genetic factors (gene mutations, amplifications, and epigenetic alterations), growth factors, greater DNA repair capacity and high metabolism of xenobiotics [12-16].

For these aspects and for the complexity of the disease it becomes important to identify the mechanisms involved in multidrug resistance, and to promote the development of new cancer therapies.

Breast cancer is a heterogeneous disease and requires specific therapeutic interventions, based on the biological characteristics of the cell subtype involved which will have its own distinctive prognosis and chemotherapy sensitivity [17].

Thanks to the new discoveries of cancer characterization, scientific interest is increasingly focused on the study of targeted therapies: a "tailored" approach based on the relationship between the drug used and its effect on the molecular alteration that confers MDR to cancer cells or in any case their survival to treatment [18].

Breast cancer subtyping into HR^+, $HER\text{-}2^+$, $HER\text{-}2^-$ and TNBC is the basis for treatment choice.

For both $HER\text{-}2^+$ and $HER\text{-}2^-$ tumors, adding cyclin CD4/6 inhibitors to hormone therapy demonstrated a doubling of progression-free survival compared to hormone therapy alone.

In $HER\text{-}2^+$ tumors, docetaxel-associated double blockade anti-HER-2 (trastuzumab and pertuzumab) in the first line reported superior progression-free survival and overall survival, compared to trastuzumab and docetaxel [19].

TNBC leads to a higher rate of recurrence metastases and strong resistance to chemotherapy and radiotherapy, however chemotherapy is the gold standard. More recently, immunotherapy (atezolizumab) added to first-line chemotherapy (nabpaclitaxel) has been shown to increase not only progression-free survival but also overall survival compared to chemotherapy alone [20].

2.1.2 Nanomedicine for drug delivery

The failure of chemotherapy administration due to various factors such as inefficient access of drugs to metastatic sites, physico-chemical interactions unfavorable to drug release, and MDR, has stimulated the development of nanomedicine. This science, over the past 15 years, has produced promising results in drug administration, diagnosis, imaging, and therapy practices [21, 22]. The strategy adopted involves the use of

structures of various kinds with diameters between few unit's nm and a few hundred nm defined as NPs [23]. NPs improve therapeutic index of drug compared to conventional therapy as they improve pharmacokinetics, stability, solubility, half-life, and accumulation in the target sites. Fig. 2.1 shows how the NPs chemical-physical characteristics affect the responses of biological processes.

NPs can be designed to obtain highly specific multifunctional devices for the target tissue/organ and thus respond to the needs of drug delivery. NPs have proved to be particularly appropriate for drug delivery to malignant cells as solid tumor tissues are characterized by some peculiarities that make them suitable for the selective delivery of drugs.

Solid tumors often have irregular vascularity when compared to healthy tissues. In the inner lining of the vessels the endothelial cells are not joined by junctions to form the normal monolayer structure, consequently their barrier function is compromised [24]. The openings between the endothelial cells of the tumor vessels can have diameters greater than 200 nm, consequently the entry of small substances and molecules, including NPs, is possible [25]. The NPs size plays a fundamental role, if the NPs are large enough to be recognized by the immune system they can be easily captured by phagocytic cells, on the other hand, if they are too small, they can instead be eliminated by the renal system. In both cases they will not reach their target [26]. NPs with dimensions below 200 nm are poorly captured by the mononuclear phagocytic system, remaining in circulation for longer [27]. Therefore, by optimizing the size of the carriers it is possible to promote the penetration into the tumor tissues and increase the circulation time.

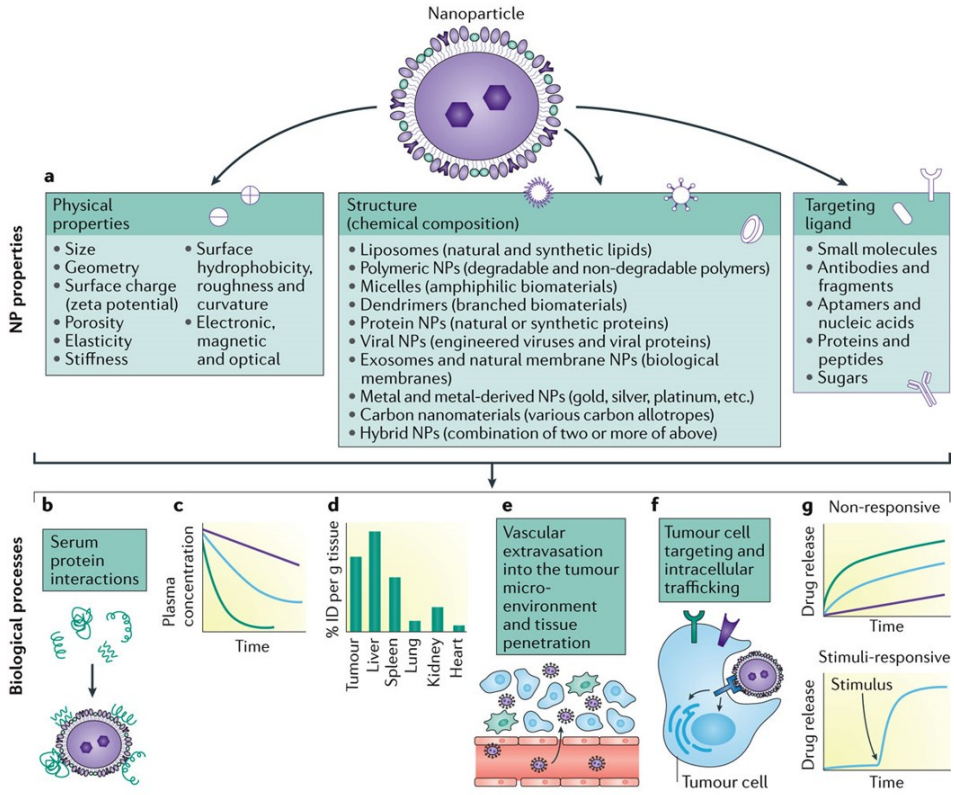

Figure 2.1. a) NPs can be of different materials and have various physicochemical properties (e.g., size, geometry, surface characteristics, elasticity, and stiffness, among others) or they can be modified with different targeted ligands. These properties interact in different ways with biological processes such as b) interactions with serum proteins, c) blood circulation, d) biodistribution, ID stands for Injected Dose, e) extravasation into the perivascular tumor microenvironment and penetration into the internal tumor tissue, f) targeting of tumor cells and intracellular trafficking, g) controlled drug release. Adapted from [21].

The materials used to produce NPs must have some peculiar characteristics, such as biocompatibility (low toxicity), good pharmacokinetics and reproducible synthesis. For this reason, there are NPs of different nature and types, some of them are listed below:

– Liposomes are spherical vesicles consisting of a double layer of phospholipids [28]. These vectors can be coupled either with

hydrophilic drugs, which will be encapsulated within the aqueous core of the liposome, or with hydrophobic drugs, which can dissolve between the lipid bilayers. However, their loading capability is limited, especially for hydrophobic drugs, which makes them primarily considered hydrophilic drug carriers. Liposomes tend to accumulate on the outside of tumors due to the EPR effect, making these NPs perfect for targeting tumor tissue [29].

- Carbon nanotubes are tubular networks of carbon atoms with a diameter of a few nm, completely insoluble in all solvents, which create toxicity problems. However, limiting their length to ~ 100 nm, their diameter to ~ 4 nm and chemically modifying their surface properties decreases this toxicity. These vectors can be loaded with different drugs both in their internal cavity and on their surface, making them able to cross the plasma membrane and enter tumor cells by endocytosis [30].
- Cubosomes are highly stable NPs formed by a single lipid bilayer. This has a periodic membrane reticular structure with pores that can be loaded with drugs. The composition of the cubosome can be highly tuned, making them applicable in various fields [31]. Gold NPs are in an early stage of clinical testing. These supports can be produced by optimizing their shape and size, also modifying their surface with different functional compounds. They showed good biocompatibility and controllable biodistribution patterns [32].
- Polymer-based NPs are polymeric aggregates prepared from natural or synthetic polymers using different strategies. They are characterized by a high in vivo stability, a higher loading efficiency

compared to liposomal carriers and, in addition, a controlled drug release kinetics. The most used polymers are poly (lactic acid) (PLA), poly (glycolic acid) (PGA) and their copolymer, PLGA, for their biodegradability and biocompatibility.

In this scenario, the NPs formulation that can optimize drug delivery plays an increasingly important role. Likewise, it is important that the formulation is stable to guarantee the safety and efficacy of the pharmaceutical compounds.

The critical points include all steps of the process: from synthesis, to transport, to storage. Although both physical and chemical alteration processes are known [33], ensuring the stability of a formulation remains a complex problem that is not easy to manage.

The purpose of this phase of the study was to characterize the stability of the formulations to guarantee the quality of the physico-chemical characteristics over time.

Among the different physico-chemical parameters, the attention of this work was focused on three specific ones:

1. Mean diameter: NP diameter size influences absorption efficiency and kinetics, internalization mechanism and also subcellular distribution [34]. The cytotoxic effect is not negligible: larger and negatively charged NPs are less toxic than those of smaller size [35].
2. The Polydispersity Index (PDI): it is a dimensionless measure of heterogeneity of a sample based on its size.
3. The Zeta Potential (ζ) is another important parameter that indicates the charge between a solid surface and its liquid medium and is

usually used to evaluate the degree of repulsion between particles and therefore the stability of the system itself.

2.2 Materials and methods

The choice of the NPs type was based on the rationale that breast cancer has peculiar characteristics useful for designing a targeted therapy. In this case the overexpression of the membrane receptor cluster determinant 44 (CD-44) and its high and specific affinity for hyaluronic acid (HA) was considered. So, nanoparticles coated with hyaluronic acid were produced and measured to monitor their stability over time and possible surface alterations in order to establish the optimal time of the formulation.

2.2.1 Formulation of NPs

NPs formulations have been prepared adopting nanoprecipitation technique [36]. Poly(lactic-co-glycolic acid)-Rhodamine B (PLGA-RhoB), lactide:glycolide 50:50, (Aldrich, St. Louis, MO, USA) has been linked to poloxamers (PEOa-PPOb-PEOa), amphiphilic triblock copolymers characterized by a variable number of ethylene oxide (a) and propylene oxide (b) units. In particular, poloxamer F127 (a = 100 and b = 65) and F68 (a = 76 and b = 29) were used (Lutrol Basf, Ludwigshafen, Germany). Poloxamers are necessary for the binding between PLGA which is hydrophilic, and HA which is hydrophobic. For NPs coating, HA of 830 kDa (Altergon S.r.l., Italy) was used as it has demonstrated to be the optimal molecular weight for internalization studies [37]. NPs coated with HA (HA-PP-NPs) and nanoparticles without HA (PP-NPs) used as a control for the first ones have been formulated.

Fig. 2.2 shows chemical structures of each component.

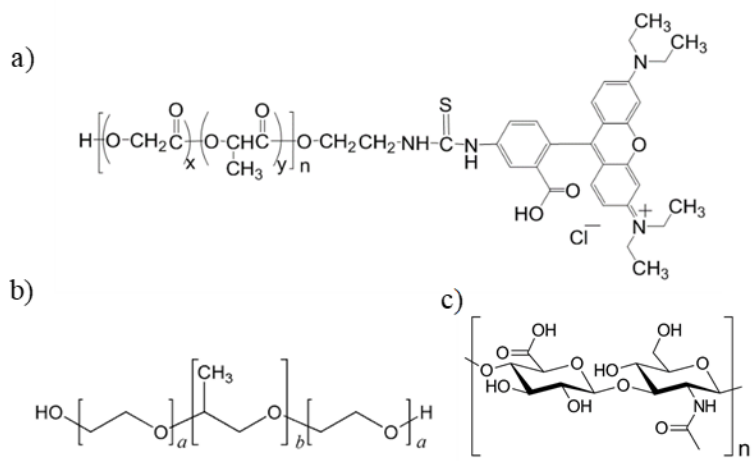

Figure 2.2 Chemical structures of a) PLGA-RhoB, b) generic poloxamer, and c) HA.

Processes of formulation is schematized in Fig 2.3. For both formulations an organic phase (O) with the same composition was prepared: 37.5 mg PLGA-RhoB, 18.75 mg F68, 18.75 mg F127 (mass ratio 1: 0.5: 0.5) in 5 mL of acetone. Subsequently a volume of 640 µl of ethanol (internal aqueous phase, W0) was added and it was emulsified using a 419 microtip probe (3000 sonicator, Misonix, USA; 5 min, 4W). The emulsion was combined with an aqueous phase (W1) placed under magnetic stirring, through a dripping obtained by forcing the emulsion through the needle of a syringe with an internal diameter: 11.99 mm and a volumetric flow rate of 333.3 µl / min (syringe pump). However, W1 is different for the two formulations. For PP-formulation, W1 is composed of 1.5mL of F68 in 0.5% w /v solution, 1.5 mL of F127 in 0.5% w/v solution and 37 mL of double-distilled water. For HA-PP-NPs formulation, 1.5mL of F68 in 0.5% w/v solution, 1.5 mL of F127 in 0.5% w/v solution, 12 mL of HA 830 kDa in 25 mL of double-distilled water were used.

Once all emulsion volume (W0 + O) has been transferred to the W1, the solution continues the magnetic stirring for about 4 h so that the acetone evaporates completely. The resulting NPs suspension was divided into 2 mL tubes and centrifuged three times (Hettich Zentrifugen, Germany; 10000 rpm, 10 min). After the first two centrifuges, 1 mL of supernatant was discarded and replaced with an equal volume of double-distilled water. After the last centrifuge, 1.5 mL of supernatant was removed, and 0.5 mL of PBS 1× was added. The formulation obtained was filtered with 0.2 µm filters and stored at 4 °C.

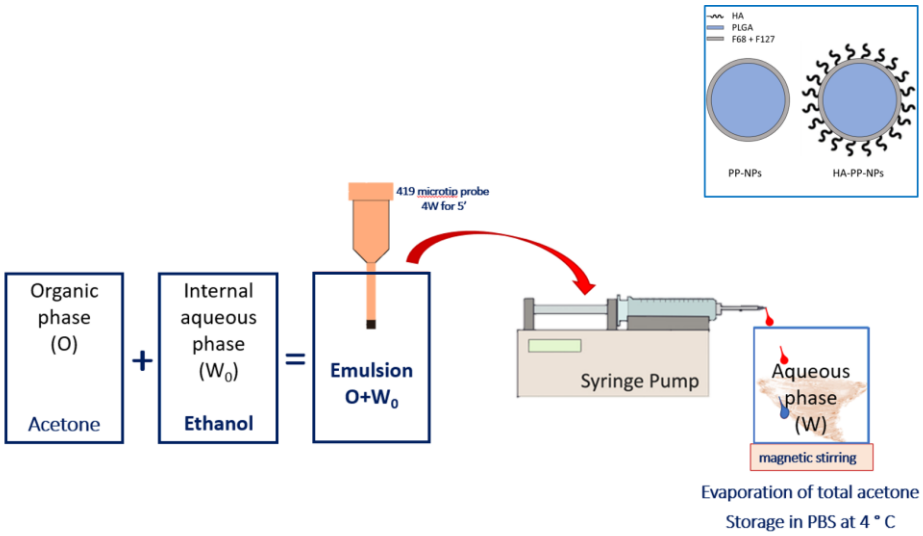

Figure 2.3 Schematization of a) NPs formulation process with the nanoprecipitation technique and b) possible NPs formulations.

2.2.2 Dynamic Light Scattering

Dynamic Light Scattering (DLS) is the most used technique to analyse particles and objects in the nanoscale. The DLS technique is based on scattering due to a laser beam that strikes a colloidal suspension, in which the particle size is sub-micrometric (the detectability of the instrument is between 0.6 nm to 6 μm). DLS assumes that each particle subject to the random Brownian motion, hit by the laser light, produces the scattering phenomenon. The speed at which particles move is related to their size, so particles that have a fast motion will be smaller than others that move slower. The intensity of the scattered light has a fluctuation frequency dependent on the speed of diffusion of the particles which in turn depends on their size: therefore, the size of the particles can be extrapolated from the analysis of the fluctuations in the intensity of the scattered light using the Stokes-Einstein equation:

$$D = \frac{k_B T}{6\pi\eta R_H} \tag{15}$$

where: D is the translational diffusion coefficient [m^2/s], the "speed of the particles"; kB is the Boltzmann constant [m^2kg/Ks^2]; T is the absolute temperature [K]; η is the viscosity coefficient of the solvent [Pa · s]; RH is the hydrodynamic radius [m].

A basic schematization of the DLS is shown in Fig. 2.4: a monochromatic laser is shot through a polarizer and into the sample. The light hits particles and is scattered in all directions, then it goes through a second polarizer and is collected by a photomultiplier. The laser light emitted by the source is attenuated by a lens to reduce the intensity of the laser and avoid overloading the detector. If the laser beam is not attenuated, a large amount of light would be scattered and would stimulate

the detector generating determination errors. Furthermore, to reduce the possible multiple scattering due to the characteristics of the sample (e.g., high concentration of particles) the detector is positioned at an angle of 175 ° C with respect to the direction of the incident beam.

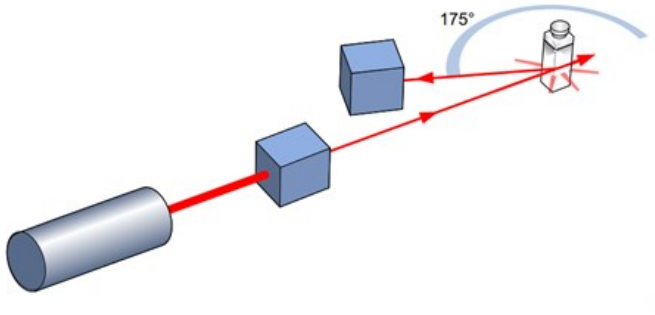

Figure 2.4 Schematization of DLS apparatus Adapted from [38].

The measurement allows to obtain a statistical distribution of the dimensions, using real distributions, based on the scattering intensity. The information obtained are a granulometric distribution curve, an average diameter value, and the polydispersity index (PDI) of the suspension. This index is between 0 and 1, the closer it is to 0 the more the suspension is monodisperse, on the other hand, for indices equal to 1 the suspensions are considered totally polydisperse. In general, a suspension can be considered monodisperse for values of PDI ≤ 0.2, on average polydisperse for 0.2 ≤ PDI ≤ 0.5 and polydisperse for values greater than 0.6 [39].

In addition to the size and PDI, another relevant information is the Zeta Potential. In this case the electrophoretic mobility is measured: a classic microelectrophoresis system is a cell with electrodes at both ends to which a potential is applied.

Particles in a liquid often have a surface charge. If an electric field is applied, these will move towards the negative or positive pole. The direction of the movement will be a clear indication of the charge on

suspended particles. If the particle has a surface charge, there will be an increase in the concentration of counter-ions around the surface.

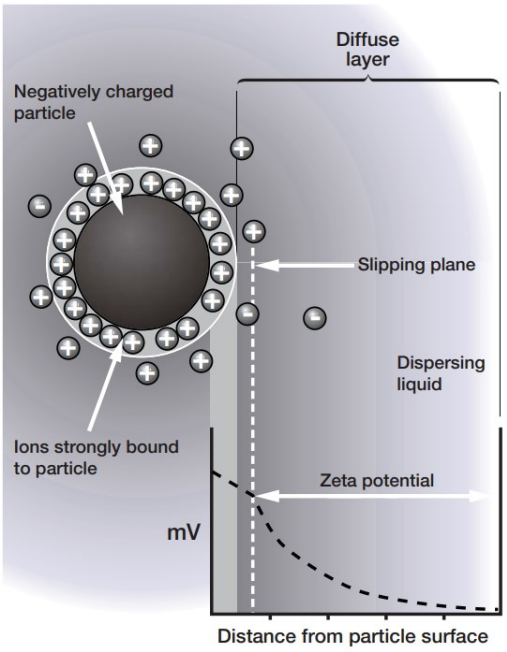

Figure 2.5 Representation of surface charges of a suspended particle. Adapted from [38].

The liquid layer surrounding the particle divides into two zones: the innermost one, called the Stern layer, where the ions are strongly bound, and an external portion, called the diffuse layer, where the interactions are weaker. The Stern layer and the diffuse layer constitute the electric double layer, inside which there is a boundary within which ions move with the particle, while outside the ions do not follow the motion of the particle. The potential relative to this boundary is the Zeta Potential (ζ), a parameter referred to the surface charge density, or to the phenomena of attraction or repulsion in solution, and therefore to the stability of the aggregates (Fig. 2.5).

If ζ value is high, the electrostatic repulsion prevents the aggregation of the dispersed particles; while when it is low the attractive forces prevail and the species give rise to coagulation phenomena. Negative values rangin between -20 and -40 mV indicate particles that are unlikely to aggregate, stable, non-toxic and which have a high penetration capacity.

Positive ζ values indicate particles usually toxic and potentially fusogenic with cells [40, 41].

Measurements were performed with a Zetasizer Nano (Malvern Instruments, Malvern, UK). The sample was prepared by diluting 10 µl of formulation in 1mL of double distilled water and inserted in a DTS0012 series polystyrene cuvette for dimensional and PDI analyses; while a DTS1070 series cuvette was used for ζ analysis (Fig. 2.6).

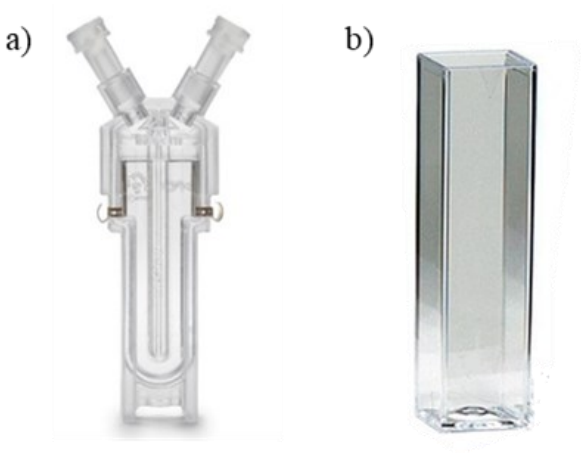

Figure 2.6 a) cuvette DTS0012 series, b) cuvette DTS1070 series

The samples were prepared, transported and measured at a temperature around 4 ° C so as not to alter the HA structure.

2.2.3 Raman spectroscopy and Surface Enhanced Raman Scattering

Raman spectroscopy (RS) is based on a phenomenon of matter-electromagnetic radiation interaction, defined as inelastic scattering of light. When the incident wave interacts with matter, the charges that make up the object begin to oscillate and emit electromagnetic radiation, according to the classical theory of electromagnetism. The RS detects the energy differences between the incident radiation and the scattered radiation from the sample, which varies from ultraviolet to near infrared.

Vibrational spectra can be considered as typical and characteristic patterns ("fingerprints") of the analytes and allow them to be detected qualitatively and quantitatively [42].

RS is a non-destructive, non-invasive technique that requires a small sample volume (approximately 1μm3); a laser radiation that hits a sample can be diffused with the same frequency (Rayleigh diffusion), greater or lesser (Raman diffusion) than the incident one.

“Raman effect" provides that the radiation is diffused (Fig. 2.7):

- in a small part in an elastic way in all directions without loss of energy, that is, at the same frequency as the incident radiation (elastic diffusion or Rayleigh);
- in part even smaller in anelastic way by yielding (Raman Stokes diffusion) or acquiring (Raman anti-Stokes diffusion) energy in the interaction with the molecule, thus vibrating at frequencies that differ in vibrational energy quanta.

The intensity of the scattered radiation (lower than the intensity of the incident radiation) therefore depends on the contribution given both by the elastic scattering and by the inelastic scattering and these, at in turn, they depend on the chemical structure of the molecules responsible for diffusion.

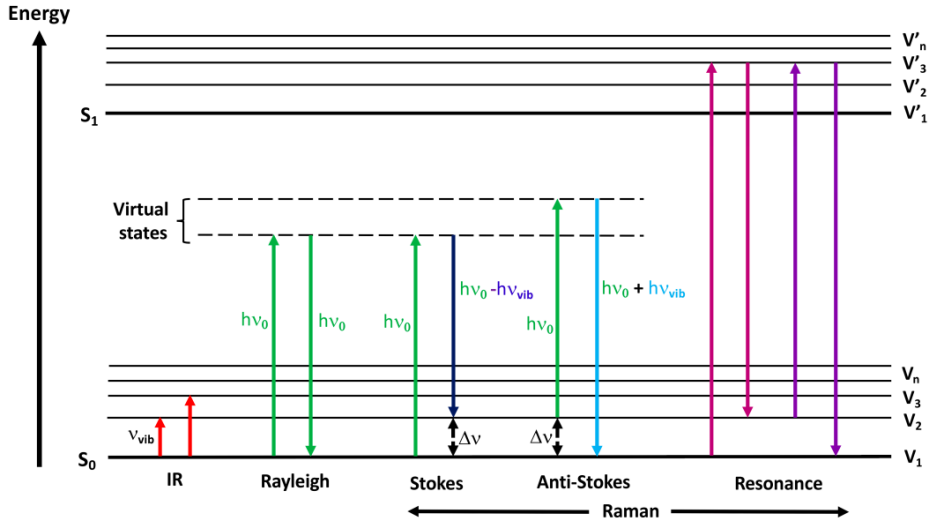

Figure 2.7 Jablonski energy diagram showing the transitions involved during infrared absorption, Rayleigh, Raman Stokes, anti-Stokes and Resonance Raman scattering. vibrational states (V'n) of the excited electronic state (S1). Hv0 = incident laser energy, hvvib = vibrational energy, Δv = Raman shift and vvib = vibrational frequencies. Adapted from [43].

Being an inelastic scattering process, its cross section is particularly low compared to other spectroscopic techniques such as, for example, fluorescence spectroscopy or absorption spectroscopy (IR).

Surface Enhanced Raman Scattering (SERS) spectroscopy is a variant of spontaneous Raman spectroscopy that overcomes the limit due to low cross sections and allows to increase sensitivity by several orders of magnitude (signal up to 10^{11}, single molecule sensivity).

This improvement, achieved by using a plethora of different nanostructured surfaces, instrumental setups and physical states of the samples, has widely spread the use of the SERS technique in various fields, from chemical physics to analytical chemistry, to electrochemistry, to solid state physics, biophysics and medicine [44].

Through the study of the acronym SERS, this spectroscopy technique can be characterized:

- Surface (S): SERS is a surface spectroscopic technique, for which the analyte must be at a nanometric distance from the substrate;
- Enhanced (E): the plasmonic resonances generated by the metal surface amplify the electromagnetic field;
- Raman Scattering (RS): the technique consists in the measurement of Raman signals.

The high SERS sensitivity is due to the excitation of surface plasmonic resonances located in metal nanostructures (mainly silver and gold), which provide an enormous enhancement of the electromagnetic field perceived by the molecules located near the so-called "hot spots" (Fig. 2.8).

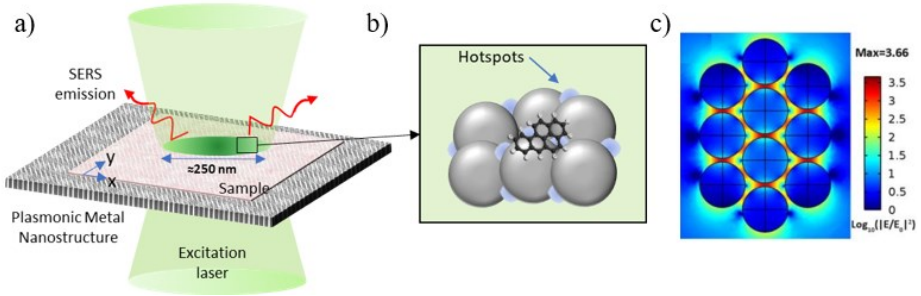

Figure 2.8 a) Schematic representation of the SERS emission, b) detail of the surface of the plasmonic metal nanostructure; c) intensity of the electric field that highlights the hot spots between the NPs. Adapted from [45].

Nanoporous materials are characterized by a dense network of interconnected structures with open nanopores that give rise to a large specific surface. The advantages of nanoporous SERS substrates relate to the large internal surface available for anchoring the molecules, and the high density of hot-spots formed in the nanopore, which ensures adequate improvement for analyte detection.

In this study, large size Ag-based nanoporous SERS substrates were used. In particular, starting from a relative flat Ag film deposited by magnetron-sputtering on a coverslip, a significant surface roughening is obtained by means of an inductively coupled plasma treatment (ICP), using synthetic air as the feed gas. This procedure gives rise to a coral-like nanopattern, composed mainly of AgO [46].

Measurements were performed using a UV-Vis spectrometer (Perkin Elmer, Lambda 35) equipped with an integrating sphere for spectral analysis in the 200-1000 nm region and a Raman spectrometer (Witec, alpha 300), an inverted microscope where the Nd: YAG laser beam (λ = 532nm) is sent.

The sample was prepared by diluting 10 µl of formulation in 1 mL of double distilled water and then taking a drop which was deposited on the substrate and allowed to dry at room temperature.

2.2.4 Statistical analysis

In order to highlight differences between different spectra, the Principal Component Analysis (PCA) technique was used. PCA is a well known multivariate statistical tool suitable to analyse multidimensional data sets. Its basic principle consists in an orthogonal linear transformation mapping of the initial data set (SERS spectra in this case) into a new coordinate system such that the greatest variance of the projected data comes to lie on the new coordinates (the first coordinate is called first principal component (PC1), the second greatest variance PC2, and so on). Therefore, PCA allows to condense, in the PCs space, acquired spectra in a set of points having as coordinates the respective PCi, i=1, 2, …, n. The affinity between spectra referring to different samples appears from the degree of clustering of the points in the PCs space. In our experiment, SERS spectra

were pre-treated by using a custom-made routine developed in order to eliminate spurious cosmic rays' contributions and to subtract a fourth order polynomial background contribution.

2.3 Results and discussion

This paragraph shows the results of the stability measurements of both formulations (PP-NPs and HA-PP-NPs) performed with both DLS and SERS techniques in order to understand the possibility of making these two techniques comparable and/or complementary.

The experimental activity was carried out thanks to a collaboration with various departments of the University of Naples Federico II: the laboratories of the Pharmaceutical Company, Technological Section of the Pharmacy department (for the formulation of NPs), the Interdepartmental Research Center on Biomaterials and the Department of Chemistry, Materials and Production Engineering (for DLS dimensional analyses) and the Department of Physics "E.Pancini" (for the SERS analyses).

2.3.1 DLS measurements

During the experiment period, two formulations were prepared each comprising HA-PP-NPs and PP-NPs (the latter used as a control). The average values of 5 measurements on each sample for each type of formulation collected over time were reported. The number of formulations was necessary also to have a statistic on the reproducibility of the formulation protocol. Figure 2.9 shows typical spectra of measurements:

a)

		Size (d.nm):	% Intensity:	St Dev (d.nm):
Z-Average (d.nm): 131.8	Peak 1:	142.3	100.0	39.99
PdI: 0.068	Peak 2:	0.000	0.0	0.000
Intercept: 0.926	Peak 3:	0.000	0.0	0.000
Result quality : Good				

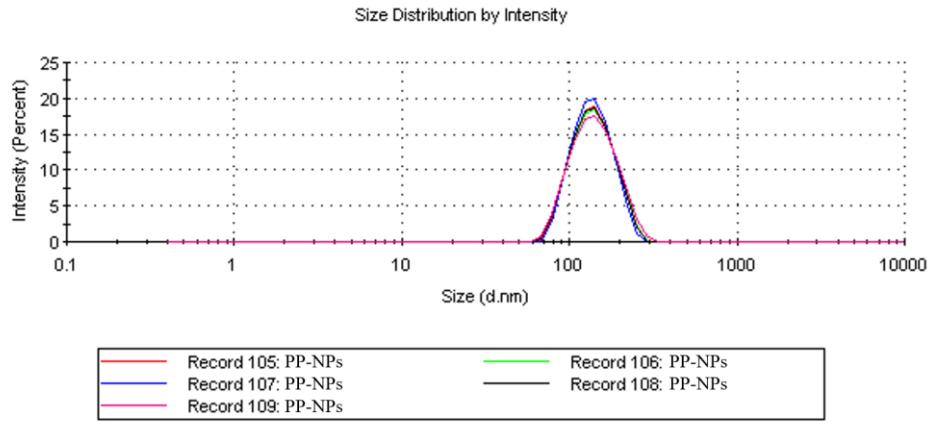

b)

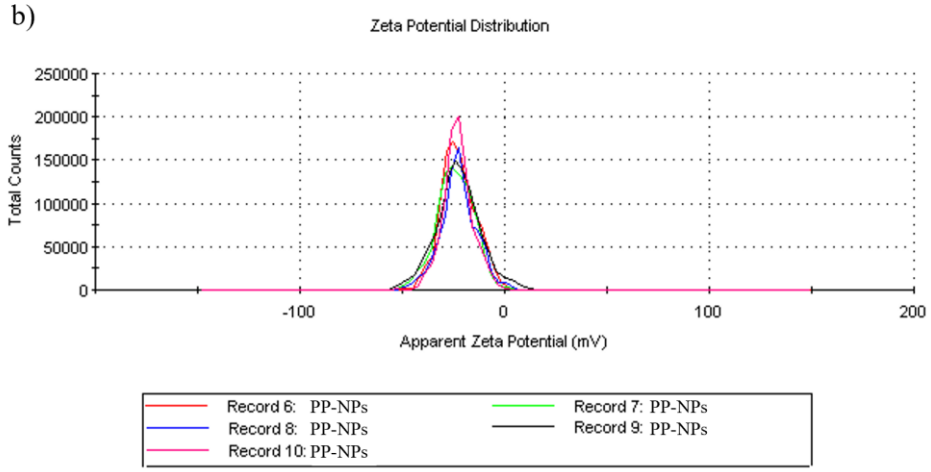

Figure 2.9 Representation of DLS measurements related to the PP-NPs formulation. a) information relating to distribution and PDI (top) and typical spectrum of mean diameter measurements, b) typical spectrum of zeta potential measurements. Different gaussians are related to different consecutive measurements

Table 2.1 shows the average values of the measurements of two different formulations (Form #1 and Form #2), made in different periods for both PP-NPs and HA-PP-NPs.

Table 2.1 Mean Diameter measurements of Form #1 and Form #2.

	Mean Diameter (nm)						
	Time (T_{days})	*T_0*	*T_{10}*	*T_{20}*	*T_{30}*	*T_{40}*	*T_{50}*
Form #1	**PP-NPs**	125 ±1	127 ±2	127 ±1	128 ±1	128 ±1	128 ±1
	HA-PP-NPs	158±2	160±1	164±1	166 ±3	162±1	175 ±5
Form #2	**PP-NPs**	127±2	132±2	130±1	131±1	135±4	138±4
	HA-PP-NPs	162±3	163±1	167±2	179±5	185±1	193±2

The first consideration concerns the comparison between the control formulation and the one with HA, from which it emerges that the difference in the mean diameter values could confirm the presence of the HA coating. This difference, occurring in both Form #1 and Form #2 formulations, indicates that HA coating, at T_0, has an average thickness of 34 nm. However, the difference between the diameters of the two formulation does not remain constant over time, reaching an average value of 51 nm at T_{50}.

By extending the evaluation to a comparison between the two formulations, Form #1 and Form #2, it is possible to make more precise consideration:

- Form #1: the PP-NPs undergo a gradual increase in diameter up to 2.4% after 50 days, unlike the HA-PP-NPs formulation which records an increase of 10.8%.
- Form #2: the PP-NPs undergo a gradual increase in diameter up to 8.6%, while the HA-PP-NPs up to 19% after 50 days.

Table 2.2 reports the monitoring of DPI variations over time, highlighting a tendency towards moderate polydispersion especially for HA-PP-NPs.

Table 2.2 Mean values of Polydispersity Index (PDI) of Form #1 and Form #2

		Polydispersity Index (PDI)					
	Time (T_{days})	*T_0*	*T_{10}*	*T_{20}*	*T_{30}*	*T_{40}*	*T_{50}*
Form #1	**PP-NPs**	0.061 ±0.022	0.045 ±0.007	0.049 ±0.016	0.041 ±0.021	0.034 ±0.023	0.092 ±0.002
	HA-PP-NPs	0.080 ±0.022	0.041 ±0.031	0.133 ±0.013	0.176 ±0.047	0.178 ±0.045	0.182 ±0.011
Form #2	**PP-NPs**	0.070 ±0.004	0.091 ±0.012	0.078 ±0.009	0.068 ±0.016	0.057 ±0.022	0.093 ±0.011
	HA-PP-NPs	0.080 ±0.02	0.102 ±0.021	0.110 ±0.041	0.151 ±0.031	0.172 ±0.021	0.210 ±0.022

The PDI at T_0 is the same for both types of NPs and for both formulation; however, it becomes interesting to comment on what happens in each condition:

- Form #1: the PDI of PP-NPs undergoes an increase not gradual of up to 50% after 50 days, while that of HA-PP-NPs increase by 128%.
- Form #2: the PP-NPs show a gradual increase in DPI up to 33%, while the HA-PP-NPs up to 162.5% after 50 days, thus also exceeding the reference value of 0.2 which guarantees the condition of monodispersion.[39].

Table 2.3 shows the mean values of ζ: usually a difference of at least 10 mV between PP-NPs and HA-PP-NPs confirms the presence of HA coating. At T_0 this difference is verified in both formulations, the 50-day monitoring revealed that some modifications were occurring in the formulations.

Table 2.3 Mean values of Zeta Potential (mV).

		Zeta Potential (mV)					
	Time (T_{days})	*T_0*	*T_{10}*	*T_{20}*	*T_{30}*	*T_{40}*	*T_{50}*
Form #1	**PP-NPs**	-19 ±2	-29 ±3	-26 ±4	-27 ±1	-28 ±2	-20 ±3
	HA-PP-NPs	-32 ±2	-40 ±2	-42 ±2	-38 ±1	-36 ±2	-38 ±1
Form #2	**PP-NPs**	-23 ±0.1	-33 ±0.3	-21 ±1	-21 ±2	-20 ±.1	-19 ±1
	HA-PP-NPs	-31 ±1	-28 ±1	-25 ±0.4	-21 ±1	-21 ±0.3	-20 ±1

From a more in-depth analysis, PP-NPs reach a maximum peak of ζ at T_{10} and then gradually return to values close to those of T_0 in both formulations.

On the contrary, the Zeta Potential of HA-PP-NPs, in the Form #2, manifests a constant increasing trend, whereas that of Form #1 seems to decrease from T_0 to T_{10} reaching a plateau value of about -40 mV.

In an overall view, the formulations, albeit with slightly different trends also due to the experimental conditions (formulation and measurement that are not perfectly reproducible), are stable over time up to a maximum of 50 days.

In a more detailed analysis, the increase in the mean diameter over time remains difficult to interpret, especially for HA-PP-NPs which could be due to various phenomena such as alteration of the tertiary structure of the HA or to the aggregation of HA debris in the solution. Alterations of HA are also confirmed by ζ values which reveal alterations attributable to HA which is not constant over time.

2.3.2 Raman and SERS measurements

Support for the interpretation of previous DLS stability data can come from the Raman spectroscopy analysis. By identifying some characteristic peaks of HA, it would be possible to monitor their variations over time. For these measurements two formulations (Form #3 and Form #4) were performed, but, unlike the previous formulations, PLGA without Rhodamine B was used, as it can give interference during the measurements.

A gradual approach was adopted which involved two experimental sets: the first was DLS of the Form #3 NPs and characterization by Raman spectroscopy, but since the latter technique proved to be insensitive, another experimental set was made with DLS of Form #4 NPs and SERS. Measurements with DLS were performed at the same time as Raman and/or SERS ones.

Step 1: DLS of the Form #3 NPs and characterization by Raman spectroscopy

DLS data characterization of Form #3 just made, and therefore at T_0, are reported in Tab. 2.4:

Table 2.4 DLS measurements of Form #3 at T_0

		Mean Diameter (nm)	***PDI***	***ζ (mV)***
Form #3	**PP-NPs**	102 ±0.5	0.11 ±0.02	-23 ±0.4
	HA-PP-NPs	126 ±3	0.12 ±0.02	-30 ±0.2

The formulation has characteristics that confirm the successful coating of the NPs with HA.

At the same time, measurements of the same sample were started by Raman spectroscopy. First, a characterization of the individual dry

formulation components (PLGA, F127, F68, HA) was made. The results are reported in Fig 2.10.

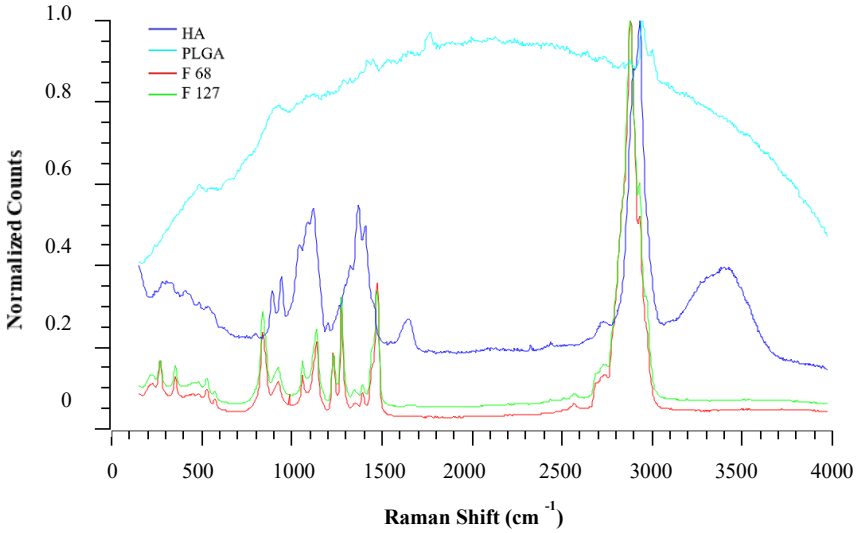

Fig. 2.10 Dry components' spectra with Raman spectroscopy. The signal amplitude is related to the laser power and the signal integration time, which were 15 mW and 50 s. Each signal is normalized to its maximum, in order to make a direct comparison between all spectra.

Except for the poloxamers (F127 and F68) which have similar and superimposable spectra, the PLGA has a very broad spectrum overlying all the others, while HA shows a spectrum with peaks that could be peculiar to the molecule. After this first characterization, for a more realistic measurement, Fig 3.11 shows the spectra of the individual components in solution and at the concentrations used in the formulation protocol (see paragraph 2.2.1).

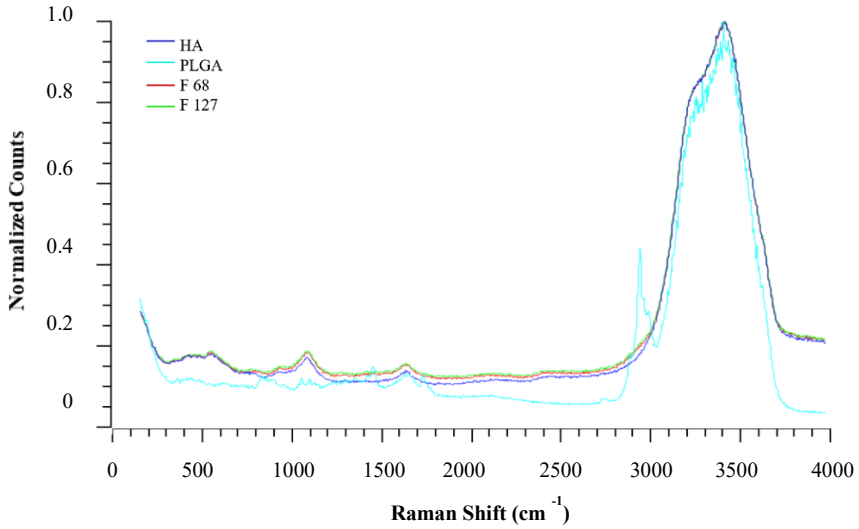

Figure 2.11 Components in solution spectra with Raman spectroscopy. Laser power was 15 mW and the integration time was 50 s.

The spectra of all components appear to be similar and, in particular, it is possible to observe the water stretching peak (referred to vibrational degrees of freedom of O-H bond), around 3400 cm^{-1} characteristics of poloxamer and HA. The PLGA, instead, shows a clear peak between 2900 and 3000 cm^{-1}.

Finally, the two formulations PP-NPs and HA-PP-NPs at concentration of 10^{13} particles/mL were measured and compared with the spectrum of HA in solution, in order to identify any peculiar peaks to monitor over time (Fig.2.12)

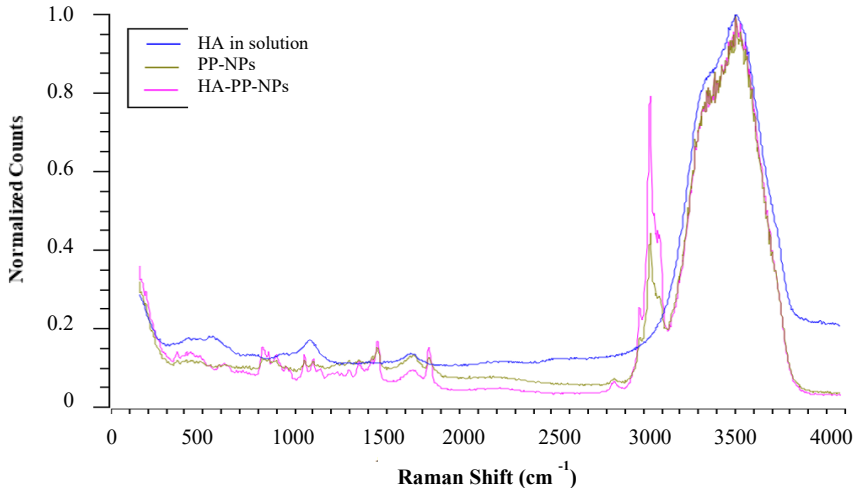

Figure 2.12 NPs formulation spectra with Raman spectroscopy compared whit HA one.

Both formulations have similar spectra to each other, but no peak in common with any of the HA. However, both formulations show a peak at 3000 cm^{-1}, typical of PLGA (as reported in fig 2.11), indicating that Raman spectroscopy does not have sufficient sensitivity to detect the thin HA coating on the NPs.

Considering all the above, SERS, having a higher signal sensitivity than Raman spectroscopy (about 10^{11} orders of magnitude), is the most suitable technique.

Step 2 DLS of Form # 4 NPs and characterization by SERS.

DLS data characterization of Form #4 are reported in table 2.5

Table 2.5 DLS measurements of Form #4 over the time

		Mean Diameter (nm)	***PDI***	***ζ (mV)***	**Time**
Form #4	**PP-NPs**	105±1	0.15 ±0.01	-26 ±1	**T_0**
	HA-PP-NPs	142±7	0.21 ±0.01	-39 ±1	
	PP-NPs	99±2	0.09 ±0.02	-23 ±2	**T_7**
	HA-PP-NPs	123±6	0.15 ±0.02	-28 ±3	
	PP-NPs	105±1	0.19 ±0.01	-23 ±1	**T_{14}**
	HA-PP-NPs	135±1	0.20 ±0.02	-29 ±1	

HA coating was carried out (the average thickness of HA over time is 30 nm). At T_7, the HA-PP-NPs undergo a decrease in the mean diameter (about 10%) to approach values like the starting ones (deviation of 5% at T14,). The trend of the PDI indicates that the formulation is stable over time. ζ shows a decrease of 28% at T_7 and 25% at T_{14} revealing that the surface of the HA-coated nanoparticles is increasing.

These results support the hypothesis that there may be alterations in HA that affect the characteristics of the formulation.

At the same time points (T_0, T_7 and T_{14}) the measurements by SERS were performed. Figure 2.13 shows a first comparison between the Raman and SERS spectra of the single components with the HA- PP-NPs formulations (at T_0 and T_7). Analysing the latter with respect to the single components, in addition to the peaks common with the poloxamers (at 2879 cm^{-1}), NPs have a region in common with SERS spectrum of HA at values below 1000 cm^{-1} and which do not find similarities with the spectra of the other components.

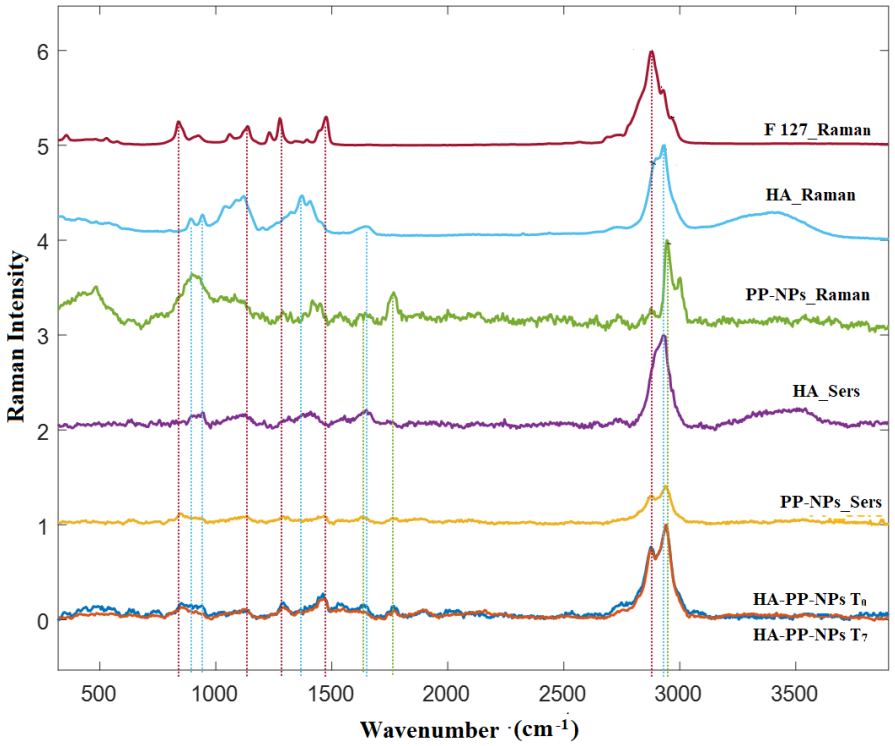

Figure 2.13 Comparison between Raman and SERS spectra. The Raman spectra of the two poloxamers are superimposable, therefore the spectrum of F127 is shown (in red), also confirmed by the FTIR [47], and those of HA and PLGA in solution (in blue and green, respectively). The SERS spectra of HA in solution (in purple), those of PP-NP (in yellow) and of HA-PP-NP at T_0 and T_7 from the formulation (in orange and blue, respectively).

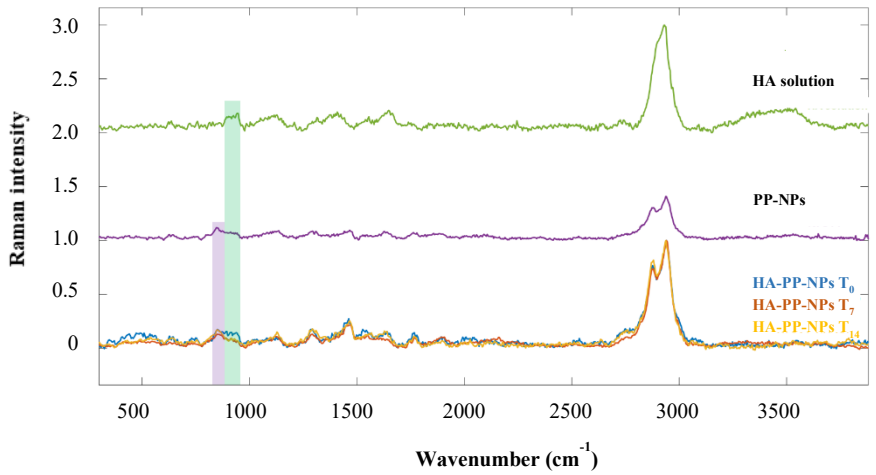

Figure 2.14 Comparison of SERS spectra of HA- PP-NPs relative to T_0, T_7, T_{14} with the SERS spectrum of HA in solution (in green) and PP-NPs (in purple).

An in-depth analysis carried out by considering the spectra of HA-PP-NPs at all time points (T_0 - T_{14}) revealed that in this region two interesting peaks close to each other highlighted in Fig. 2.14 and which are connected to the spectra of HA and of HA-PP-NPs. Figure 2.15 highlights the variations of these peaks in HA-PP-NPs as a function of time. In fact, it appears clear that fresh formulations (T_0 and T_7) show peaks corresponding to HA; unlike the measurement at T_{14} in which the typical peaks of HA disappear, resulting in spectrum close to that of PP-NPs.

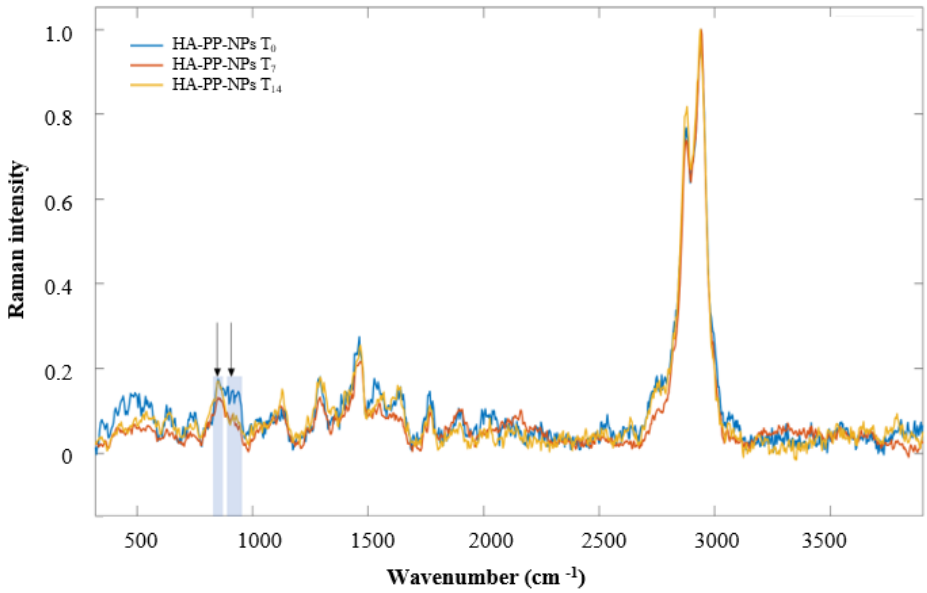

Figure 2.15 Identification of specific HA peaks and measurements of their variation over time in HA-PP-NPs.

In particular, the spectral region between 800 and 900 cm^{-1} shows quite isolated peaks that denote a clear variation in intensity (Fig. 2.16).

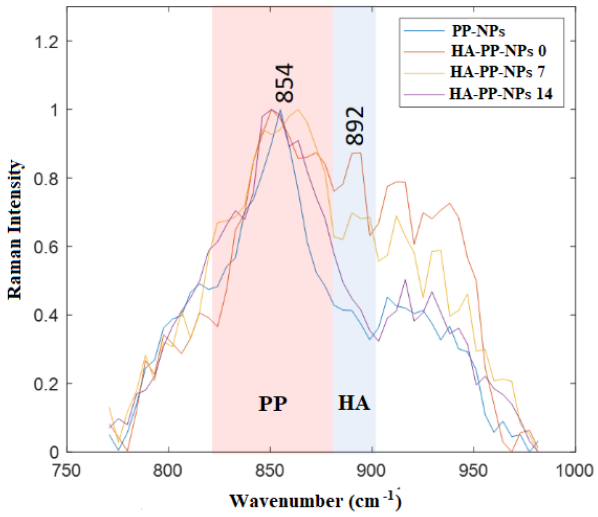

Figure 2.16 Specific wavenumber of SERS peaks for HA and PP.

Interestingly, these two peaks correspond to those of PLGA and HA. Normalizing the spectra with respect to the PLGA peak, a decrease in the HA peak is observed. These evidences confirm that the formulations preserve the HA coating for a maximum of 7 days.

To highlight differences between these spectra, it is advantageous to analyse the spectra by means of PCA. A set of SERS measurements performed on a pure HA sample at the concentration of 0.25% w/v was included in the analysis and considered as control. The PCA scores in Fig.2.17 shows a clear difference between the two populations (PP-NPs and HA-PP-NPs) along PC1. It is notably that the HA-PP-NPs population tends to overlap the set of spectra of HA.

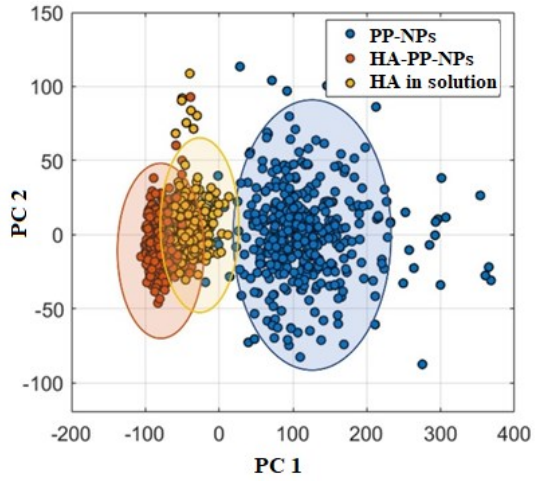

Figure 2.17 Score plot of PC1 versus PC2 for PP-NPs and HA-PP-NPs and HA.

Fig 2. 18 shows the PCA processing to evaluate the aging of the formulations confirming the information reported by the spectra of Fig. 2.16

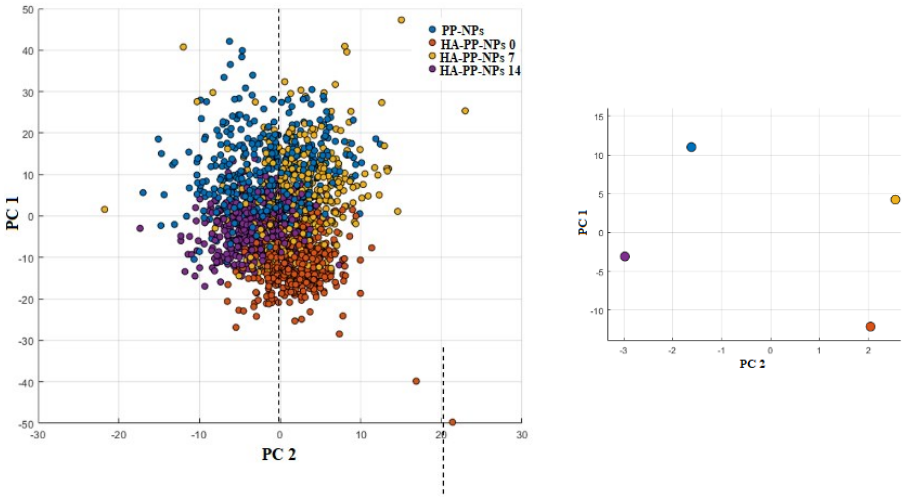

Figure 2.18 Score plot of PC1 versus PC2 for PP-NPs and HA-PP-NPs over the time (left) and average value for each population (right).

In this plot the control is represented by naked NPs (PP-NPs) that occupy negative part along PC2. It is evident how the formulations are distributed according to time. At T_0 and T_7 they occupy positive values along PC2 and are partially overlapped, indicating properties different from those of the control. At T_{14} the HA-PP-NPs population overlaps with the control and therefore of naked NPs. In fig 2.18 b) result is even more evident by reporting only the average value for each population analysed.

References

1. Dollinger M. 1996. *Oncologist*. **1**(1 & 2):107-111.
2. Zraik IM, et al. 2021. *Urologe A*. **60**(7):862-871. doi:10.1007/s00120-021-01569-7.
3. Qin SY, et al. 2018. *Biomaterials*. **171**:178-197. doi:10.1016/j.biomaterials.2018.04.027.
4. Chew HK. 2001. *West J Med*. **174**(4):284-287. doi:10.1136/ewjm.174.4.284.
5. Fisusi FA, et al. 2019. *Pharm Nanotechnol*. **7**(1):3-23. doi:10.2174/2211738507666190122111224.
6. Giordano SH. 2003. *Oncologist*. **8**(6):521-530. doi:10.1634/theoncologist.8-6-521.
7. Wang M, et al. 2017. *Sci Rep* **7**:44673. doi:10.1038/srep44673.
8. Kümmel S, et al. 2014. *Br J Surg.* **101**(8):912-924. doi:10.1002/bjs.9545.
9. Darby S, et al. 2011. *Lancet.* **378**(9804):1707-1716. doi:10.1016/S0140-6736(11)61629-2.
10. Rashid OM, et al. 2014. *J Womens Health (Larchmt).* **23**(2):184-188. doi:10.1089/jwh.2013.4517.
11. Hortobagyi GN. 1998. *N Engl J Med*. **339**(14):974-984. doi:10.1056/NEJM199810013391407.
12. Luqmani YA. 2005. *Med Princ Pract.* **14**(suppl.1):35-48. doi:10.1159/000086183.
13. Wu Q, et al. 2014. *Cancer Lett*. **347**(2):159-166. doi:10.1016/j.canlet.2014.03.013.
14. Wang J, et al. 2017. *Oncotarget.* **8**(48):84559-84571. doi:10.18632/oncotarget.19187.
15. Wang X, et al. 2019. *Cancer Drug Resist*. **2**(2):141-160. doi:10.20517/cdr.2019.10.
16. Dallavalle S, et al. 2020. *Drug Resist. Updat.* **50**:100682. doi:10.1016/j.drup.2020.100682
17. Sørlie T, et al. 2001. *Proc Natl Acad Sci USA*. **98**(19):10869-10874. doi:10.1073/pnas.191367098.
18. Sonnenblick A, et al. 2016. *Mol Oncol.* **10**(8):1147-1159. doi:10.1016/j.molonc.2016.07.002.
19. Gu G, et al. 2016. *Curr Opin Pharmacol*. **31**:97-103. doi:10.1016/j.coph.2016.11.005.
20. Kang C, et al. 2020. *Drugs*. **80**(6):601-607. doi:10.1007/s40265-020-01295-y.
21. Shi J, et al. 2017. *Nat Rev Cancer*. **17**(1):20-37. doi:10.1038/nrc.2016.108.
22. Avitabile E, et al. 2018. *Nanoscale.* **10**(25):11719-11731. doi:10.1039/C8NR02796J.
23. Strambeanu N, et al. 2015. In: Lungu M, Neculae A, Bunoiu M, Biris C. (eds) Springer, Cham. doi:10.1007/978-3-319-11728-7_1

24. Brigger I, et al. 2021. *Adv Drug Deliv Rev.* **54**(5):631-651. doi:10.1016/s0169-409x(02)00044-3.
25. Hashizume H, et al. 2000. *Am J Pathol*. **156**(4):1363-1380. doi:10.1016/S0002-9440(10)65006-7.
26. Kobayashi H, et al. 2013. *Theranostics.* **4**(1):81-89. doi:10.7150/thno.7193.
27. Owens DE 3rd, et al. 2006. *Int J Pharm*. **307**(1):93-102. doi:10.1016/j.ijpharm.2005.10.010.
28. Cevc G. 2012. *J Control Release.* **160**(2):135-46. doi:10.1016/j.jconrel.2012.01.005.
29. Qi SS, et al. 2017. *Drug Deliv.* **24**(1):1909-1926. doi:10.1080/10717544.2017.1410256.
30. Pérez-Herrero E, et al. 2015. *Eur J Pharm Biopharm*. **93**:52-79. doi:10.1016/j.ejpb.2015.03.018.
31. Barriga HMG, et al. 2019. *Angew Chem Int Ed Engl*. **58**(10):2958-2978. doi:10.1002/anie.201804067.
32. Krzysztof S, et al. 2018. *Mol. Pharm.* **16**(1)1-23. doi:10.1021/acs.molpharmaceut.8b00810.
33. Wu L, et al. 2011. *Adv Drug Deliv Rev*. **63**(6):456-469. doi:10.1016/j.addr.2011.02.001.
34. Shang L, et al. 2014. *J Nanobiotechnol.* **12**(5) doi:10.1186/1477-3155-12-5
35. Bhattacharjee S, et al. 2012. *Part Fibre Toxicol*. **9**(11). doi:10.1186/1743-8977-9-11
36. Menon JU, et al. 2012. *J Biomed Mater Res A*. **100**(8):1998-2005. doi:10.1002/jbm.a.34040.
37. Della Sala F, et al. 2022. *Colloids Surf B Biointerfaces*. **210**:112240. doi:10.1016/j.colsurfb.2021.112240.
38. ZetaSizer Nano Series Manual. Available from: https://www.chem.uci.edu/~dmitryf/manuals/Fundamentals/DLS%20measurement%20principles.pd.
39. Danaei M, et al. 2018. *Pharmaceutics.* **10**(2):57. doi:10.3390/pharmaceutics10020057.
40. Honary S, et al. 2013. *Trop J Pharm Res*. **12**(2):255. doi:10.4314/tjpr.v12i2.19.
41. Honary S, et al. 2013. *Trop J Pharm Res*. **12**(2):265. doi:10.4314/tjpr.v12i2.20.
42. Le Ru EC, et al. 2013. *MRS Bulletin.* **38**(8):631-640. doi:10.1557/mrs.2013.158.
43. Geraldes CFGC. 2020. *Molecules.* **25**(23):5547. doi:10.3390/molecules25235547.
44. Pérez-Jiménez AI, et al. 2020. *Chem. Sci.* **11**(18):4563-4577. doi:10.1039/d0sc00809e
45. Yang J, et al. 2014. *Photonics.* **1**(4):380-389. doi:10.3390/photonics1040380.

46. Capaccio A, et al. 2020. *Nanoscale*. **12**:24376–24384. doi:10.1039/d0nr05107a
47. Liu Y, et al. 2017. *Int J Nanomedicine*. **12**:2635-2644. doi:10.2147/IJN.S122746.

Chapter 3 – Radiotherapy and internalization of HA-PP-NPs, a new potential approach for drug delivery

3.1 Background

The management of cancer treatment, the choice of therapy, the stage of the disease and the patient's response are the fundamental inputs to study and adopt the best strategy. Many studies are aimed at designing specific NPs capable of recognizing only the target cells or the choice of treatment plans that involve the use of multiple chemotherapeutics to minimize MDR and reduce adverse effects. In addition, also radiotherapy faces new perspectives in evaluating the effects on diseased tissues, suggesting that new combinations are possible with respect to standard treatment plans.

The aim of this part of the work was to investigate how the effects of radiotherapy treatment can influence, from a biomechanical point of view, the internalization processes of functionalized NPs. The rationale was to exploit hoe the overexpression of CD-44 in tumor cells can be used to promote the internalization of NPs decorated with HA, which was the decoration of NPs. However, reactions within the cellular environment could impair targeting effectiveness, e.g., the formation of the protein corona on NPs surface, potentially representing a limitation of the starting ratio. It has been shown that the effects of the ionizing radiations could represent a solution or at least a factor facilitating the internalization process by tumor cells.

3.1.1 Internalization pathways in cancer

Cancer cells have particular characteristics such as an altered enzyme set or the expression of specific membrane receptors. These characteristics can be exploited to selectively convey the carriers into the tumor limiting adverse effects of a systemic therapy. In fact, conventional chemotherapy

delivers the anticancer drug indiscriminately; both to tumors and to normal tissues, causing secondary effects that have a negative impact on the patient's well-being. Using features unique to tumors to selectively administer the drug is an effective remedy.

A peculiarity of solid tumors is a reduced lymphatic drainage which facilitates the accumulation of NPs within the tumor. This phenomenon was first described about forty years ago and is known as the *"enhanced permeability and retention effect"* (EPR) [1].

Tumor cells proliferating in an uncontrolled way induce greater angiogenesis for a sufficient supply of nutrients and oxygen [2]. This neovascularization is totally different from that of normal tissues starting from the anatomical architecture. The blood vessels in the tumor, in fact, are dilated, leaky and with large fenestrations. Furthermore, perivascular cells and the basement membrane, or smooth muscle layer, are frequently absent or abnormal in the vascular wall. In addition, some vascular mediators such as nitric oxide, bradykinin and endothelial growth factor play a fundamental role in the development of tumors and their metastases and can influence the EPR effect in solid tumors. Therefore, the modulation of these factors can increase the EPR effect and NPs accumulation within the tumor (Fig 3.1).

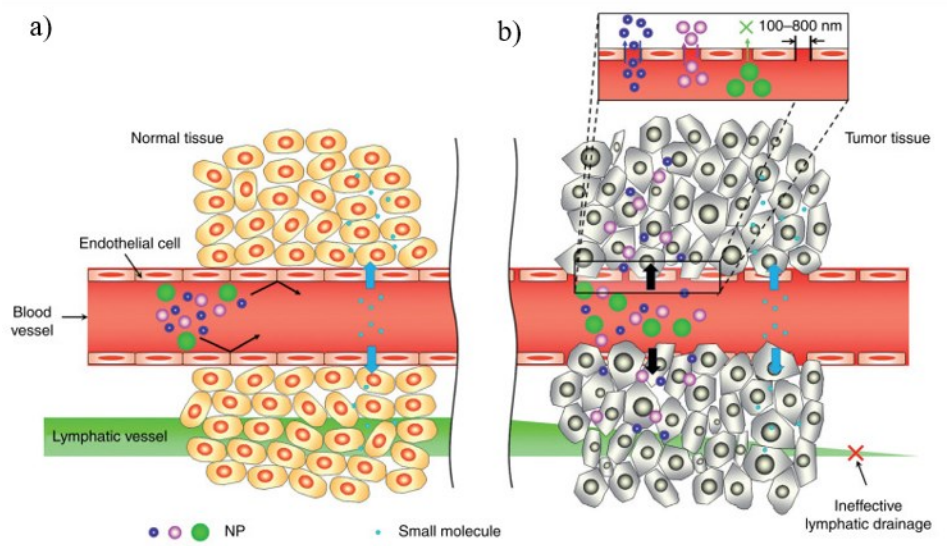

Figure 3.1 EPR effect on uptake of NPs across a) normal and b) cancerous tissues. Adapted from [3]

NPs can accumulate within tumor tissues through mechanism of passive and active "targeting". Passive “targeting” is based on two physiological phenomena that occur at the level of blood circulation, diffusion, and convection. Diffusion is responsible for the transport, across cell membranes, of very lipophilic substances with low molecular weight, according to the concentration gradient. Convection is a process resulting from the motion of blood and is responsible for the transport of large molecules through the large fenestrations present between the endothelial cells of the tumor vessels. The EPR effect allows the NPs to passively accumulate in tumor vessels without any surface modification.

In active targeting, NPs are modified with specific ligands for receptors and other molecules expressed on the surface of tumor cells. Conjugation with these ligands avoids the interaction of NPs with tissues other than tumor tissue.

Figure 3.2 schematically illustrates the main pathways of internalization of NPs by cells.

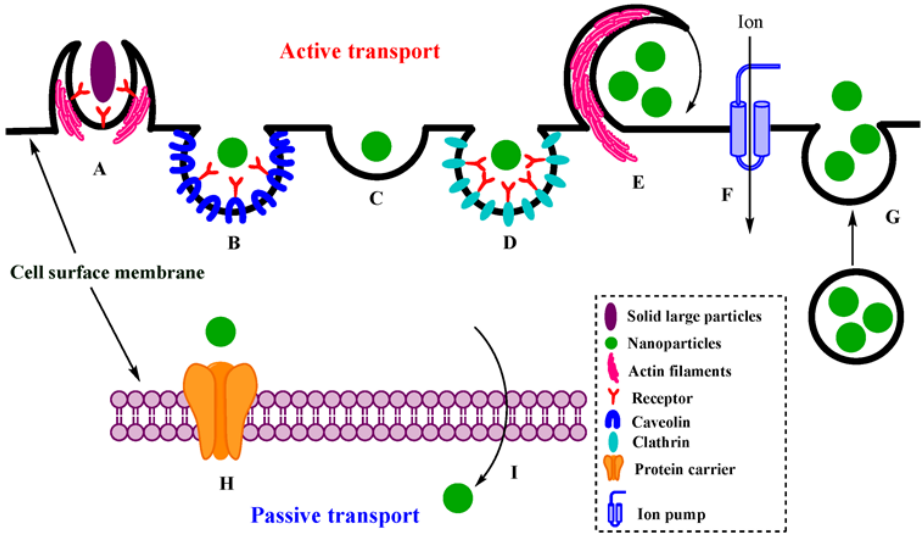

Figure 3.2 The main cellular uptake pathways: (A) phagocytosis, (B) caveolin-mediated endocytosis, (C) clathrin-caveolin-independent endocytosis, (D) clathrin-mediated endocytosis, (E) macro-pinocytosis, (F) ion pumps, (G) exocytosis, (H) facilitated diffusion and (I) simple diffusion. Adapted from [4].

3.1.2 Drug delivery in breast cancer: case of CD-44 receptor and NPs HA coated

As for all cancers, breast cancer presents some peculiar characteristics useful for designing a targeted therapy using functionalized NPs in order to maximize the effectiveness of drug delivery.

The rationale of this research project is based on the role of an overexpressed transmembrane receptor, cluster determinant 44 (CD-44), in targeted therapy. CD-44 plays a wide range of functions, among which it is responsible for intercellular adhesion, cell orientation, migration, and the signalling process of matricellular cues [5].

The therapeutic importance of a receptor is linked to the possibility of correlating its level of expression to a specific disease. CD-44 is associated with malignant tumors when it is overexpressed in higher molecular weight isoforms (e.g., CD-44v) [6] which will then correspond to the type of cancer cells. This feature makes CD-44 both a diagnostic and prognostic marker (breast, prostate, bowel, head and neck, pancreas, and colorectal cancers) [7].

The pharmacological approach, on the other hand, is based on the ability of CD-44 to bind specific ligands and usually includes two main classes of targeted therapeutic agents:

- substances that exploit the natural mechanism of CD-44 mediated endocytosis (HA and its derivatives)
- substances with high affinity for a specific isoform or for all of CD-44 (monoclonal antibodies)

The advantages of HA-based carriers over CD-44 antibodies are lower cost, compatibility with different active pharmaceutical ingredients and better binding and internalization mechanism with different receptor isoforms. On the other hand, antibodies allow a targeted and precise action at the molecular level.

Given CD-44 high molecular variability [8], the use of antibodies is limited and dependent on the molecular characterization of the specific variant, for this reason the choice fell on the formulation and use of HA-functionalized NPs.

HA is a linear polyanionic polymer composed of repeating disaccharide units of D-glucuronic acid (GlcUA) and N-acetyl-D-glucosamine (GlcNAc), that are linked together through alternating beta-1,3 and beta-1,4 glycosidic bonds. It is a component of the ECM, highly water-soluble

and biodegradable polymer, abundant in the embryonic tissues [9]. Also, HA interacts with specific cell membrane receptors and functions as a signalling molecule, regulating cell adhesion, migration and proliferation. Therefore, this molecule has an important role in many physiological and pathological conditions [10, 11]. HA biocompatibility, biodegradability and non-immunogenicity make this molecule the perfect surface decoration of NPs for an active tumor targeting. The degradation of HA molecule after administration can follow two paths: (1) when the molecule travels in the bloodstream it is catabolized in lymph nodes and in the liver, (2) while it is degraded by the lysosomes after the internalization in the cell.

HA has a wide molecular weight (MW), ranging from 1000 to 10,000,000 Da, and it plays different roles in the body depending on its MW: high MW has anti-inflammatory actions and generally inhibits cell movement, and it is related to cancer resistance; while low MW HA is pro-inflammatory, promotes angiogenesis and enhances cell motility, so, it is linked to tumor progression.

Breast cancer cells are known to have greater HA uptake than normal tissues required by overexpression of P-glycoprotein (P-gp), which contributes to multidrug resistance. CD-44 also seems to be strongly related to P-gp, the main protein associated to multidrug resistance in tumoral cells [12]. It seems that the overactivation of one of these two proteins may lead to the regression of the other: this would mean that increasing the CD-44/HA complex formation ratio by adding a large amount of HA near tumoral cells, can reverse the multiple drug resistance mediated by P-gp [13]. Using CD-44 as a target for NPs-mediated

chemotherapy thus can lead to an increased sensitivity of tumoral cells towards the chemotherapeutic drug.

It is also known that increasing levels of CD-44 expression in human breast cancer cell lines are closely correlated with their capacity to bind, internalize and degrade HA [14].

3.1.3 Therapeutic applications: some challenges

HA appears to be an excellent candidate for use in the therapeutic field both for its metabolic kinetics and for its chemical versatility. After being absorbed by tumor cells through receptor-mediated endocytosis, HA is easily degraded to low molecular weight components (hyaluronidase) thus exposing the drug [15]. Furthermore, HA has several functional groups that allow conjugation with different chemicals making it functional for different therapeutic applications. Fig 3.2 shows some possible modifications: the carboxyl groups of HA can be modified to obtain hydrazide groups to promote covalent bonds with drugs. Methacrylate, and tyramine modification is used to prepare crosslinked hydrogels. The HA functionalization with, can also be used to coat gold NPs. Dialdehyde HA is instead used for conjugates or the formation of pH-sensitive hydrogels.

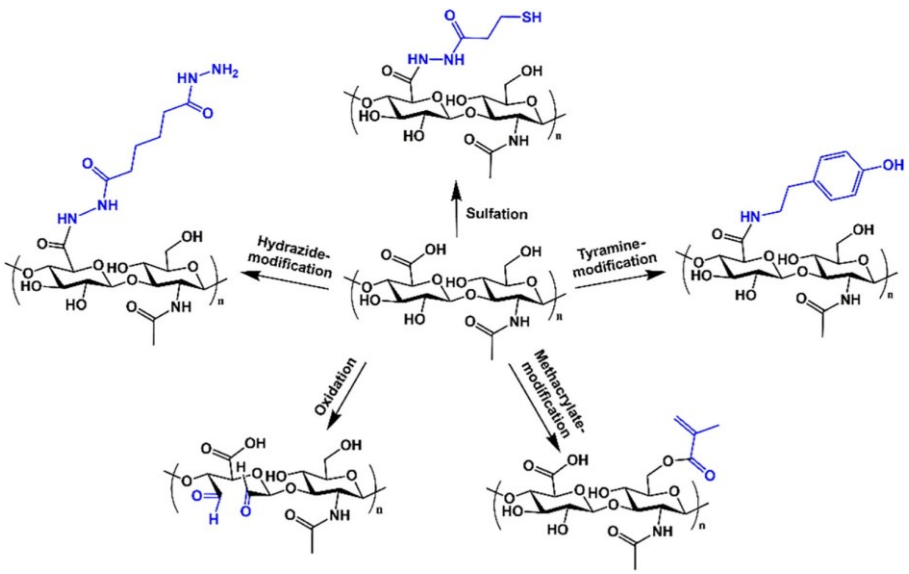

Figure 3.2 Chemical modifications of HA. Adapted from [16].

Versatility of this molecule makes it one of the elements suitable for the design of functionalized drugs in order to reduce the adverse effects of systemic administration.

In particular, breast cancer, despite the numerous drugs approved and adopted in clinical practice, has an increasingly widespread MDR, making urgent the development of alternative approach. Nanomedicine may be a solution, however there are still few drugs approved by the Food and Drug Administration (FDA): Doxil, albumin-bound paclitaxel nanoparticles (Abraxane), PLA micelle-based paclitaxel (Genxol) and paclitaxel-loaded liposomes [17].

This is also the reason why a large part of the attention is directed towards studies involving the use of biocompatible molecules with high specificity, such as HA. A very important aspect that the scientific community is still studying is the control of targeted therapy involving the selectivity and binding mechanisms of HA and CD-44.

In addition to CD-44, HA interacts with several membrane receptors having an extracellular domain called "LINK module". By conformational modifications, it allows binding to HA. Fig. 3.3 shows the main receptors of HA, cytoplasmic and especially membrane, divided into two superfamilies: a) Link-modules, among which gene-6 stimulated by tumor necrosis factor (TSG-6), endocytic receptor of lymphatic vessels (LYVE-1), HA receptor for endocytosis (HARE); and b) non-link receptors, among which receptor for hyaluronan mediated motility, CD168 (RHAMM) and intracellular adhesion molecule-1 (ICAM-1). Of the latter, one has a domain with a series of seven amino acids flanked by a residue of arginine or lysine; the other one has a cluster of basic amino acids not containing acid residues. Both receptors have HA binding sites similar to CD-44 [18].

	A I LINK-module superfamily				B I non-LINK receptors	
	TSG-6	**LYVE-1**	**CD44**	**HARE**	**RHAMM**	**ICAM-1**
Localization	Soluble (ECM)	Cell surface	• Cell surface • Soluble (ECM)	• Cell surface* • Soluble: trimer / monomer (cytopl.)	• Cytoplasmic • Cell surface*	• Cell surface • Soluble (cytopl.)
Expression	Inflamed milieu	• ECs of liver, spleen, and lymphatics • Macrophages	• Leukocytes • Fibroblasts and ECs • Tumors (overexp.) • Inflamed milieu	• ECs of liver, spleen, and lymphatics	• Leukocytes • ECs • Several tumors (overexp.)	• Leukocytes • ECs
Functional role	Anti-inflammatory	• Lymphatic HA transport • Metastasis	• Development • Inflammation • T-cell recruitment • Tumor progression	Systemic GAGs clearance	• Cell migration • Tissue injury and repair	Signaling roles upon HA binding
Ligands	**Main:** HA **Other:** aggrecan, versican, TSP I & II, PTX-3, fibronectin	HA	**Main:** HA **Other:** OPN, collagen, MMPs, GAGs	HA, DS, and CnS (A, C, D, and E)	HA	HA, LFA-1

Figure 3.3 HA receptors of a) LINK-module superfamily and b) non-LINK receptors. TSP, thrombospondin; PTX-3, pentraxin-related protein; GAGs, glycosaminoglycans; OPN, osteopontin; DS, dextran sulfate; CnS, chondroitin sulfate type A, C, D, and E; LFA-1, lymphocyte function-associated antigen 1. Adapted from [19].

In this scenario it is clear that there are several CD-44 competitors that could cause off-target effects, and for this reason the discussion on a targeted therapy oriented exclusively on CD-44 is still open.

Among all competitors, HARE, promotes endocytosis and catabolism of HA and is responsible for the physiological turnover of one third of total HA per day [20]. One solution could be a pre-administration of low molecular weight HA to saturate HARE [21], even if this effect lasts less than 15 min [22].

Although CD-44 remains the main receptor of HA, it has intrinsic elements that could cause off-target effects due to alternative splicing and the different isoforms that derive from it. In general, it is possible to distinguish two broad categories of isoforms: CD-44s expressed mainly in healthy tissues [23] and CD-44v overexpressed in tumoral cells [24] and with a higher affinity for HA than CD-44s [25].

One of the aspects still little studied nowadays is the effect of ionizing radiation on the internalization processes of NPs by tumor cells. Some interesting information on the effects of ionizing radiation derives from studies on triple negative tumor cells such as MDA-MB-231 which, after irradiation at different doses (2, 4, 6 or 8 Gy), showed an increase in the expression of cancer stem cells [26]. These cells, at the base of the radioresistance, induce an alteration of growth factors and invasiveness promoters, including an overexpression of CD-44. Could this also translate into an increased interaction with HA and therefore the ability to internalize?

The results reported in chapter 2 were the background on which to build the hypothesis of the experiment that will be described below.

After irradiation treatments, the intake of HA-PP-NPs by healthy and tumor cells irradiated at traditional doses of radiotherapy cycles was evaluated. The aim was to investigate whether, in addition to the known

affinity of HA for CD-44, the cytoskeletal responses to the physical insult of ionizing radiation may affect the internalization capability.

3.2 Materials and methods

In this session the principle of targeted therapy intersects with the physical effects of ionizing radiation. Healthy and tumoral breast cells were irradiated according to the protocol already described in chapter 1, subsequently they were incubated with PP-NPs and HA-PP-NPs for two-time intervals, and finally their cell internalization was quantified.

The cells were seeded on glass plates assuming they could better mimic the stiffness of the tumor microenvironment. Therefore, if in the previous experiment (chapter 1) there were two scenarios (healthy and tumor ECM), in this one only the pathological one with a greater stiffness is considered.

Most of the materials and methods have been covered previously: in chapter 1 cells lines (see 1.2.1), staining protocol (see 1.2.6), X-ray irradiation (see 1.2.4 and Appendix C) and confocal microscope have been described; while, in chapter 2 the NPs formulation protocol (see 2.2.1).

3.2.1 Experimental condition

The experimental conditions included:

- healthy and breast cancer cell lines (MCF10A and MDA-MB-231, respectively);
- two doses of irradiation (2 and 10 Gy);
- two times after irradiation (24 and 72 h):
- two incubation times for both formulations of NPs (5 and 24 h).

Both cell lines were seeded on glass plates.

In order to preserve the cells during the transport to the facility, the medium was supplemented with HEPES Buffer (Fisher Scientific), to maintain a physiological pH despite the changes in carbon dioxide concentration. After irradiation, the cell plates were washed in PBS 1× and new warm medium was added before incubating them at 37 °C.

After staining, image acquisition was performed with confocal microscope. Pinhole size of 55 μm and z-stacks (0.41 μm steps) were recorded covering total cell volume. The resolution was set at 2048 × 2048 pixel (0.5 μm/px). Image analysis was performed by Image J software.

3.2.2 Spectrofluorometer

The main components of a spectrofluorometer are a light source, an excitation monochromator, a sample cuvette, an emission monochromator and a detector, as shown in Fig. 4.4. The light from the source reaches the excitation monochromator, which transmits a specific wavelength to the sample. After excitation, the sample emits light in a range of emission, at higher wavelengths than the excitation ranges and this is collected by the emission monochromator and then reaches the detector. The Stokes shift is the phenomenon which enables fluorescent substances to be discriminated and consists in a difference between the absorption and the emission energy of a sample. This happens due to the difference between the energy needed from molecules to be excited and the energy that they release in the de-excitation process. In fact, after the electrons in the ground state are excited in higher energy states, they can lose some energy due to atoms vibrational motion, so that the energy released during the de-excitation process is lower than the initial energy gained from an external source, such as the excitation laser of the spectrofluorometer. The second monochromator is needed to minimize the scatter of light before reaching

the detector, which could change the emission response of the sample. Most spectrofluorometers also have a reference sample, a strongly fluorescent solution with a broad absorbance spectrum, which helps to correct the lamp output, especially when varying the excitation wavelength, and it corrects the output for differences in detector sensitivity [89].

NPs formulations can have a different concentration, and this has to be considered during the contact with cells, in order to give each condition a sufficient NPs concentration in the cell medium to be internalized and fully exploit cell internalization capability. This is the reason why, before performing this test, the fluorescent signals of both formulations were characterized to determine the quantity of solution to add in each glass dish containing cells.

The assumption of the calibration was to choose the same fluorescence value for both formulations and to use the corresponding dilution factor. Calibration was performed using clear 24-well multi-wells (Fig. 3.5) and consists in filling each group of three wells with a different known solution dilution, in order to link the fluorescence signal to the NPs concentration for both PP-NPs and HA-PP-NPs.

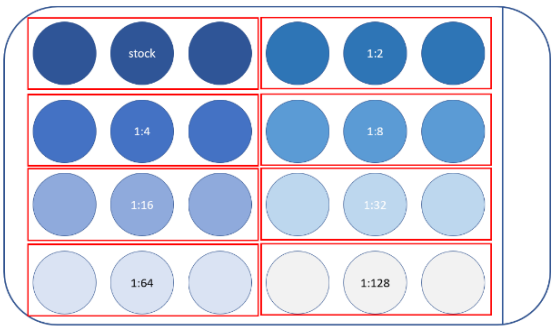

Figure 3.5 Multiwell division for NPs calibration curve. Stock wells are fill NPs formulation produced.

From the calibration curve an arbitrary fluorescence signal (equal for both formulations) was selected as the concentration of PP-NPs and HA-PP-NPs to put in contact with cell in culture.

3.3 Results and discussion

This paragraph reports the results of the calibration curves to define the dilution factor to be used for the experiment, and of the dimensional characterization study of the NPs in the culture medium. Finally, the amount of internalized NPs was quantified in terms of fluorescence signals.

The experimental activity was carried out thanks to a collaboration with various departments of the University of Naples Federico II: the laboratories of the Pharmaceutical Company, Technological Section of the Pharmacy department (for the formulation of NPs), Istituto Nazionale Tumori IRCCS Fondazione G. Pascale, in Naples (for radiotherapy treatment) and the Interdepartmental Research Center on Biomaterials and the Department of Chemistry, Materials and Production Engineering (for the dimensional analyses at DLS and acquisitions of images).

3.3.1 NPs calibration curves

The calibration curve (Fig. 3.6) was used to establish the dilution factor of each formulation based on the same fluorescence signal.

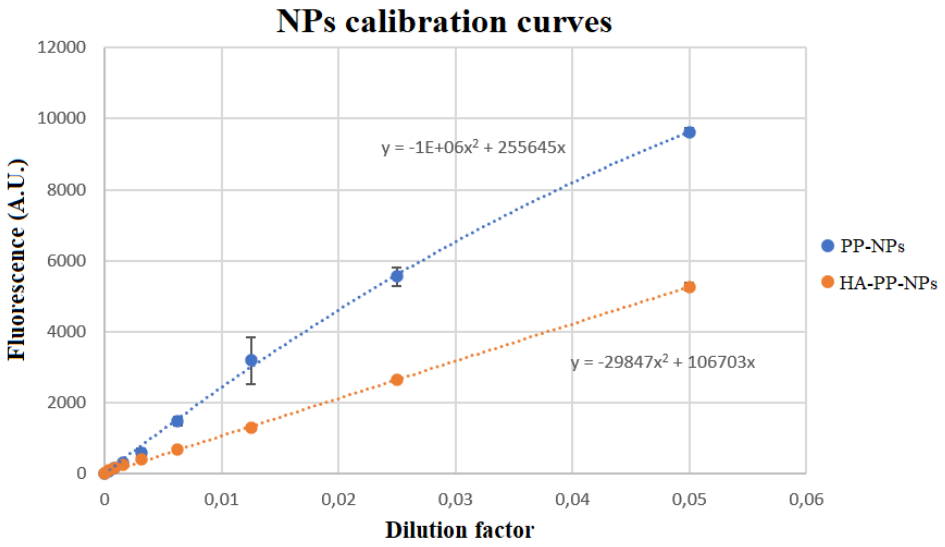

Figure 3.6 PP- and HA-PP-NPs calibration curves

As described in the paragraph *3.2.2,* the fluorescence of solution with a known dilution factor was measured. The average value of background (solution without NPs) was subtracted from those of solutions with NPs for obtaining calibration curves (Figure 3.6). The experimental data were fitted with quadratic equations (goodness of fit R^2 greater than 0.9).

The analysis revealed that the initial, but unknown, concentration of PP-NPs was greater than that of HA-PP-NPs. Then, the dilution factors to obtain the same fluorescence (~ 1320 A.U.) and, as a consequence, the same concentration, were 0.42% and 0.72% for PP-NPs and HA-PP-NPs, respectively.

3.3.2 DLS measurements under experimental conditions

Dimensional characterization of the formulations was carried out with DLS in 3 different solvents: i) in double distilled water (ddH20); ii) in medium without serum; iii) in complete medium. In Tab. 3.1 the mean values and standard deviations of 5 measurements for each individual sample are reported.

Table 3.1 Dimensional measurements of mean diameter, polydispersity index (PDI) and Zeta Potential (ζ) of Form #5 in different solvents.

		Mean Diameter (nm)	***PDI***	**ζ *(mV)***	**Solvent**
Form #5	**PP-NPs**	128 ±2	0.08 ±0.01	-21 ±2	**ddH_2O**
	HA-PP-NPs	167 ±6	0.11 ±0.12	-29 ±2	
	PP-NPs	153 ±2	0.19 ±0.17	-10 ±1	**Medium without serum**
	HA-PP-NPs	195 ±6	0.15 ±0.12	-11 ±1	
	PP-NPs	175 ±6	0.29 ±0.17	-11 ±1	**Complete medium**
	HA-PP-NPs	213 ±8	0.37 ±0.20	-11 ±1	

Comparing the variations in the mean diameter of the same formulation in different solvents, it is evident that the serum makes a significant contribution to modify NPs chemical-physical characteristics. PP-NPs mean diameter increases, compared to the control (ddH_2O), by 19% and 36% in medium without serum and in complete medium, respectively. HA-PP-NPs formulation increases its diameter by 14% and 30% in 2 different solvents. This similar increase between the two formulations reveals that the interaction with the solvent occurs in the same way regardless of the nature of the formulation. If the contribution of the medium without serum can be considered insignificant from the dimensional point of view, the contribution of salts dissolved in the complete medium is instead relevant. The values of ζ are constant, confirming a sort of *saturation phenomenon* [28].

The most plausible hypothesis to the enhancement of NPs size in complete medium is that the well-known phenomenon of the formation of the protein corona has occurred [29]. Protein corona has often been considered an obstacle to drug delivery and targeted therapy of NPs as it creates a new "biological" entity with its own bioavailability and kinetics. Although there are about 4000 different proteins in human plasma, only a few hundred are adsorbed on the surface of the nanosystem and of these, a few dozens are found in the protein corona [29]. Physico-chemical characteristics of the NPs influence the formation of the protein corona, including size. For example, large particles offer more surface interaction for each protein [30]; on the other hand, smaller ones have higher surface curvature that leads to less influence on the protein's conformation [31]. Among the many, another factor that influences the formation of the protein corona is the chemical nature of the surface: HA, due to its hydrophilicity, presents a protein-repellent shield around the NP, thus limiting the influence of the protein corona on drug delivery [32].

3.3.3 Acquisitions and internalization analysis

Both NPs were incubated with MCF10A and MDA-MB-231 cells at 37°C for two different time points: 5 and 24 h. 5 h represents an incubation time in which most of the NPs have been internalized [33]; for 24 hours it is assumed that saturation has been reached (plateau).

Both cell lines were irradiated at 2 and 10 Gy and incubation occurred after 24 and 72 h from irradiation.

For confocal microscopy acquisition, cytoskeletal actin was stained with Alexa-fluor Phalloidin, while NPs were identifiable for PLGA-bound rhodamine B. Fig. 3.7 shows a summary panel of all the experimental conditions used.

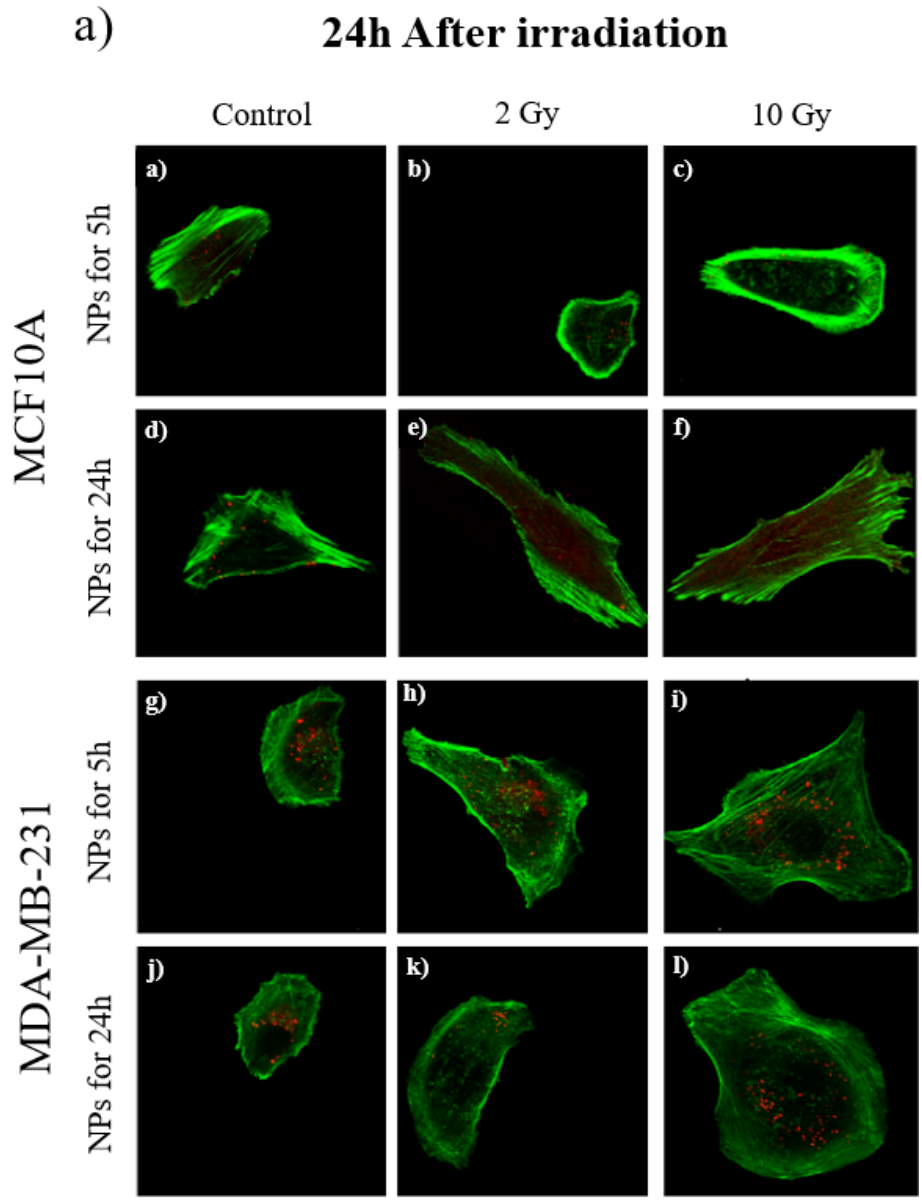
a)
24h After irradiation
Control
2 Gy
10 Gy
MCF10A
MDA-MB-231
NPs for 5h
NPs for 24h
NPs for 5h
NPs for 24h
a)
b)
c)
d)
e)
f)
g)
h)
i)
j)
k)
l)

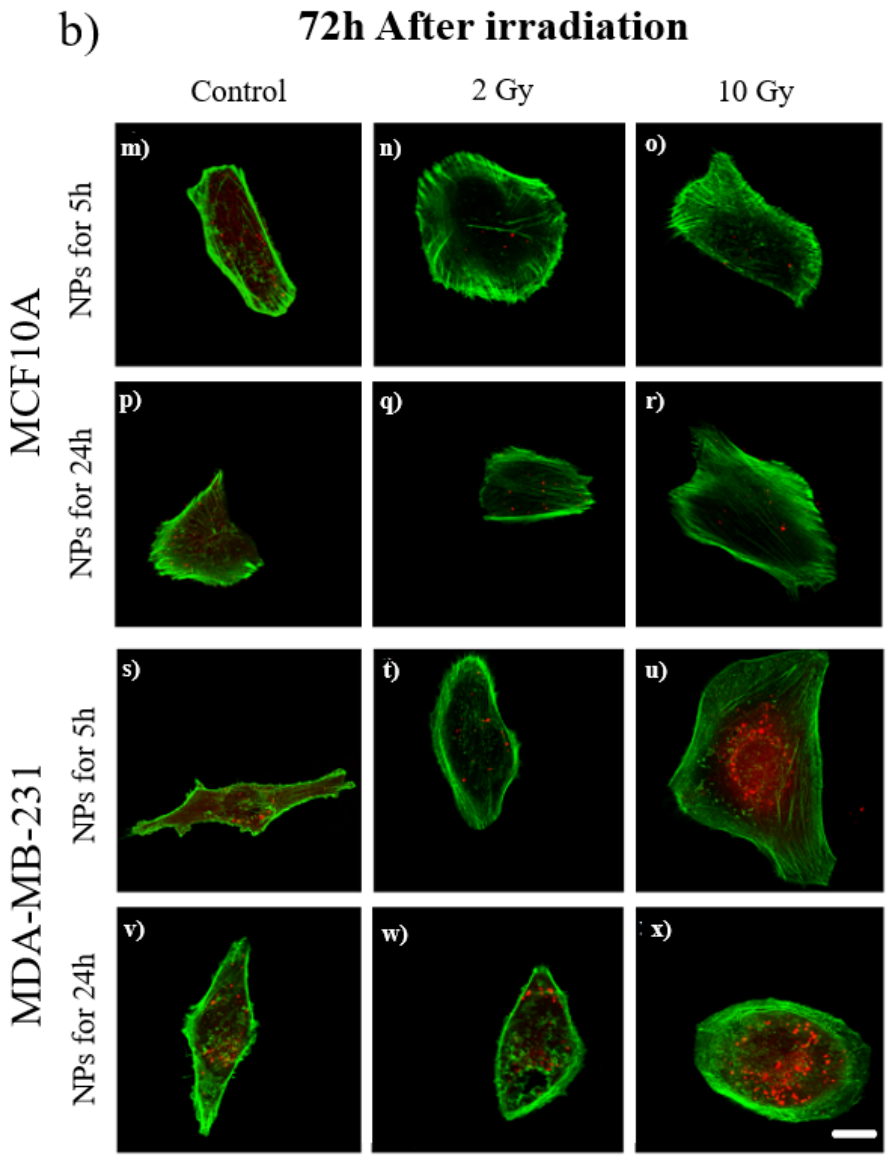

Figure 3.7 Panel of representative images for internalization studies of two cell lines in all experimental conditions: a) 24h and b)72h after irradiation. Cells were stained for actin (green), and NPs are visible in red. Scale bar: 20 µm.

Image acquisitions were processed and analysed using the ImageJ Sofware. The results are reported in Fig. 3.8 and median values measured are reported in Tab. 3.2. Statistical analyses are reported in Annex VI.

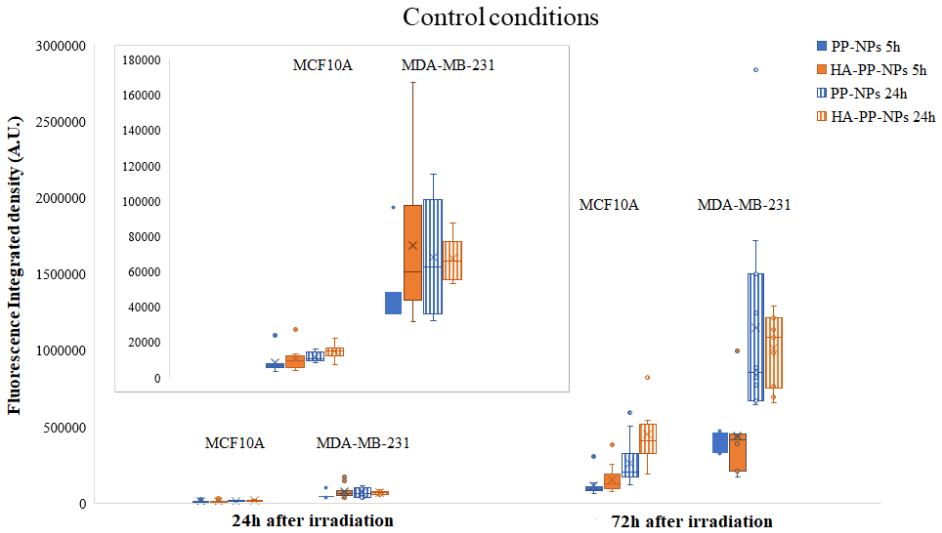

Figure 3.8 Box plots (mean value, the median, the interquartile, and the outliers) of internalization values of non-irradiated cells - control condition. The inset reveals the differences between the internalization capability of the two cell lines 24 h after irradiation.

Table 3.2 median values of internalization in control conditions

Time after irradiation	**NPs Incubation time**	**Median (Q2)** MCF10A (A.U.)	**Median (Q2)** MDA-MB-231 (A.U.)
24 h	PP-NPs 5h	6686.418	40453.281
	HA-PP-NPs 5h	9395.740	59761.133
	PP-NPs 24h	10594.644	62662.055
	HA-PP-NPs 24h	15109.519	66071.347
72h	PP-NPs 5h	88686.166	379928.968
	HA-PP-NPs 5h	125728.557	409817.739
	PP-NPs 24h	202378.797	854713.470
	HA-PP-NPs 24h	403527.788	1086199.138

The "*after irradiation*" labeling of the abscissa should not be misleading, as the control conditions were not irradiated but were coeval with the irradiated samples. By defining a T_0 on the day of irradiation, the two times for all the samples were then defined. In this way, control realistically represents the potential to internalize each cell line at a given time interval.

The most immediate evaluation is related to time: the highest median value of integrated density at 24h after irradiation is 16 times lower than the highest value of the condition at 72h after irradiation. Incubation time also affected the quantity of internalized NPs. Therefore, regardless of cell lines and formulation, it can be assumed that a parameter promoting internalization is time.

Considering the cell lines, MCF10A has a time dependent internalization capability with a higher affinity for HA-PP-NPs. However, the integrated density values are far lower than those of the tumor counterpart. MDA-MB-231 also internalizes more HA-PP-NPs than PP-NPs, however at 24h after irradiation this trend is more marked compared to the 72h after irradiation condition which, in addition to confirming the affinity for HA, reveals an incubation time dependent trend.

Finally, a minor internalization difference between the two formulations (PP-NPs vs HA-PP-NPs) could be caused by the protein corona effect discussed previously. However, the encouraging results concern the significant difference in internalization between the two cell lines, confirming that tumor cells have alterations in the internalization mechanisms favoring drug delivery.

From the first results, it seems that the starting rationale, that is to exploit the overexpression of CD-44 in tumor cells and its affinity to bind HA, could be threatened precisely by the effects of the protein corona.

So, the purpose of this experiment was to understand if ionizing radiation can affect the internalization mechanisms and therefore represents a reasonable solution to this discussed problem, premising the design of an alternative approach to drug delivery.

Fig 3.9 shows the data relating to internalisation 24 h after irradiation; Tab. 3.3 median values measured. Healthy cell line does not show relevant variations compared to the control conditions, however, irradiation at a dose of 2 Gy produced a slight increase in internalization of both PP-NPs and HA-PP-NPs. At 10 Gy the values are equal/lower than those of the controls.

On the contrary, the tumor line seems to respond to physical stress induced by irradiation, in a way that favors internalization with a dose and incubation time dependent trend.

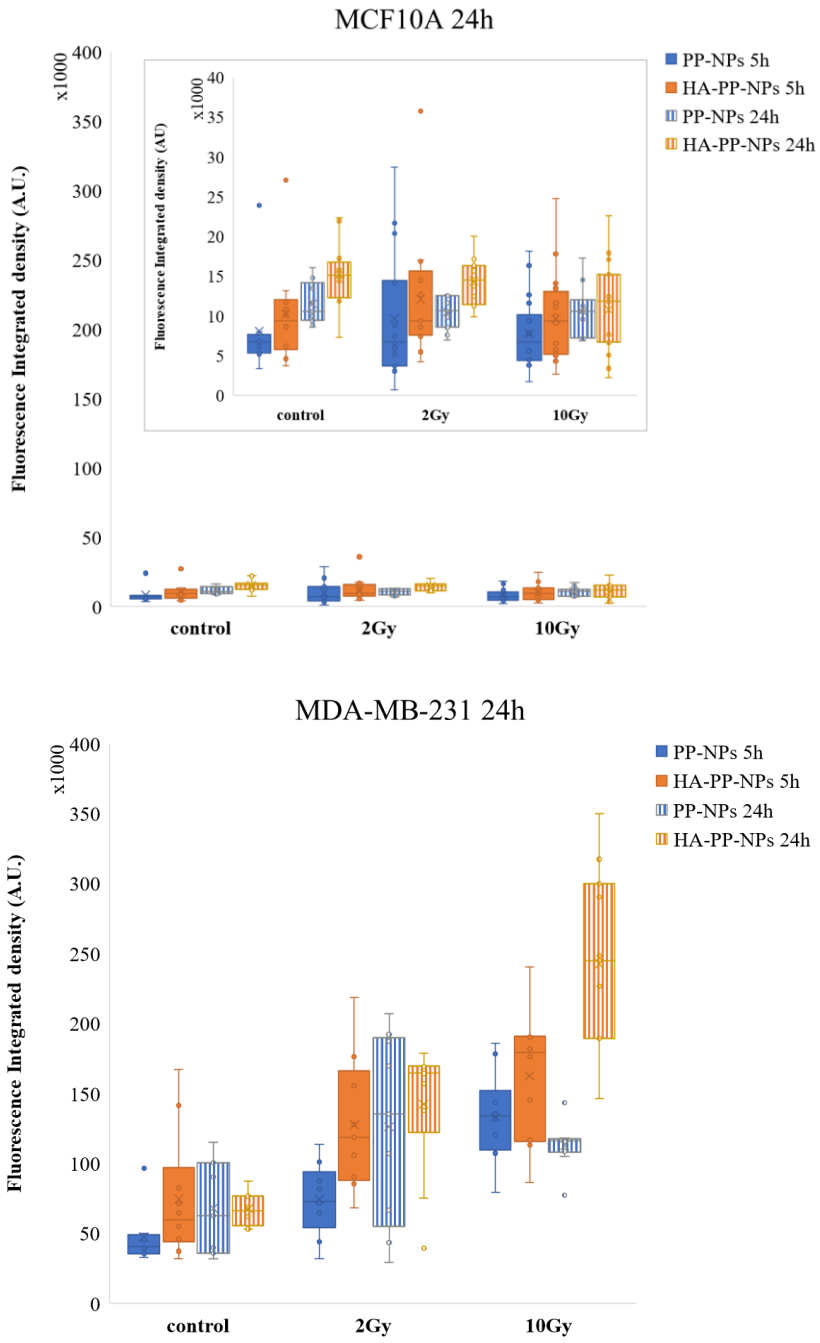

Figure 3.9 Box plots (mean value, the median, the interquartile, and the outliers) of internalization 24h after irradiation of MCF10A (top) and MDA-MB-231 (bottom).

Table 3.3 Median values of internalization 24h after irradiation

Dose (Gy)	**NPs Incubation time**	**Median (Q2)** MCF10A (A.U.)	**Median (Q2)** MDA-MB-231 (A.U.)
control	PP-NPs 5h	6686.418	40453.28
	HA-PP-NPs 5h	9395.740	59761.13
	PP-NPs 24h	10594.644	62662.06
	HA-PP-NPs 24h	15109.519	66071.35
2 Gy	PP-NPs 5h	6686.418	72674.79
	HA-PP-NPs 5h	9395.740	118743.21
	PP-NPs 24h	10649.932	135082.68
	HA-PP-NPs 24h	14533.415	164785.58
10 Gy	PP-NPs 5h	6686.418	133524.24
	HA-PP-NPs 5h	9395.740	178952.37
	PP-NPs 24h	10594.644	116184.95
	HA-PP-NPs 24h	11822.838	246729.80

Fig 3.10 shows the data relating to internalisation 72h after irradiation; Tab. 3.4 median values measured

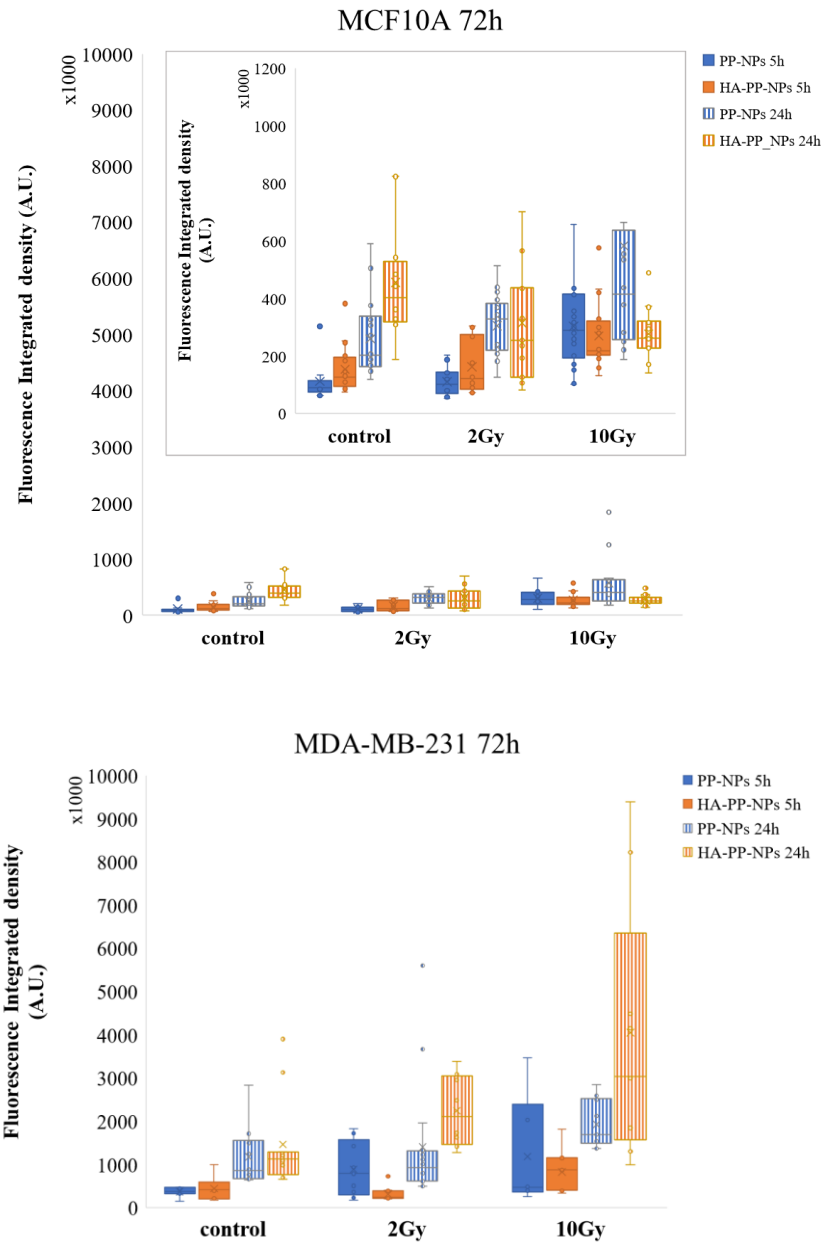

Figure 3.10 Box plots (mean value, the median, the interquartile, and the outliers) of internalization 72h after irradiation of MCF10A (top) and MDA-MB-231 (bottom).

Table 3.4 Median values of internalization 72h after irradiation

Dose (Gy)	**NPs Incubation time**	**Median (Q2)** MCF10A (A.U.)	**Median (Q2)** MDA-MB-231 (A.U.)
Control	PP-NPs 5h	88686.166	379928.968
	HA-PP-NPs 5h	125728.557	409817.739
	PP-NPs 24h	202378.797	854713.470
	HA-PP-NPs 24h	403527.788	1133780.810
2 Gy	PP-NPs 5h	101328.457	787364.910
	HA-PP-NPs 5h	120684.478	241137.678
	PP-NPs 24h	327917.014	931054.412
	HA-PP-NPs 24h	255164.199	2110740.271
10 Gy	PP-NPs 5h	289785.700	467536.683
	HA-PP-NPs 5h	216484.345	866957.671
	PP-NPs 24h	414334.795	1697882.287
	HA-PP-NPs 24h	260684.345	3036454.608

After 72 h from irradiation, the integrated density values increase by an order of magnitude in all conditions.

MCF10A at 2 Gy shows an internalization capability similar to control with an incubation time and dose dependent trend, with a no significant difference between the two formulations. Internalisation increases at a dose of 10 Gy while confirming this insensitivity to the type of coating.

MDA MB 231 shows a dose and time dependent internalization for an incubation time of 24 h with higher integrated density values for the HA-PP-NPs formulation than for PP-NPs one. This difference does not emerge for incubation times of 5 h

Considering ionizing radiation effects on variations in cell volumes (Annex VI), also confirmed by the acquired images (see Fig. 3.7), the integrated density values were normalized for cell volumes (Fig 3.11 and Tab. 3.5).

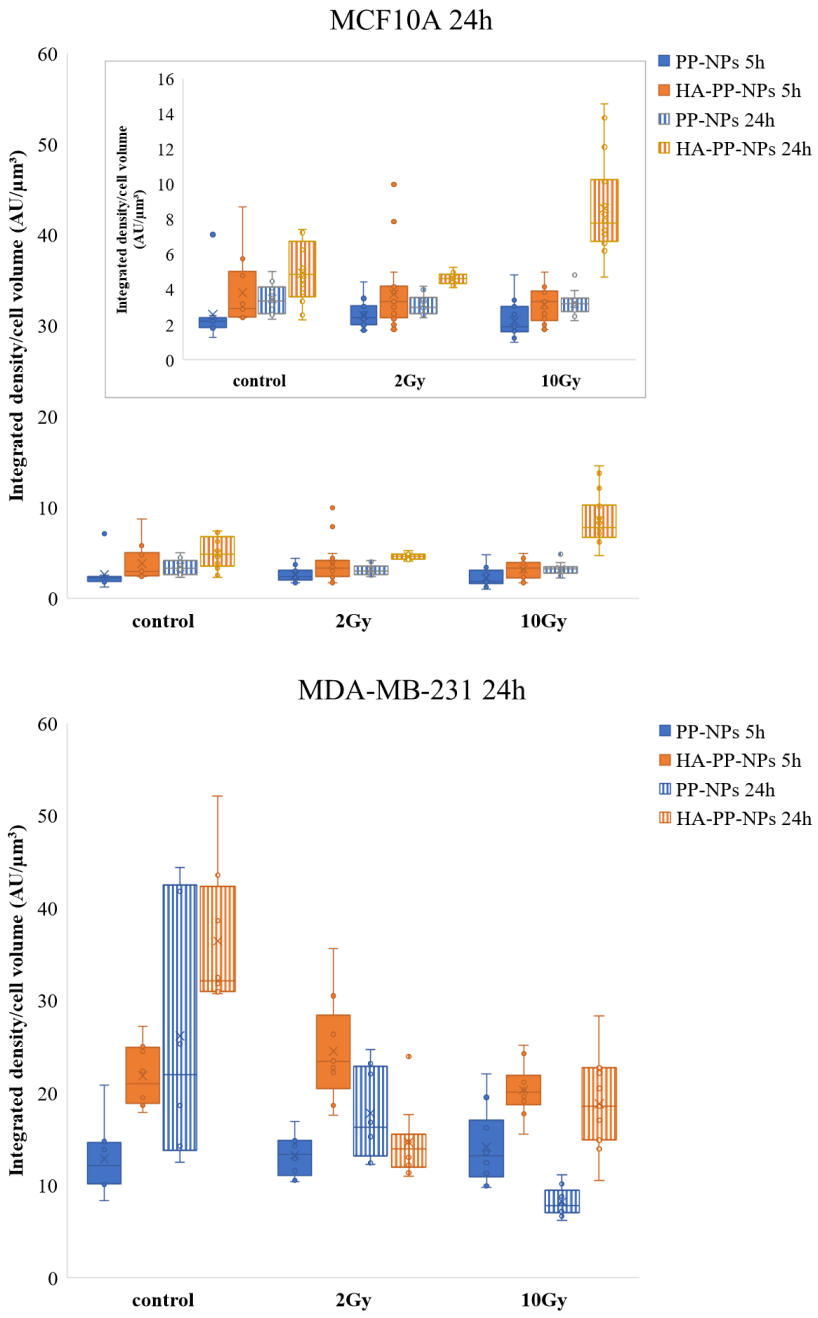

Figure 3.11 Box plots (mean value, the median, the interquartile, and the outliers) of internalization normalized to cell volume 72h after irradiation of MCF10A (top) and MDA-MB-231 (bottom).

Table 3.5 Median values of internalization normalized to cell volume 24h after irradiation

Dose (Gy)	**NPs Incubation time**	**Median (Q2)** MCF10A (A.U.)	**Median (Q2)** MDA-MB-231 (A.U.)
control	PP-NPs 5h	2.215	12.130
	HA- PP-NPs 5h	2.925	20.971
	PP-NPs 24h	3.341	21.969
	HA-PP-NPs 24h	4.863	32.119
2 Gy	PP-NPs 5h	2.395	13.309
	HA- PP-NPs 5h	3.317	23.439
	PP-NPs 24h	2.987	16.265
	HA-PP-NPs 24h	4.631	13.909
10 Gy	PP-NPs 5h	1.881	13.176
	HA- PP-NPs 5h	3.315	20.064
	PP-NPs 24h	3.211	7.790
	HA-PP-NPs 24h	7.932	18.534

The normalized values for the volume are unchanged for MCFA10A at 24h after irradiation, while for tumor cells they are reduced by up to an order of magnitude. Furthermore, there is a difference in sensitivity on the type of coating of the NPs (favoring HA-PP-NPs) and an internalization trend contrary to the previous one (Fig 3.9 b). This confirms that cancer cells increase their volume in a time and dose dependent way.

Figure 3.12 and Tab. 3.6 show data of internalization normalized to cell volume 72h after irradiation.

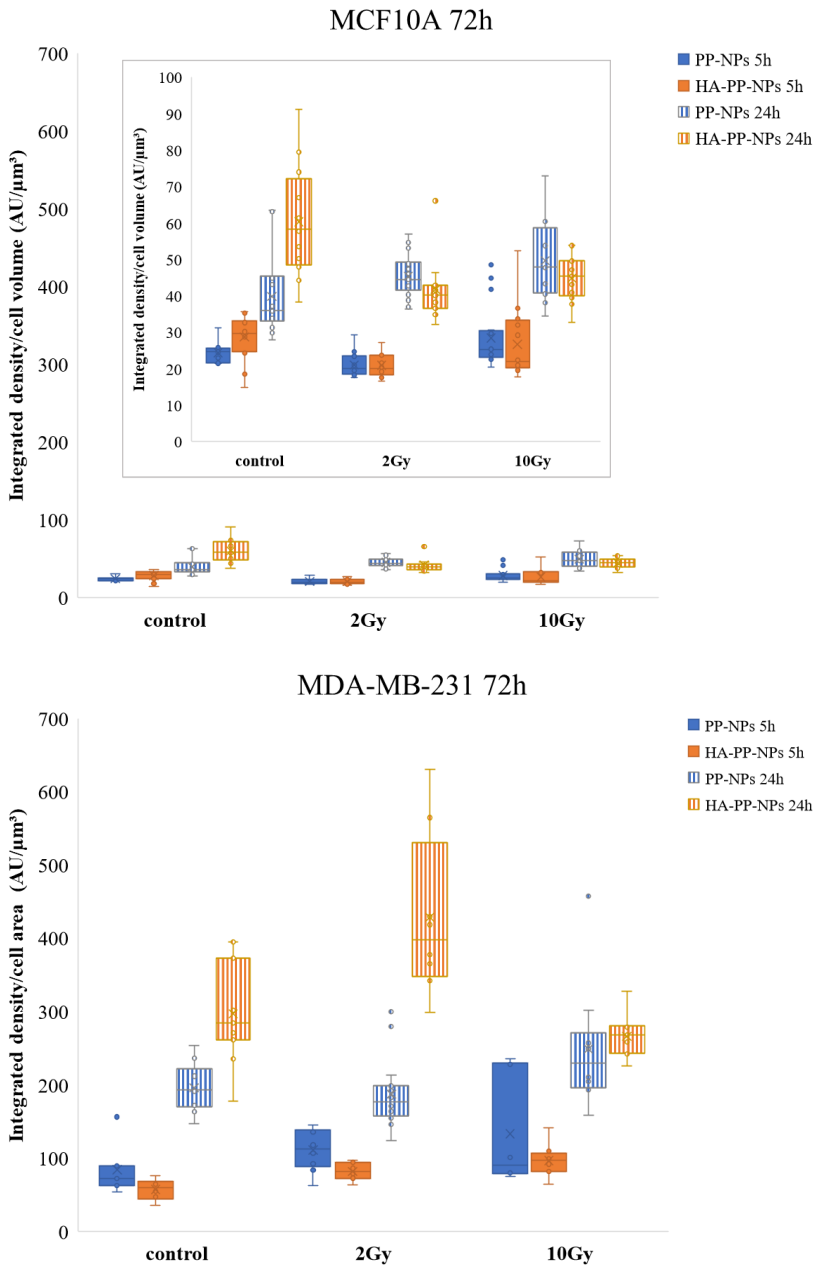

Figure 3.12 Box plots (mean value, the median, the interquartile, and the outliers) of internalization normalized to cell volume 72h after irradiation of MCF10A (top) and MDA-MB-231 (bottom).

Table 3.6 Median values of internalization normalized to cell volume 72h after irradiation

Dose (Gy)	**NPs Incubation time**	**Median (Q2)** MCF10A [A.U.]	**Median (Q2)** MDA-MB-231 [A.U.]
control	PP-NPs 5h	24.480	71.817
	HA- PP-NPs 5h	29.511	59.361
	PP-NPs 24h	35.985	192.721
	HA-PP-NPs 24h	58.164	284.401
2 Gy	PP-NPs 5h	19.870	112.428
	HA- PP-NPs 5h	20.051	82.019
	PP-NPs 24h	44.346	176.809
	HA-PP-NPs 24h	40.080	397.987
10 Gy	PP-NPs 5h	25.085	90.706
	HA- PP-NPs 5h	21.925	96.549
	PP-NPs 24h	47.924	230.008
	HA-PP-NPs 24h	45.438	267.873

Irradiated healthy cell line has a dose and time dependent internalization with no particular difference between the two formulations. Indeed, it seems that the cells irradiated at both doses internalize less than the control condition. Tumor line, on the contrary, for incubation times of 5 h shows no difference between the two formulations, after 24 h it shows a marked affinity for HA-PP-NPs formulation regardless of the dose.

From the point of view of a pharmacological approach, while considering the weight of internalization with respect to cell volume, it is important to consider the absolute value of the integrated density and therefore the internalization potential of a drug. Therefore, the effect of radiotherapy could be twofold: increasing the cell volume of cancer cells and favoring a greater supply of NPs loaded with chemotherapy drug.

References

1. Matsumura Y, et al. 1986. *Cancer Res*. **46**(12 Pt 1):6387-6392.
2. Folkman J. 1995. *Nat Med*. **1**(1):27-31. doi:10.1038/nm0195-27.
3. Yetisgin AA, et al. 2020. *Molecules.* **25**(9):2193. doi:10.3390/molecules25092193.
4. Sabourian P, et al. 2020. *Int J Mol Sci.* **21**(21):8019. doi:10.3390/ijms21218019.
5. Ponta H, et al. 2003. *Nat Rev Mol Cell Biol*. **4**(1):33-45. doi:10.1038/nrm1004.
6. Naor D, et al. 1997. *Adv Cancer Res*. **71**:241-319. doi:10.1016/s0065-230x(08)60101-3.
7. Yan Y, et al. 2015. *Stem Cells Transl Med*. **4**(9):1033-1043. doi:10.5966/sctm.2015-0048.
8. Naor D, et al. 2008. *Semin Cancer Biol*. **18**(4):260-267. doi:10.1016/j.semcancer.2008.03.015.
9. Kogan G, et al. 2007. *Biotechnol Lett*. **29**(1):17-25. doi:10.1007/s10529-006-9219-z.
10. Abatangelo G, et al. 2020 *Cells*. **9**(7):1743. doi:10.3390/cells9071743.
11. Fraser JR, et al. 1997. *J Intern Med.* **242**(1):27-33. doi:10.1046/j.1365-2796.1997.00170.x.
12. Callaghan R, et al. 2014. *Drug Metab Dispos*. **42**(4):623-631. doi:10.1124/dmd.113.056176
13. Misra S, et al. 2003. *J Biol Chem*. **278**(28):25285-25288. doi:10.1074 / jbc.C300173200
14. Lesley J, et al. 2000. *J Biol Chem.* **275**(35):26967-26975. doi:10.1074 / jbc.M002527200
15. Fallacara A, et al. 2018. *Polymers (Basel).* **10**(7):701. doi:10.3390/polym10070701.
16. Hou X, et al. 2022. *Carbohydr Polym*. **292**:119662. doi:10.1016/j.carbpol.2022.119662.
17. Weissig V, et al. 2014. *Int J Nanomedicine*. **9**:4357-4373. doi:10.2147/IJN.S46900.
18. Yang B, et al. 1994. *EMBO J.* **13**(2):286-296. doi:10.1002/j.1460-2075.1994.tb06261.x.
19. Rios de la Rosa JM, et al. 2018. *Adv. Biosys*. **2**:1800049. doi:10.1002/adbi.201800049.
20. Laurent TC, et al. 1992. *FASEB J*. **6**(7):2397-2404.
21. Venning FA, et al. 2015. *Front Oncol*. **5**:224. doi:10.3389/ fonc.2015.00224.
22. Weigel PH, et al. 2002. *Biochim Biophys Acta*. **1572**(2-3):341-363. doi:10.1016 / s0304-4165 (02) 00318-5.
23. Huang G, et al. 2019. *Int. J. Biol. Macromol*. **125**:478–484. doi:10.1016/j.ijbiomac.2018.12.074.

24. Kim JH, et al. 2018. *Polymers (Basel).* **10**(10):1133. doi:10.3390/polym10101133.
25. Misra S, et al. 2011. *FEBS J.* **278**(9):1429-1443. doi:10.1111/j.1742-4658.2011.08071.x.
26. Ko YS, et al. 2018. *Oncol Rep*. **40**(6):3752-3762. doi:10.3892/or.2018.6714.
27. Zhang Z, et al. 2019. *Nat Commun*. **10**:3561. doi:10.1038/s41467-019-11593-z
28. Kopac T. 2021. *Int J Biol Macromol.* **169**:290-301. doi:10.1016/j.ijbiomac.2020.12.108.
29. Berrecoso G, et al. 2020. *Drug Deliv Transl Res.* **10**(3):730-750. doi:10.1007/s13346-020-00745-0.
30. Xu F, et al. 2016. *ACS Nano*. **10**(1):1189-1200. doi:10.1021/acsnano.5b06501.
31. Magro M, et al. 2019. *Biomacromolecules.* **20**(3):1375-1384. doi:10.1021/acs.biomac.8b01750.
32. Mizrahy S, et al. 2014. *Nanoscale.* **6**(7):3742-3752. doi:10.1039/c3nr06102g.
33. Panzetta V, et al. *Il nuovo cimento C*, **41**(6):1-8. doi:10.1393/ncc/i2018-18204-7

Conclusion

Breast cancer is one of the most widespread diseases in the world, despite the continuous updates of scientific research on the most effective therapeutic treatments, it continues to be difficult to cure.

The rationale of this thesis project was to consider the use of HA-functionalizes nanoparticles to overcome the limitations of free therapeutics and navigate biological barriers - systemic, microenvironmental and cellular - that are heterogeneous across patient populations and diseases. HA, due to its chemical characteristics, is one of the elements suitable for the design of NPs loading different types of drugs. Furthermore, the ionizing radiations, deriving from the radiotherapy treatment, produce mechanical alterations on the structural systems of the cell such as the CSK and ECM. The aim therefore was to investigate, from a biophysical and mechanobiological point of view, how, after a traditional radiotherapy treatment, the alterations produced may be favourable to increasing the internalization of NPs. The results could be a contribution to improving and optimizing the radio- and chemo-therapy combination. So, a patient undergoing radiotherapy could receive the administration of chemotherapy with functionalized NPs, after a definite time from irradiation to increase the intake of the drug only in the tumor site.

To this end. The biophysical properties of a breast epithelial cell line and adenocarcinoma cell line, MCF10A and MDA-MB-231 respectively, were investigated. In particular, the study was based on the investigation of cells spreading and migration ability on different substrates stiffness characterized by Young's modulus of 1.3 kPa and 13 kPa, which simulates the healthy and the tumoral tissue respectively. Samples were irradiated

with two different doses, 2 and 10 Gy, which ate the conventional dosages used in external beam radiotherapy.

Results indicate that ECM mechanics can play a very active role in mediating responses of cells to radiotherapy. On one hand, the healthy cell line after 72 h manifest the ability to restore the alterations due to irradiation, highlighting the radioprotective role of the physiological ECM; on the other hand, cancerous cells, when irradiated with 10 Gy, show an increase in their adhesion ability on the stiffer substrates which mimic pathological microenvironment. This effect is also supported by a reduced motility.

After a stability and aging study of a formulation of HA-coated NPs, which defined the time within which functionalization is stable (seven days), and the potential of SERS spectroscopy as a complementary tool in surface analysis, the internalization studies were conducted.

Both cell lines were seeded on glass plates which mimic the stiffness of the tumor microenvironment, similarly to 13 kPa PAA substrate, and were irradiated according to the aforementioned protocol. Incubation times with HA- coated and naked NPs (HA-PP-NPs and PP-NPs, respectively) were 5 h and 24 h. The results revealed that the ideal incubation time is 24 h. With respect to the effects of irradiation, after 24 h, the internalization of the tumor cell line was about an order of magnitude greater than that of the healthy cell line, and after 72 h this difference was maintained, increasing by another order of magnitude.

Therefore, it is possible to state that the ideal condition for optimizing the protocol that combines radio- and chemo-therapy, by facilitating the NPs internalization, is the exposure to the higher dose (10 Gy) of X-ray,

followed by the administration of the drug by means of well-designed, after 72 h from irradiation for an incubation time of 24 h.

These evidences set the conditions for implementing the investigation also on 3D models which recreate more accurately the tumor microenvironment conditions. Finally, it is interesting how the high dose gave more promising results; it would be interesting to perform the internalization study using higher doses, in line with the emerging trend of considering higher doses (up to 50 Gy) for shorter times, also known as FLASH therapy.

Appendix A

The linear-quadratic model

Many schemes of fractionation are well described using the so-called Linear-Quadratic (LQ) model, which represents the radiobiological effect of tissue in response to a dose insult, in the form of cells surviving fraction (SF) [1]:

$$SF = e^{-\alpha D - \beta D^2} \tag{16}$$

This model has been proven to predict biological outcomes of a radiotherapy scheme by measuring α and β parameters. In fact α represents the direct cell killing (lethal events), while β represents the accumulation of harmful but non-lethal events, and they both depends on the specific tissue, so they are referred to as radiosensitivity parameters [2]. Usually, when comparing different radiotherapy plans, the key parameter is the α/β ratio because it measures the tissue sensitivity to the fractionation scheme:

A low α/β ratio indicates that the linear component is less important to the SF than the quadratic component, so this specific tissue is highly dependant on the fraction size (dose per fraction) and has a large repairing capacity. This is characteristic of normal tissues which are usually late responding tissues.

A high α/β value indicates that the linear component is more important than the quadratic component, so this specific tissue is not dependent on the fraction size. This is characteristic of tumors and fast growing normal tissues, which are usually early responding tissues.

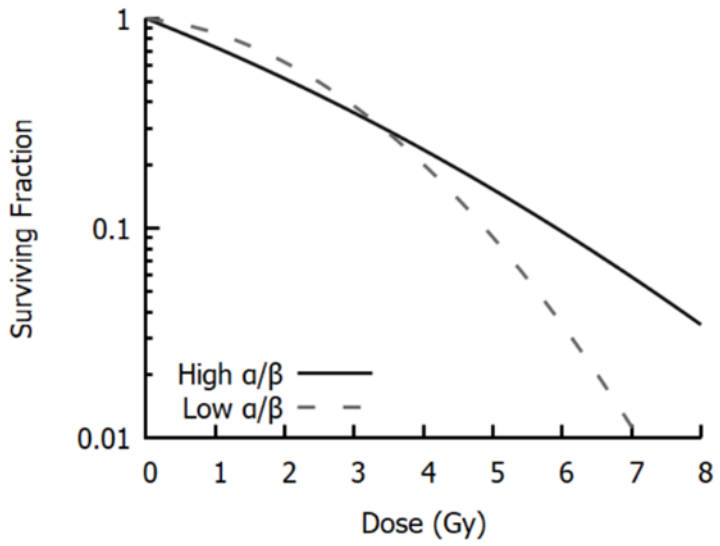

Figure A.1 Schematization of LQ curves. A high α/β ratio (order of $\sim 10\ Gy$) has nearly constant rates of cell killing with increasing dose, while a low α/β ratio (order of $\sim 3\ Gy$) shows a pronounced curvature, with greater killing per unit dose at higher doses. Adapted from [3].

As shown in A.1, the LQ curve is differently shaped between different α/β tissues. This shouldered response is particularly important when dose fractionation is used, because tissues have the time to repair the sub-lethal damage so that, during the following dose fraction, they newly present the shoulder part of the curve. In this case the LQ model can be adapted as:

$$SF = e^{-n \cdot d(\alpha+\beta d)} \tag{17}$$

where nn is the number of fractions of dose d (so that the product n·d represents the total dose during the treatment). This leads to an increase in the cell survival, affecting mostly low α/βα/β tissues [3]. The main hypothesis on which this adaptation relies on, is that the biological response of tissues is always the same for each fraction, in fact it is derived by multiplying n times a single fraction LQ curve, as supported by many studies on animals.

The LQ model has also been modified to account for the total time of the treatment, the repopulation of tissues, the apoptosis and many other factors that surely contributes to the overall tissue response to the therapy. The main results indicate that the LQ model does not always predict well the SF in the low doses range, and that αα and ββ parameters found with in vitro studies cannot always be applied on in vivo conditions [2].

The LQ model is a special case of a hit model (it comes from the target theory), based on the hypotesis that cell death is associated to the deactivation of a critical target. All cells have at least one target, which is the DNA, but some multi-target models also consider the cell membrane and some organelles as potential targets. The target 'deactivation' means that the target is damaged (hit) by ionizing radiation either after one or multiple hits, which are generally independent one from another. All of these models usually assume that cells have homogeneous behaviour, but this is not necessarely true, because of the non huniform concentration of oxygen in tissues and because of the different radiosensitivity of different cells [4]. In this context, the LQ model is a single target model and it considers the possibility for the target to be damaged by a single hit event (α) or by two minor events (β) close enough to be lethal.

TCP and NTCP models

As already said, radiotherapy aims to completely radicate the tumor from the body, but this can cause a series of collateral effects which have to be minimized [4]. To predict these effects and compare different treatment plans one has to superimpose the dose distributions with the patient anatomy and examining the Dose-Volume Histograms (DVH) [5]. From that, Tumor Control Probability (TCP) and Normal Tissue

Complication Probability (NTCP) curves can be calculated and they can be used to rank different plans according to the specific patient.

Dose-Volume Histograms are a useful tool used by medical physics to predict the dose distribution in each organ and tissue, setting the irradiation geometry, the beam energy and the dose constraints. The optimal situation is the one where TCP and NTCP are maximized and minimized, respectively. Pratically, upper and lower thresholds are derived by LQ model or other hit models, for example TCP $\geq \geq 0.5$ and NTCP $\leq 0.05 \leq$.

These curves can be derived either by using DVH or by the LQ model. The following discussion about TCP and NTCP is based only on the theoretical approach of deriving the two curves and we will not discuss specific methods of derivation using DVH.

TCP quantifies the probability that no tumor cell survives after treatment and it can be written following the Poisson distribution that describes the probability of cell killing events:

$$TCP = e^{-N \cdot p_{hit}(D)} \tag{18}$$

with the dose D. This surviving fraction can be written using the LQ model but it does not take into account the tumor regrowth.

NTCP, instead, is based on the assumption that all organs are composed of Functional Subunits (FSUs) and the damage of one or more subunits can cause a complication of normal tissue [6]. It can be written as following:

$$NTCP = 1 - \prod_{i=1}^{n} [1 - p_i(D)] \tag{19}$$

where $p_i(D)$ is the probability of damaging a single FSU and n is the total number of FSUs in the considered organ or tissue. Both TCP and

NTCP have sigmoidal relations with dose and, as shown in Fig. A.2, the optimal treatment dose is the one that maximizes the product TCP(1-NTCP)$TCP(1 - NTCP)$. This optimal dose is situated in the so called "therapeutic window", which is the dose interval with TCP>NTC

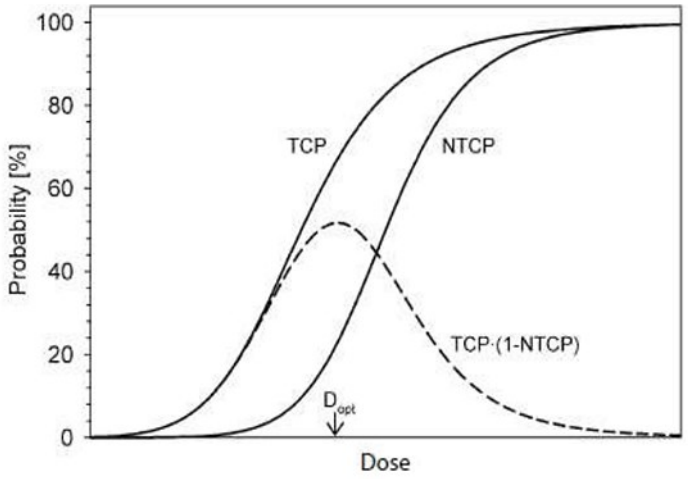

Figure A.2 Example of Tumor Control Probability and Normal Tissue Control Probability

References

1. van Leeuwen CM, et al. 2018. *Radiat Oncol*. **13**(1):96. doi:10.1186/s13014-018-1040-z.
2. Jones L, et al. 2001. *Australas Phys Eng Sci Med*. **24**(3):132-146. doi:10.1007/BF03178355.
3. McMahon SJ. 2018. *Phys Med Biol*. **64**(1):01TR01. doi:10.1088/1361-6560/aaf26a.
4. Keinj R, et al. 2011. *J Theor Biol.* **279**(1):55-62. doi:10.1016/j.jtbi.2011.03.025.
5. Warkentin B, et al. 2004. *J Appl Clin Med Phys*. **5**(1):50-63. doi:10.1120/jacmp.v5i1.1970.
6. Kazemzadeh A, et al. 2021. *Rep Pract Oncol Radiother*. **26**(1):86-92. doi:10.5603/RPOR.a2021.0015.

Appendix B

Structural components contributing to mechanosensing

The main structural components contributing to mechanosensing are: integrins, intracellular cytoskeleton (CSK), and extracellular matrix (ECM).

Integrins physically connect the CSK to the ECM through structures called focal adhesions (FAs), which represent a fundamental element in the mechanosensing process [1]. Integrins are heterodimer transmembrane receptors, having two different subunits: α and β. To date, 24 different heterodimers are known, obtained from the combination of 18 α subunits and 8 β subunits. Integrins act as bidirectional signaling receptors. Indeed, while some intercellular proteins are able to influence the mechanical properties of the environment by exerting tensile forces and breaking the ECM, a process called inside-out signaling, the binding of the ligand causes specific changes that they are able to activate cascade intercellular signaling, external-internal signaling. In addition to this, the ligand bonds can promote the grouping of integrins, which is critical for cellular diffusion. Many studies have demonstrated the connection between mechanical loading and integrin-ECM bonds. In fact, while some integrins show a slip-bond behavior characterized by a shorter bond duration as the load increases, others show a catch-bond behavior, which involves an increase in the bond duration as the load increases.

CSK is a system of interlinking protein filaments that spreads from the cell nucleus to the cell membrane. Located in the cytoplasm, it is composed of three main components, each of which plays a specific role in different biological processes: microtubules, actin filaments and intermediate filaments [2].

Microtubules are the stiffest of the cytoskeletal polymers (~25 nm in diameter) and are involved in the control of cell shape, transport and cell motility and cell division processes [3]. Microtubules can be found in two different states: stably growing or rapidly shrinking. This changing dynamic allows these structures to rapidly control the shape of the cell.

- Actin filaments, composed of two strands of actin, filamentous (F) and globular (G) proteins, (~7 nm in diameter), play an important role in endocytosis [4], exocytosis [5] and mechanical stability. Differently from the microtubules, the actin filaments do not switch between two different states, but they gradually elongate in the presence of nucleotide-bound monomers. This process produces the mechanical forces necessary to the migration of the cells. In addition to this, the actin CSK is continually assembled and disassembled in response to the signalling system. Both microtubules and actin filaments are polarized polymers and, subsequently, they act as tracks for molecular motors in a preferential direction.
- Intermediate filaments, which are the least rigid structure of CSK (~10 nm in diameter) [6], can anchor organelles in the cell and are therefore considered mechanical buffers [7,8]. Furthermore, they are involved in many other processes, such as the modulation of mitochondrial motility. Intermediate filaments are also involved in extracellular cell-matrix (ECM) crosstalk [9], cell migration and adhesion [10,11] and control of cortical and intracellular cell stiffness [12].

ECM provides mechanical support, strength and attachment sites to cells. In addition to this, the ECM provides the cell with signalling

molecules, growth factors, cytokinesis and proteolytic enzymes. There are two different types of ECM: basement membrane and connective tissues. The former is a 2D substrate on which polarized cells, such as epithelial and endothelial cells, adhere. Its main components are laminin, collagen IV, nidogen and heparan sulphate proteoglycans. The connective tissue, instead, provides the cell with a 3D support composed of fibrillar collagens, mostly type I and II, proteoglycans and glycosaminoglycans [13]. Figure B.1 shows the mechanisms involved in mechanobiology.

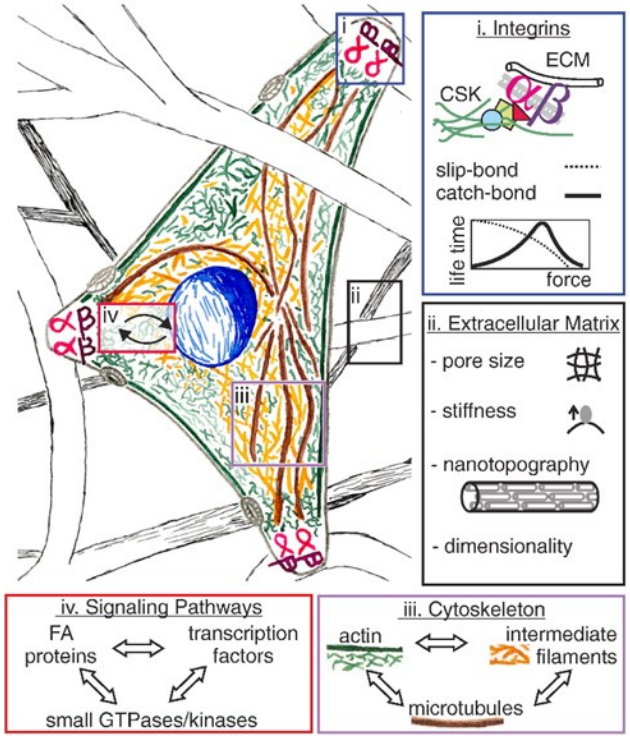

Figure B.1 Schematic of a cell in the ECM. The main elements involved in mechanosensing are shown in the boxes: (i) integrins (α and β) are grouped in FA together with other FA proteins; (ii) ECM provides signals of dimension, stiffness, nanotopography and dimensionality; (iii) CSK is composed of actin (green), intermediate filaments (yellow) and microtubules (brown); (iv) Summary of the main signaling pathways. Adapted from [14].

References

1. Baker EL, et al. *J Biomech*. **43**(1):38-44. doi:10.1016/j.jbiomech.2009.09.007.
2. Hohmann T, et al. 2019. *Cells.* **8**(4):362. doi:10.3390/cells8040362.
3. Ohi R, et al. 2016. F1000Res. **5**:F1000 Faculty Rev-314. doi: 10.12688/f1000research.7439.1.
4. Kessels MM, et al. 2021. *Curr Opin Cell Biol*. **68**:10-19. doi:10.1016/j.ceb.2020.08.008.
5. Drury JL, et al. 2001. *Biophys J.* **81**(6):3166-3177. doi:10.1016/S0006-3495(01)75953-X.
6. Theret DP, et al. 1988. *J Biomech Eng*. **110**(3):190-199. doi: 10.1115/1.3108430.
7. Schmid-Schönbein GW, et al. 1981. *Biophys J.* **36**(1):243-256. doi:10.1016/S0006-3495(81)84726-1.
8. Bausch AR, et al. 1999. *Biophys J.* **76**(1Pt1):573-579. doi:10.1016/S0006-3495(99)77225-5.
9. Levine AJ, et al. 2009. *J Phys Chem B*. **113**(12):3820-3830. doi:10.1021/jp808192w.
10. Satcher RL Jr, et al. 1996. *Biophys J.* **71**(1):109-118. doi:10.1016/S0006-3495(96)79206-8.
11. Thorne BC, et al. 2011. *Front Physiol.* **2**:20. doi:10.3389/fphys.2011.00020.
12. Wu JZ, et al. 1999. *J Biomech*. **32**(6):563-572. doi:10.1016/s0021-9290(99)00034-2.
13. Yue B. 2014. *J Glaucoma*. **23**(8suppl.1):S20-3. doi:10.1097/IJG.0000000000000108.
14. Jansen KA, et al. 2015. *Biochim Biophys Acta*1853(11 Pt B):3043-52. doi:10.1016/j.bbamcr.2015.05.007.

Appendix C

Treatment plan for cell irradiation

For a successful radiotherapy treatment plan, it is necessary to delineate the tumor volume and the volume of all the adjacent organs that should not be irradiated. For this purpose, using all the available diagnostic tests, such as CT scan, MRI or PET, it is possible to delineate the following zones:

- GTV (Gross Tumor Volume), which is the primary site of the tumor, that can be imaged or palped by doctors.
- CTV (Clinical Target Volume), which is a bigger volume containing GTV. CTV accounts for an eventual spread of the tumor that cannot be imaged, thus being more difficult to delineate. If the radiotherapy is done after surgery, GTV is no longer visible, and the CTV is derived from the initial position of the GTV.
- PTV (Planning Target Volume), which is a bigger volume containing CTV that account for uncertainties in dose delivery or the patient movement during the treatment. This outer volume is needed to ensure that all the CTV is taking the prescribed dose, to fully eradicate the tumor.
- OAR (Organ at Risk), which are all the organs near the tumor that should not be irradiated. These are the main constraint in a treatment plan because the total dose for them have to respect some threshold value, specific for each organ. In some cases, also OARs have an outer volume like PTV to fully ensure their safety (PRV – Planning organ at Risk Volume).

The different volumes of interest in planning the radiotherapy treatment can be summarized as shown in the figure C.1

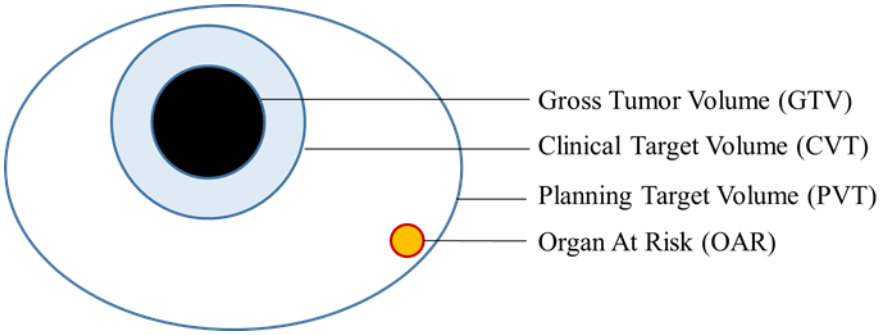

Figure C.1 Simple diagram of different volumes of interest in radiotherapy treatment planning.

Fig. C.2 and C.4 show an example of irradiation plan for 2 and 10 Gy dose respectively: the transverse section of the cell plate, above and under which are positioned the plexiglass plate, is shown. The graph beside shows the isodose curve relating to the irradiation plane. Fig. C.3 and C.5 are offprints of treatment plan report for 2 and 10 Gy, respectively.

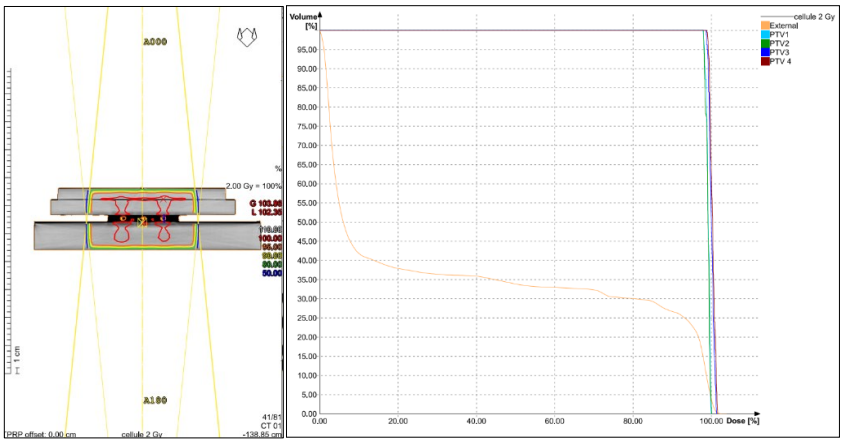

Figure C.2 Irradiation plan for a 2 Gy dose with the distribution of the dose on the samples and relative isodose curve.

Beam Information

All coordinates in the IEC 61217 system; origin at TPRP (incrocio).
The TPRP has coordinates X=0.01 cm Y=-138.85 cm Z=-0.29 cm relative to the orig

Beam	A000	A180
Beam number	1	2
Treatment unit	LINAC2	LINAC2
Radiation type	PHOTON	PHOTON
Energy	6 MV	6 MV
Fraction Group Number	1	1
Number of Fractions	1	1
MU or min / Fraction	80.68	81.34

FX (cm)	(FX)	**20.00**	(FX)	**20.00**
FY (cm)	(FY)	**20.00**	(FY)	**20.00**
X1 (cm)	(-leaf-)	-10.00	(-leaf-)	-10.00
X2 (cm)	(-leaf-)	10.00	(-leaf-)	10.00
Y1 (cm)	(Y1)	-10.00	(Y1)	-10.00
Y2 (cm)	(Y2)	10.00	(Y2)	10.00
MLC		MLCX		MLCX

Isocenter X (cm)	0.00	0.00
Isocenter Y (cm)	0.00	0.00
Isocenter Z (cm)	-0.00	-0.00
Table Top Lateral (cm)	0.00	0.00
Table Top Longitudinal (cm)	0.00	0.00
Table Top Vertical (cm)	0.00	0.00

SSD (cm)	93.81	95.11
Depth of isocenter(cm)	6.19	4.89
Gantry (degrees)	0.00	180.00
Gantry Arc Direction		
Collimator (degrees)	0.00	0.00
Couch (degrees)	0.00	0.00

Algorithm	CC (GPU)	CC (GPU)
Number of Histories		
Inhomogeneity correction	On	On

Bolus		
Bolus ID		

Dose Information

Calculation Specification Details

Density Matrix Spacing X, Y, Z (cm)	0.30; 0.30; 0.30
Dose Slice Distance Y (cm)	0.50
Dose Grid Spacing X, Z (cm)	0.30; 0.30
Dose Grid Size X, Y, Z (cm)	41.10; 33.50; 11.70
Dose Grid Position (cm)	Right = -19.64 Left = 21.46 Posterior = -5.08 Anterior = 6.62 Inferior = -17.00 Superior = 16.50
External Axial Extension (cm)	Inferior = 0.00 Superior = 0.00

Normalization and Prescription

Normalization: norm (X=-1.35, Y=1.50, Z=0.27) cm
Normalization dose: 100%
Absolute dose 2.00 Gy (2.00 Gy / Fraction) corresponds to the relative dose 100%

Fraction Information

Beam	A000	A180
Beam Number	1	2
Fraction Group Number	1	1
Number of Fractions	1	1
MU or min / Fraction	80.68	81.34
Beam Dose (Gy/Fraction)	1.00	1.00
Specification Point	norm (-1.4, 1.5, 0.3)	norm (-1.4, 1.5, 0.3)

Dose Point Information

Dose Point Label	**Coordinates X, Y, Z (cm)**	**Dose (Gy/Fraction)**	**Total Dose (Gy)**
norm **Normalization point** **Dose specification point**	-1.35; 1.50; 0.27	2.00	2.00
Iso [A000\A180]	0.00; 0.00; -0.00	2.00	2.00

Total Dose Point Contributions

Beam		A000	A180
Beam Number		1	2
MU or min / Fraction		80.68	81.34
norm (-1.4, 1.5, 0.3) Normalization point	**Dose (Gy / Fraction)**	1.00 Dose specification point	1.00 Dose specification point
	SSD (cm)	93.85	95.09
	Depth (cm)	5.90	5.20
	Rad. Depth (cm)	5.65	5.49
Iso [A000\A180] (0.0, 0.0, -0.0)	**Dose (Gy / Fraction)**	0.99	1.01
	SSD (cm)	93.77	95.07
	Depth (cm)	6.23	4.93
	Rad. Depth (cm)	5.38	5.14

Dose Volume Information

Label	**Volume (ccm)**	**Calculated Points**	**D98 (Gy)**	**D2 (Gy)**	**D50 (Gy)**	**Min (Gy)**	**Max (Gy)**	**Average (Gy)**	**Std.Dev. (Gy)**	**Bulk Density**	**Rel. Density**
External	12103.63	268969	0.01	2.02	0.12	0.00	2.08	0.72	0.85		
PTV1	3.63	80	1.96	2.00	1.98	1.96	2.00	1.98	0.01		
PTV2	4.41	97	1.96	2.00	1.98	1.96	2.00	1.98	0.01		
PTV3	3.61	80	1.98	2.02	2.00	1.97	2.03	2.00	0.01		
PTV 4	3.89	86	1.98	2.03	2.01	1.98	2.03	2.01	0.01		

Fig. C.3 Report offprint of treatent plan for a dose of 2 Gy

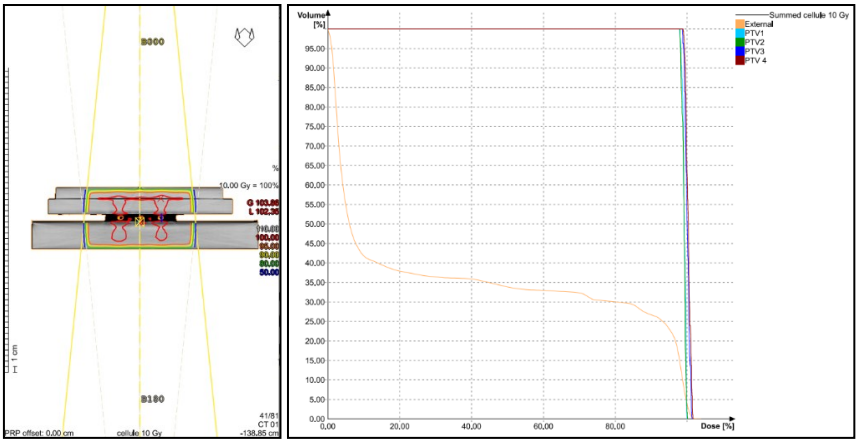

Figure C.4 Irradiation plan for a 10 Gy dose with the distribution of the dose on the samples and relative isodose curve

Beam Information

All coordinates in the IEC 61217 system; origin at TPRP (incrocio).
The TPRP has coordinates X=0.01 cm Y=-138.85 cm Z=-0.29 cm relative to the origin of the original DICOM patient coordinate system.

Beam	B000	B180
Beam number	1	2
Treatment unit	LINAC2	LINAC2
Radiation type	PHOTON	PHOTON
Energy	6 MV	6 MV
Fraction Group Number	1	1
Number of Fractions	1	1
MU or min / Fraction	403.39	406.68

FX (cm)	(FX)	**20.00**	(FX)	**20.00**
FY (cm)	(FY)	**20.00**	(FY)	**20.00**
X1 (cm)	(-leaf-)	-10.00	(-leaf-)	-10.00
X2 (cm)	(-leaf-)	10.00	(-leaf-)	10.00
Y1 (cm)	(Y1)	-10.00	(Y1)	-10.00
Y2 (cm)	(Y2)	10.00	(Y2)	10.00
MLC		MLCX		MLCX

Isocenter X (cm)	0.00	0.00
Isocenter Y (cm)	0.00	0.00
Isocenter Z (cm)	-0.00	-0.00
Table Top Lateral (cm)	0.00	0.00
Table Top Longitudinal (cm)	0.00	0.00
Table Top Vertical (cm)	0.00	0.00

SSD (cm)	93.81	95.11
Depth of isocenter(cm)	6.19	4.89
Gantry (degrees)	0.00	180.00
Gantry Arc Direction		
Collimator (degrees)	0.00	0.00
Couch (degrees)	0.00	0.00

Algorithm	CC (GPU)	CC (GPU)
Number of Histories		
Inhomogeneity correction	On	On

Bolus		
Bolus ID		

Dose Information

Calculation Specification Details

Density Matrix Spacing X, Y, Z (cm)	0.30; 0.30; 0.30
Dose Slice Distance Y (cm)	0.50
Dose Grid Spacing X, Z (cm)	0.30; 0.30
Dose Grid Size X, Y, Z (cm)	41.10; 33.50; 11.70
Dose Grid Position (cm)	Right = -19.64 Left = 21.46 Posterior = -5.08 Anterior = 6.62 Inferior = -17.00 Superior = 16.50
External Axial Extension (cm)	Inferior = 0.00 Superior = 0.00

Normalization and Prescription

Normalization: norm (X=-1.35, Y=1.50, Z=0.27) cm
Normalization dose: 100%
Absolute dose 10.00 Gy (10.00 Gy / Fraction) corresponds to the relative dose 100%

Fraction Information

Beam	B000	B180
Beam Number	1	2
Fraction Group Number	1	1
Number of Fractions	1	1
MU or min / Fraction	403.39	406.68
Beam Dose (Gy/Fraction)	5.00	5.00
Specification Point	norm (-1.4, 1.5, 0.3)	norm (-1.4, 1.5, 0.3)

Dose Point Information

Dose Point Label	**Coordinates X, Y, Z (cm)**			**Dose (Gy/Fraction)**	**Total Dose (Gy)**
norm Normalization point Dose specification point	-1.35;	1.50;	0.27	10.00	10.00
Iso [B000\B180]	0.00;	0.00;	-0.00	9.99	9.99

Total Dose Point Contributions

Beam		B000	B180
Beam Number		1	2
MU or min / Fraction		403.39	406.68
norm (-1.4, 1.5, 0.3) Normalization point	**Dose (Gy / Fraction)**	5.00 Dose specification point	5.00 Dose specification point
	SSD (cm)	93.85	95.09
	Depth (cm)	5.90	5.20
	Rad. Depth (cm)	5.65	5.49
Iso [B000\B180] (0.0, 0.0, -0.0)	**Dose (Gy / Fraction)**	4.93	5.06
	SSD (cm)	93.77	95.07
	Depth (cm)	6.23	4.93
	Rad. Depth (cm)	5.38	5.14

Dose Volume Information

Label	**Volume (ccm)**	**Calculated Points**	**D98 (Gy)**	**D2 (Gy)**	**D50 (Gy)**	**Min (Gy)**	**Max (Gy)**	**Average (Gy)**	**Std.Dev. (Gy)**	**Bulk Density**	**Rel. Density**
External	12103.63	268969	0.07	10.10	0.60	0.00	10.39	3.58	4.24		
PTV1	3.63	80	9.80	9.99	9.92	9.78	9.99	9.92	0.05		
PTV2	4.41	97	9.80	10.00	9.91	9.80	10.01	9.91	0.05		
PTV3	3.61	80	9.88	10.12	10.00	9.86	10.14	10.01	0.07		
PTV 4	3.89	86	9.91	10.15	10.03	9.89	10.16	10.03	0.07		

Fig. C.5 Report offprint of treatment plan for a dose of 10 Gy

Appendix D

Kruskal-Wallis test

The Kruskal-Wallis test is a non-parametric method used to test two or more independent samples, of equal or different size, and establish whether samples come from the same distribution. Differently from the ANOVA test, the Kruskal-Wallis test does not assume samples fallow the normal distribution of the residual. Therefore, if the user can make the assumption of an identically shaped distribution for all groups of samples, except for any difference in the medians, the null hypothesis is that all the medians of the group are equal. Alternatively, the hypothesis is that at least one population median of one group is different from the median of at least one other group.

In order to calculate the test statistic, identified by the letter H, the user has to rank all data, that is rank data from 1 to N without taking into account the group membership. The test is given by

$$H = (N-1)\frac{\sum_{i=1}^{g} n_i(\bar{r_i} - \bar{r})^2}{\sum_{i=1}^{g}\sum_{j=1}^{n_i}\left(r_{ij} - \bar{r}\right)^2} \tag{20}$$

where:

- g is the number of all groups;
- n_i is the number of observations in the group i;
- r_{ij} is the rank of the observation j in the group i;
- N is the total number of observations between all groups;
- $\bar{r_i} = \frac{\sum_{j=1}^{n_i} r_{ij}}{n_i}$ is the average rank of all observations in the group i;
- $\bar{r} = \frac{1}{2}(N+1)$ is the average of all r_{ij}.

The decision to reject the null hypothesis is given by the comparison of H with a critical value, H_c, obtained from a table, also known as alpha

level. In fact, if the former value is bigger than the latter, then the null hypothesis is rejected.

The distribution of H is approximately a chi-squared distribution with a $g - 1$ degrees of freedom. This implies that the chance of getting a specific value of H, if the null hypothesis is true, is equivalent to the P-value corresponding to a chi-square equal to H.

Statistical analyses of spreading data

			Control	***2 Gy***				***10 Gy***			
				24h		72h		24h		72h	
			H	**S**	**H**	**S**	**H**	**S**	**H**	**S**	**H**
Control		**S**	***, NS ***, NS	**, ### ***, NS	***, NS **, ##	***, ### ***, NS	NS, NS ***, ###	**, NS NS, ##	***, NS NS, ###	NS, NS NS, ###	***, ### ***, ###
		H		***, ### **, #	***, NS ***, ###	***, ### **, NS	***, NS NS, ###	***, # ***, ###	***, NS **, ###	***, NS ***, ###	NS, ### NS, ###
2 Gy	24h	**S**			NS, ### NS, #	*, NS NS, ###	***, ### ***, NS	NS, ### NS, #	***, ### NS, ###	*, ## **, ###	***, ### ***, ###
		H				NS, ### NS, ###	***, NS ***, NS	NS, NS NS, NS	***, NS NS, NS	***, ## NS, ###	***, ### ***, ###
	72h	**S**					***, ### ***, ###	NS, ### NS, ###	***, ### NS, ###	***, NS *, ###	***, ### ***, ###
		H						***, # ***, NS	***, NS **, NS	NS, NS ***, ###	***, ### **, ###
10 Gy	24h	**S**							***, ## NS, NS	*, ## NS, ##	***, ### ***, ###
		H								***, NS *, NS	***, ### **, ###
	72h	**S**									***, ### ***, ###

*Figure I.1 Kruskal-Wallis test for spreading analyses. S stands for Soft and refers to 1.3 kPa, H stands for Hard and refers to 13 kPa. P-value of the analysed samples. Asterisks (*) are used to indicate the spreading area (black) and nuclei area (red) of MCF10A cells. Hash signs (#) refer to the MDA-MB-231 cell line. ***, ### P<0.001, **; ## P<0.01; *, # P<0.05; NS not significant.*

Annex II

Statistical analyses of migration data

			Control		*2 Gy*				*10 Gy*			
					24h		72h		24h		72h	
			S	**H**	**S**	**H**	**S**	**H**	**S**	**H**	**S**	**H**
Control		**S**		***, ###	***, ###	***, ###	***, ###	***, ###	NS, NS	***, ###	***, ###	***, ###
		H			***, ##	***, NS	***, ###	***, ###	***, ###	NS, NS	***, ###	***, ###
2 Gy	24h	**S**				***, #	***, ###	***, ###	***, ###	***, #	***, ###	***, ###
		H					***, ###	NS, ###	***, ###	***, NS	***, ###	***, ###
	72h	**S**						***, NS	***, ###	***, ###	***, ###	***, NS
		H							***, ###	***, ###	***, ###	***, NS
10 Gy	24h	**S**								**, ###	***, ###	***, ###
		H									***, ###	***, ###
	72h	**S**										***, ###

*Figure II.1 Kruskal-Wallis test for migration analyses. S stands for Soft and refers to 1.3 kPa, H stands for Hard and refers to 13 kPa. P-values obtained from the analysis of samples. Asterisks (*) are used to indicate the velocity of MCF10A cells, while hash signs (#) refers to the MDA-MB-231 cell line. ***, ### P<0.001, **; ## P<0.01; *, # P<0.05; NS not significant.*

Annex III

Statistical analyses of trajectories data

		Control	*2 Gy*		*10 Gy*	
		H	**S**	**H**	**S**	**H**
Control	**S**	***, ** NS, ### ¶¶, ¶¶	***, *** ###, ### ¶¶¶,¶¶¶	***,*** NS, ### ¶¶, ¶¶	***, * ###, ### ¶¶¶, ¶¶¶	***, ** NS, ### ¶¶¶, ¶¶¶
	H		***, * ###, ### ¶¶¶, ¶¶¶	NS, * NS, ### NS, ¶¶¶	**, NS ###, ### ¶¶¶, ¶¶¶	**, NS NS, ### ¶¶, ¶¶
2 Gy	**S**			***, NS ###, NS ¶¶, ¶¶	NS, *** NS, NS NS, NS	NS, * ###, NS ¶¶¶. ¶¶¶
	H				**, ** ###, NS ¶¶¶, ¶¶¶	**.* NS, NS ¶¶¶, ¶¶¶
10 Gy	**S**					NS, NS ###, NS ¶¶¶, ¶¶¶

*Figure III.1 Statistical test for trajectories analyses. S stands for Soft and refers to 1.3 kPa, H stands for Hard and refers to 13 kPa. Asterisks (*) refer to TER of MCF10A(left) and MDA-MB-231(right), hash signs (#) to y-displacement and pilcrow (¶) to AT. ***, ###, ¶¶¶ P < 0.001, **, ##, ¶¶ P <0.01, *, #,¶ P <0.05, NS not significant*

Statistical analyses of YAP expression

		Control	***2 Gy***		***10 Gy***	
		H	**S**	**H**	**S**	**H**
Control	**S**	***, NS, NS, NS	NS, * NS, NS	***, NS NS, NS	***, *** ###, NS	*, NS ##, NS
	H		NS, NS NS, NS	NS, NS NS, NS	NS, NS NS, NS	NS, NS ###, NS
2 Gy	**S**			***, NS NS, NS	NS, NS ###, NS	NS, NS ###, NS
	H				NS, * ###, NS	NS, NS ###, NS
10 Gy	**S**					NS, NS NS, NS
	H					

*Figure IV.1 Statistical test for $Y^{d}_{N/C}$ analyses. S stands for Soft and refers to 1.3 kPa, H stands for Hard and refers to 13 kPa. Asterisks (*) refer to 24 h (blue) and 72 h (black) of MCF10A cell. Hash signs (#) to those of MDA-MB-231 cells. ***, ### P<0.001. **, ## P<0.01. *, # P<0.05. NS not significant.*

		Control	***2 Gy***		***10 Gy***	
		H	**S**	**H**	**S**	**H**
Control	**S**	NS, NS, NS, NS	NS, NS NS, NS	NS, ***, NS, NS	NS, *** ###, ###	NS, *** NS., ##
	H		*, NS NS, NS	NS, NS NS, NS	NS, * ###, ###	***, * NS, NS
2 Gy	**S**			NS, NS NS, NS	NS, *** ###, #	NS, *** NS, NS
	H				NS, NS ###, ###	NS, NS NS, NS
10 Gy	**S**					NS, NS ###, NS
	H					

*Figure IV.2 Statistical test for $Y_{N/C}$ analyses sterisks (*) refer to 24 h (blue) and 72 h (black) of MCF10A cell. Hash signs (#) to those of MDA-MB-231 cells. ***, ### P<0.001. **, ## P<0.01. *, # P<0.05. NS not significant.*

Analyses of Y_N and Y_C

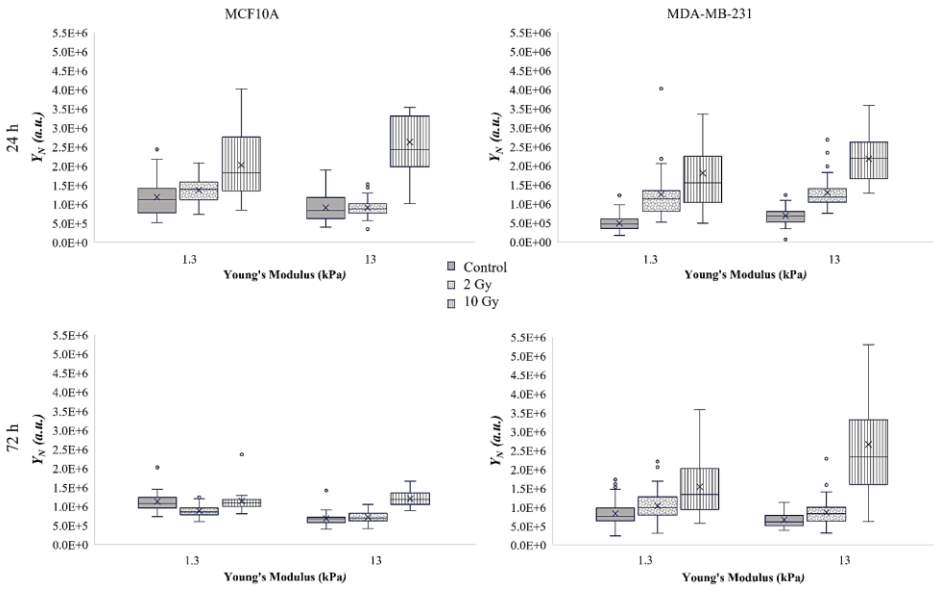

Figure V.1 Box plots of the YAP expression into the nucleus, Y_N (mean value, median, interquartile, and outliers). The values have been estimated for both cell lines 24 (top) and 72 hours (bottom) after irradiation.

		Control	***2 Gy***		***10 Gy***	
		H	**S**	**H**	**S**	**H**
Control	**S**	NS, ***, NS, NS	NS, NS ###, NS	NS, ***, ###, NS	***, NS ###, ###	***, NS ###,, ##
	H		***, NS ##, ###	NS, NS ###, NS	***, *** ###, ###	***, *** ###, ###
2 Gy	**S**			***, NS NS, NS	NS, NS NS, NS	**, *** ###, ###
	H				***, *** NS, NS	***, *** ###, ###
10 Gy	**S**					NS, NS NS, NS
	H					

*Figure V.2 Statistical test of YAP expression in nucleus(Y_N). Asterisks (*) refer to Y_N at 24 h (blue) and 72 h (black) of MCF10A cell. Hash signs (#) to those of MDA-MB-231 cells. ***, ### P<0.001. **, ## P<0.01. *, # P<0.05. NS not significant.*

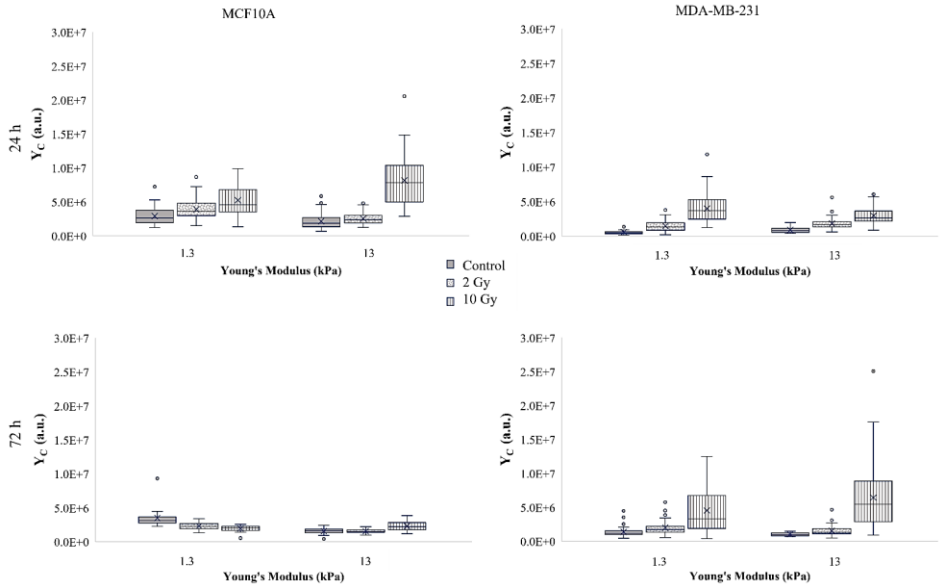

Figure V.3 Box plots of the YAP expression into the cytoplasm, Y_C, (mean value, median, interquartile, and outliers). The values have been estimated for both cell lines 24 (top) and 72 hours (bottom) after irradiation.

		Control	***2 Gy***		***10 Gy***	
		H	**S**	**H**	**S**	**H**
Control	**S**	NS, ***, NS, NS	NS, * ###, #	NS, ***, ###, NS	***, *** ###, ###	***, * ###, ###
	H		***, *** NS, ###	NS, NS ###, NS	***, NS ###, ###	***, *** ###, ###
2 Gy	**S**			***, *** NS, NS	NS, NS ###, #	*, NS ###, ###
	H				***, NS ###, ###	***, *** ###, ###
10 Gy	**S**					NS, NS NS, NS
	H					

*Figure V.4 Statistical test of YAP expression in nucleus(Y_N). Asterisks (*) refer to Y_N at 24 h (blue) and 72 h (black) of MCF10A cell. Hash signs (#) to those of MDA-MB-231 cells. ***, ### P<0.001. **, ## P<0.01. *, # P<0.05. NS not significant.*

Statistical analyses of internalization

				Control conditions							
				24 h				72h			
				5 h		24h		5h		24h	
				PP	HA	PP	HA	PP	HA	PP	HA
Control conditions	24h	5 h	PP		##, *** NS, NS	#,* ##, NS	##, *** ##, **	###, *** ###, ***	###, *** ###, ***	###, *** ###, ***	###, *** ###, ***
			HA			NS, NS NS, NS	NS, *** ##, NS	###, *** ###, ***	###, *** ###, ***	###, *** ###, ***	###, *** ###, ***
		24 h	PP				#, NS ##, NS	###, ** ###, **	###, ** ###, **	###, *** ###, ***	###, *** ###, ***
			HA					###, *** ###, ***	###, ** ###, ***	###, *** ###, ***	###, *** ###, ***
	72h	5 h	PP						##, NS #, NS	###,*** ###, ***	###, *** ###, ***
			HA							###, *** ##, **	###, *** ###, **
		24 h	PP								##, *** ##, NS
			HA								

*Figure VI.1 Statistical test of the analysed samples in control conditions. Asterisks (*) indicates the normalised integrated density (black) and the fluorescence (red) of MDA-MB-231 cells. Hash signs (#) refer to the MCF10A cell line. ***, ### P<0.001, **; ## P<0.01; *, # P<0.05; NS not significant.*

			Control				2 Gy				10 Gy			
			5 h		24h		5 h		24 h		5 h		24 h	
			PP	HA	PP	HA	PP	HA	PP	HA	PP	HA	PP	HA
Control	5 h	PP		##, *** NS, NS	#,* ##, NS	##, *** ##, **	NS, *** NS, NS	#, ** #, ***	##, *** ##, **	#, *** ##, ***	NS, *** NS, ***	#, *** NS, ***	##, *** ##, ***	###, *** NS, ***
		HA			NS, NS NS, NS	NS, *** ##, NS	#, *** NS, NS	NS, NS NS, **	NS, NS NS, NS	NS, *** ##, **	##, *** NS, **	NS, NS NS, ***	NS, *** NS, *	###, NS NS, ***
	24 h	PP			#, NS ##, NS		##, * NS, NS	NS, NS NS, *	NS, NS NS, NS	##, NS #, **	###, * ##, **	NS, NS NS, **	NS, *** NS, **	###, NS NS, ***
		HA					#, *** ##, NS	#, ** NS, **	#, *** ##, NS	NS, *** NS, ***	###, *** ###, ***	##, *** ###, ***	##, *** ##, ***	###, *** NS, ***
2 Gy	5 h	PP						#, *** NS, **	#, * NS, NS	###, NS #, **	NS, NS NS, ***	NS, *** NS, ***	#, *** NS, ***	###, ** NS, ***
		HA							NS, * NS, NS	##, *** NS, NS	###, *** NS, NS	NS, NS NS, NS	NS, *** NS, NS	###, * NS, ***
	24 h	PP								###, NS ##, NS	##, NS #, NS	NS, NS NS, NS	NS, *** NS, NS	###, NS NS, **
		HA									###, NS ###, NS	###, *** ##, NS	###, *** ##, *	###, * NS, ***
10 Gy	5 h	PP										##, ** NS, NS	##, *** NS, NS	###, * NS, ***
		HA											NS, *** NS, *	###, NS NS, **
	24 h	PP												###, *** NS, ***
		H												

*Figure VI.2 Statistical test of the analysed samples 24 hours after irradiation Asterisks (*) indicates the normalised integrated density (black) and the fluorescence (red) of MDA-MB-231 cells. Hash signs (#) refer to the MCF10A cell line. ***, ### P<0.001, **; ## P<0.01; *, # P<0.05; NS not significant*

			Control				2 Gy				10 Gy			
			5 h		24h		5 h		24 h		5 h		24 h	
			PP	HA	PP	HA	PP	HA	PP	HA	PP	HA	PP	HA
Control	5 h	PP		##, NS #, NS	###, *** ###, ***	## #, ** * ## #, ** *	NS, NS NS, NS	NS, NS NS, NS	###, *** ###, ***	###, *** ##, ***	###, NS ###, NS	###, NS ###, NS	###, *** ###, ***	###, *** ###, ***
		HA			###, *** ##, **	## #, ** * ## #, **	##, ** NS, NS	NS, ** NS, NS	###, *** ###, **	###, *** #, **	#, ** ###, NS	#, ** ###, NS	###, *** ###, ***	##, *** ###, ***
	24 h	PP				##, ** * ##, NS	###, *** ###, NS	###, *** ##, ***	NS, NS #, NS	##, *** NS, **	###, NS NS, NS	#, *** NS, NS	NS, NS ###, **	##, *** NS, **
		HA					###, *** ###, NS	###, *** ###, ***	###, *** #, NS	###, ** NS, *	###, *** ##, NS	##, *** ##, NS	#, * NS, **	###, NS ##, **
2 Gy	5 h	PP						NS, ** NS, *	###, *** ###, NS	###, *** ##, **	###, NS ###, NS	###, NS ###, NS	###, *** ###, **	###, *** ###, **
		HA							###, *** ###, ***	###, *** #, ***	###, NS ##, **	##, NS ##, ***	###, *** ###, ***	###, *** ##, ***
	24 h	PP								NS, *** NS, **	##, NS NS, NS	NS, *** NS, NS	NS, ** #, **	NS, *** NS, **
		HA									##, *** NS, NS	NS, *** NS, **	NS, ** NS, NS	NS, *** NS, NS
10 Gy	5 h	PP										NS, NS NS, NS	###, * #, NS	NS, ** NS, **
		HA											#, *** ##, ***	NS, *** NS, ***
	24 h	PP												##, NS ##, NS
		HA												

*Figure VI.3 Statistical test of the analysed samples 72 hours after irradiation Asterisks (*) indicates the normalised integrated density (black) and the fluorescence (red) of MDA-MB-231 cells. Hash signs (#) refer to the MCF10A cell line. ***, ### P<0.001, **; ## P<0.01; *, # P<0.05; NS not significant.*

Cellular volume after irradiation

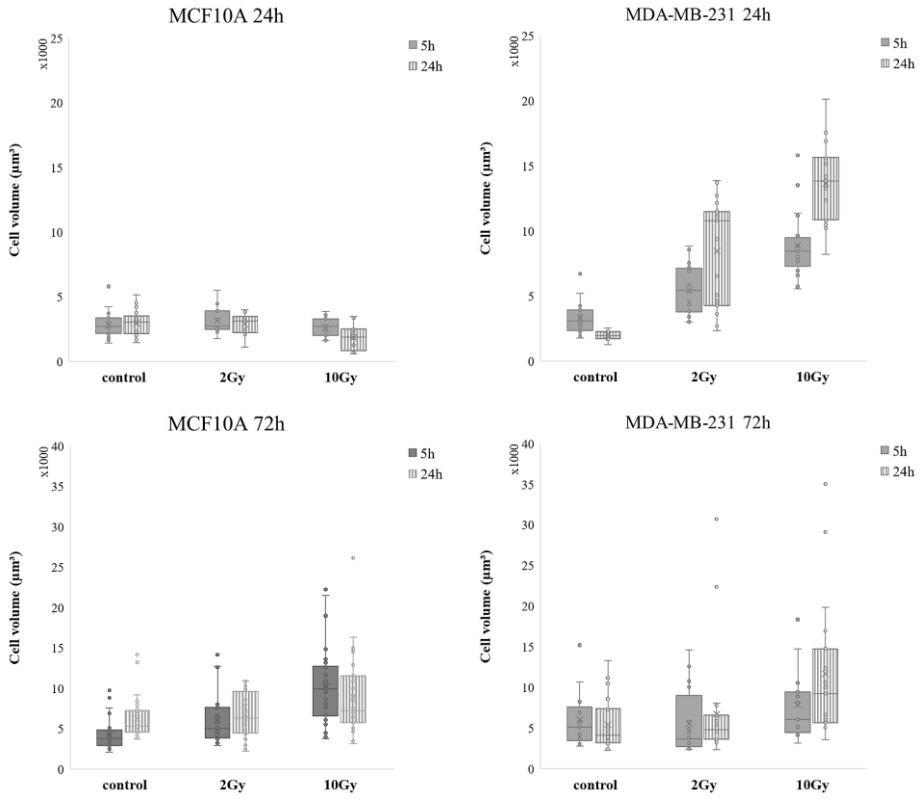

Figure VII.1 Box plots of cellular volume (mean value, median, interquartile, and outliers) of MCF10A (left) and MDA-MB-231 (right) after 24 (top) and 72 hours (bottom).